Synthesis, Morphological Optimization, and Biosensing Applications of ZnO, CuO, NiO, Co₃O₄ Nanomaterials in Plant Stress Monitoring and Environmental Diagnostics

PhD Thesis

Valdis Mizers

Supervisor: Dr. Phys Vjaceslavs Gerbreders

G. Liberts' Innovative Microscopy Centre

Daugavpils University

Abstract

The present doctoral thesis has been created by Valdis Mizers at G. Liberts' Innovative Microscopy Centre of Daugavpils University under the supervision of Dr. Phys. Vjaceslavs Gerbreders. It contains research result that were carried out in 2018-2024.

The following thesis is based on a series of 11 scientific papers published in peer-reviewed journals. The structure of the work is as following: introduction, research object and goals, theoretical framework, overview of research field, methods description, results and discussion. The thesis contains 85 pages, 32 figures, 4 tables, 1 appendix (7 pages). The list of references includes 101 titles. The thesis is written in English.

The primary focus of this thesis is creation of nanostructured coatings for electrochemical cell electrodes for the use case of electrochemical sensing. Such sensors can detect various chemical compound by analyzing electrical current dynamics caused by interaction of electrode material with solution under test.

The following study focuses on developing electrochemical cells capable of detection of herbicide (glyphosate) and plant oxidative stress indicator (hydrogen peroxide). Multiple nanostructured oxide coatings were developed, including zinc, copper, cobalt, nickel oxides, using hydrothermal and laser assisted methods. The morphology, crystalline structure, and applicability for electrochemical sensors were evaluated for each of them via scanning electron microscopy, x-ray diffraction, and enerdy dispersive x-ray spectroscopy. Those oxides were utilized to perform herbicide and oxidative stress detection in samples collected from real plants, proving *in-situ* applicability of created sensors.

The created sensors could be utilized in agriculture for rapid analysis of plant condition, governmental control over the use of herbicides, and general flora monitoring for ecological studies.

Official reviewers:

Dr.sc.ing., Prof. Andris Šutka (Riga Technical University, Latvia); *Dr.chem.*, Assoc. Prof. Anton Popov (Vilnius University, Lithuania); *Dr.phys.*, Senior Researcher Boriss Polakovs (University of Latvia, Latvia).

The defense of the doctoral thesis will take place at the open meeting of the Promotion Council for Physics and Astronomy of Daugavpils University on 16 January 2026, at Daugavpils, Parādes Street 1a, Auditorium 130, at 13:00.

The thesis and its summary can be reviewed at the **Daugavpils University Library**, Parades Street 1, Daugavpils, and on the Daugavpils University website.

Send feedback to the secretary of the Promotion Council:

Daugavpils, Parādes Street 1a, LV-5401, e-mail: eriks.sledevskis@du.lv

Chair of the Promotion Council:

Dr.phys. Irēna Mihailova

Secretary of the Promotion Council:

Dr.phys. Ēriks Sļedevskis

Scientific articles included in this work

- 1. Eriks Sledevskis, Marina Krasovska, Vjaceslavs Gerbreders, Irena Mihailova, Jans Keviss, **Valdis Mizers** and Andrejs Bulanovs "Impact of ZnO Nanostructure Morphology on Electrochemical Sensing Performance for Lead Ion Detection in Real Water Samples", Chemosensors, 2025.
 - DOI: https://doi.org/10.3390/chemosensors13020062
- Vjaceslavs Gerbreders, Marina Krasovska, Eriks Sledevskis, Irena Mihailova, Valdis Mizers, Jans Keviss and Andrejs Bulanovs "Enhancing Salt Stress Tolerance in Rye with ZnO Nanoparticles: Detecting H2O2 as a Stress Biomarker by Nanostructured NiO Electrochemical Sensor", Crystals, 2024. DOI: https://doi.org/10.3390/cryst14050423
- Vjaceslavs Gerbreders, Marina Krasovska, Eriks Sledevskis, Irena Mihailova and Valdis Mizers "Co3O4
 Nanostructured Sensor for Electrochemical Detection of H2O2 as a Stress Biomarker in Barley: Fe3O4
 Nanoparticles-Mediated Enhancement of Salt Stress Tolerance" Micromachines, 2024.
 DOI: https://doi.org/10.3390/mi15030311
- 4. Vjaceslavs Gerbreders, Marina Krasovska, Irena Mihailova, **Valdis Mizers**, Eriks Sledevskis, Andrejs Bulanovs "Selective Laser-Assisted Patterning Of ZnO: Effects Of Synthesis Parameters On Nanostructure Morphology", Latvian Journal Of Physics And Technical Sciences, 2024. DOI: https://doi.org/10.2478/lpts-2024-0042
- Irena Mihailova, Marina Krasovska, Eriks Sledevskis, Vjaceslavs Gerbreders, Valdis Mizers and Andrejs Ogurcovs "Assessment of Oxidative Stress by Detection of H2O2 in Rye Samples Using a CuO- and Co3O4-Nanostructure-Based Electrochemical Sensor", Chemosensors, 2023.
 - DOI: https://doi.org/10.3390/chemosensors11100532
- Valdis Mizers, Vjaceslavs Gerbreders, Marina Krasovska, Eriks Sledevskis, Irena Mihailova, Andrejs Ogurcovs, Andrejs Bulanovs, Andrejs Gerbreders "Non-Enzymatic Co3O4 Nanostructure-Based Electrochemical Sensor For H2O2 Detection", Latvian Journal Of Physics And Technical Sciences, 2023. DOI: https://doi.org/10.2478/lpts-2023-0037
- Irena Mihailova, Marina Krasovska, Eriks Sledevskis, Vjaceslavs Gerbreders, Valdis Mizers and Andrejs Ogurcovs "Selective Patterned Growth Of ZnO Nanoneedle Arrays", Latvian Journal Of Physics And Technical Sciences, 2023.
 - DOI: https://doi.org/10.2478/lpts-2023-0035
- Valdis Mizers, Vjaceslavs Gerbreders, Marina Krasovska, Irena Mihailova, Andrejs Bulanovs and Eriks Sledevskis "Cheap And Mass-Producible Electrochemical Sensor Of Hydrogen Peroxide", Latvian Journal Of Physics And Technical Sciences, 2023.
 - DOI: https://doi.org/10.2478/lpts-2023-0013
- Irena Mihailova, Vjaceslavs Gerbreders, Marina Krasovska, Eriks Sledevskis, Valdis Mizers, Andrejs Bulanovs and Andrejs Ogurcovs "A non-enzymatic electrochemical hydrogen peroxide sensor based on copper oxide nanostructures", Beistein Journal of Nanotechnology, 2022. DOI: https://doi.org/10.3762/bjnano.13.35
- Vjaceslavs Gerbreders, Marina Krasovska, Irena Mihailova, Eriks Sledevskis, Andrejs Ogurcovs, Edmunds Tamanis, Vitalijs Auksmuksts, Andrejs Bulanovs and Valdis Mizers "Morphology Influence On Wettability And Wetting Dynamics Of ZnO Nanostructure Arrays", Latvian Journal Of Physics And Technical Sciences, 2022.
 - DOI: https://doi.org/10.2478/lpts-2022-0004
- 11. Valdis Mizers, Vjaceslavs Gerbreders, Eriks Sledevskis, Inese Kokina, Edmunds Tamanis, Marina Krasovska, Irena Mihailova, Andrejs Ogurcovs and Andrejs Bulanovs "Electrochemical Detection Of Small Volumes Of Glyphosate With Mass-Produced Non-Modified Gold Chips", Latvian Journal Of Physics And Technical Sciences, 2020.
 - DOI: https://doi.org/10.2478/lpts-2020-0013

Table of Contents

Abstract	2
Scientific articles included in this work	2
Abbreviations	
1. Introduction	8
2. Electrochemical sensors based on metal oxide nanostructures	12
2.1. Electrochemical sensing theory	12
2.1.1. The electrochemical cell potential	13
2.1.2. Standard Electrode Potentials and Reference Systems	15
2.1.3. Non-Standard Conditions and the Nernst Equation	16
2.1.4. Current Flow in Electrochemical Cells	16
2.2. Methods of Electrochemical Analysis	18
2.2.1. Chronoamperometry	18
2.2.2. Cyclic Voltammetry	19
2.2.3. Differential Pulse Voltammetry	20
2.3. Nanostructured Metal-Oxide Sensors (ZnO, CuO, Co ₃ O ₄ , NiO)	21
2.4. Morphology–Performance Relations in Nanostructured Electrochemical Sensors	25
2.5. Scalable and Miniaturized Fabrication (PCB, Microcells, SPEs)	27
2.6. H ₂ O ₂ Detection in Plant and Complex Matrices for Oxidative Stress Monitoring	29
3. Synthesis and Morphological Characterization of Metal Oxide Nanostructures	32
3.1. Laser-assisted and Hydrothermal Synthesis of ZnO Nanoneedles with Tailored Morphology	32
3.2. Synthesis and Morphological Characterization of Copper Oxide Nanostructures	40
3.3. Synthesis and Morphological Characterization of Cobalt Oxide (Co ₃ O ₄) Nanostructures	43
3.3.1. Chloride Anion-Assisted Synthesis	43
3.3.2. Acetate Anion-Assisted Synthesis	4
3.3.3. The comparison of Chloride and Acetate anoin-assisted sytnhesized nanostructures	4
3.4. Synthesis and Morphological Characterization of Nickel Oxide Nanostructures	47
4. Cell Designs Utilized in Electrochemical Sensing Studies	49
4.1. Custom-Built Electrochemical Cell with Nanostructured Electrodes	49
4.2. Mass-Produced PCB Chip Electrochemical Cell	50

4.3. Miniaturized Droplet-Based Electrochemical Cell for Surface Morphology Studies	51
5. Glyphosate Detection Using Electrochemical Sensors	53
5.1. Experimental Procedures	54
5.2. Data Analysis and Automation Potential	55
5.3. Molecular Validation of Glyphosate Effects	55
Discussion and Implications	56
6. Electrochemical Sensors for Hydrogen Peroxide Detection Using Metal Oxides	57
6.1. Cyclic Voltammetry for Electrochemical Hydrogen Peroxide Detection	57
6.1.1. Cobalt Oxide (Co ₃ O ₄) Electrodes	57
6.1.2. Copper Oxide (CuO) Electrodes	59
6.1.3. Nickel Oxide (NiO) Electrodes	60
6.2. Sensitivity Analysis of Metal Oxide Electrodes for H ₂ O ₂ Detection	62
6.2.1. Copper Oxide (CuO) Electrode	62
6.2.2. Cobalt Oxide (Co ₃ O ₄) Electrode.	63
6.2.3. Nickel Oxide (NiO) Electrode	65
7. Plant Stress Detection Using H ₂ O ₂ Electrochemical Sensors	67
7.1. Sensor Application	67
7.2. Experimental Procedures	68
7.3. Plant stress detection using CuO and Co3O4 nanostructured electrochemical sensors	69
7.4. Correlation Between H ₂ O ₂ Accumulation and Plant Vital Functions	70
7.5. Utilization of Nanoparticles for Stress Mitigation and Sensor Application Field Expansion.	71
7.6. Chapter Summary	72
Conclusions	73
Acknowledgements	75
References	76
Appendix 1. Python program for electrochemical cell simulations	86

Abbreviations

CA Chronoamperometry
CE Counter Electrode
CNT Carbon Nanotube

CTAB Cetyltrimethylammonium Bromide

CV Cyclic Voltammetry

DPV Differential Pulse Voltammetry

EDS Energy Dispersive X-Ray Spectroscopy

EMF Electromotive Force
GCE Glassy Carbon Electrode

GOx Glucose Oxidase

HMTA Hexamethylenetetramine HRP Horseradish Peroxidase ITO Indium Tin Oxide

MOF Metal-Organic Framework
MWCNT Multiwalled Carbon Nanotube

NP Nanoparticle

PAD Paper-Based Analytical Device

PCB Printed Circuit Board PEI Polyethyleneimine

PSA Prostate-Specific Antigen PVP Polyvinylpyrrolidone

RAPD Random Amplified Polymorphic DNA

RE Reference Electrode
rGO Reduced Graphene Oxide
ROS Reactive Oxygen Species
SEM Scanning Electron Microscope
SHE Standard Hydrogen Electrode
SPE Screen-Printed Electrodes

WE Working Electrode XRD X-Ray Diffraction

1. Introduction

The development of advanced electrochemical sensing platforms based on nanostructured materials has become a key research priority due to the unique and highly tunable properties that nanomaterials offer. Among these, metal oxide nanostructures—such as ZnO, CuO, Co₃O₄, and NiO—have gained increasing attention for their excellent catalytic activity, high surface-to-volume ratio, and structural versatility. These properties make them highly suitable for the fabrication of electrochemical sensors with enhanced sensitivity, selectivity, and response time. The ability to control the morphology, composition, and surface chemistry of these nanostructures through various synthetic methods allows researchers to tailor sensor performance for specific applications, such as the detection of reactive oxygen species like hydrogen peroxide (H₂O₂).

Despite these advancements, the development and optimization of metal oxide-based electrodes remain highly challenging due to a number of unresolved issues. First, the performance of a sensor is heavily dependent on the micro- and nano-scale architecture of the electrode surface. While various synthesis techniques—such as hydrothermal growth, electrochemical deposition, and laser-assisted patterning—have been employed to fabricate nanostructured films, the influence of parameters such as precursor concentration, growth temperature, seed layer uniformity, and external stimuli (e.g., laser power) on final morphology and electrochemical performance has not been fully explored. A more systematic understanding of these factors is essential for reproducible and scalable fabrication of high-performance electrodes.

Second, while the intrinsic electrochemical activity of metal oxides makes them promising candidates for non-enzymatic sensors, their direct integration into practical sensor architectures remains limited. Many studies are still confined to conventional three-electrode setups with glassy carbon or platinum working electrodes, which are not suitable for mass production or miniaturization. The development of alternative, scalable fabrication techniques—such as the use of PCB-based chips, droplet-based microcells, and screen-printed electrodes—has only recently begun to be explored in depth. These approaches not only enable the production of compact and robust sensor systems but also allow for the simultaneous monitoring of multiple analytes in complex or low-volume samples.

Moreover, while significant progress has been made in the design of metal oxide-based electrochemical sensors, the translation of laboratory-scale devices into real-world applications remains a challenge. The need for stable, long-term, and highly sensitive sensors in harsh environments—such as those involving interfering species, varying pH, or fluctuating temperatures—has not yet been fully met. The ability to modify electrode surfaces to resist interference from common coexisting species (e.g., ascorbic acid, glucose, or citric acid) is still an area of active research, particularly for sensors intended for use in complex chemical or biological matrices.

Furthermore, the application of electrochemical sensors for the detection of oxidative stress biomarkers in plants has received relatively limited attention, despite the growing importance of monitoring plant health in response to environmental and chemical stressors. While traditional analytical methods—such as spectrophotometry and fluorescence-based assays—have been widely used to assess stress-induced changes in plants, they often require laborious sample preparation, expensive instrumentation, and are typically limited to laboratory settings. In contrast, electrochemical sensors offer a promising alternative by enabling rapid, in situ, and real-time detection of stress markers such as hydrogen peroxide (H₂O₂), a central reactive oxygen species (ROS) that is both a signaling molecule and an indicator of oxidative stress. However, the development of sensors specifically tailored for plant-based matrices—where the presence of interfering compounds and low analyte concentrations pose significant challenges—has lagged behind their use in more controlled environments such as clinical or industrial settings.

In particular, the use of metal oxide nanostructures for the detection of plant stress biomarkers remains an underexplored area. Most existing studies focus on the general electrochemical behavior of these materials in aqueous solutions or in simple buffer systems, but few address their performance in complex, real-world samples such as plant extracts, which contain a diverse array of organic and inorganic species. Moreover, there is a lack of systematic investigation into how the morphology and composition of metal oxide nanostructures influence their selectivity and sensitivity in plant-derived matrices. As a result, the design of sensors that can reliably detect stress indicators in vivo—without requiring extensive sample pretreatment—remains a critical technological gap. Addressing this gap is essential for the advancement of precision agriculture, environmental monitoring, and the development of plant stress-mitigating strategies, particularly in the context of climate change and increasing use of agrochemicals.

Goals:

- 1. To develop and optimize laser-assisted and hydrothermal synthesis methods for the controlled fabrication of high-quality ZnO nanoneedles with tailored morphologies and patterned arrangements, suitable for application in electrochemical sensing.
- 2. To develop and optimize scalable synthesis techniques for CuO, Co₃O₄, and NiO nanostructures, enabling precise control over morphology, composition, and surface properties to enhance their performance in electrochemical sensing applications.
- 3. To develop and optimize a range of electrochemical cell platforms sutable for creation of application-specific nanostructure based electrochemical sensors.
- 4. To develop and evaluate non-enzymatic electrochemical sensors based on Co3O4, CuO and NiO nanostructures for the sensitive and selective detection of hydrogen peroxide in complex plant matrices under abiotic and herbicide-induced stress conditions.
- 5. To validate sensor applicability for plants stress detection by correlating electrochemical H₂O₂ detection results with physiological and molecular stress indicators in plants.

In order to achieve the defined goals, the following tasks were identified:

- 1. Investigate the effect of precursor concentration, growth temperature, and laser parameters on the morphology and uniformity of ZnO nanoneedles using hydrothermal and laser-assisted methods.
- 2. Develop hydrothermal synthesis methods that enable the controlled formation of CuO, Co₃O₄, and NiO with repeatable morphologies and systematically characterize the synthesized nanostructures using SEM, XRD and element analysis.
- 3. Design and fabricate a variety of electrochemical sensor platforms with nanostructured electrodes suitable for in situ analysis. These platforms should be optimized for compatibility with different sample types and operational conditions.
- 4. Validate the performance of the developed electrochemical platforms across a range of applications, including in situ plant stress monitoring and glyphosate detection in agricultural samples. This includes testing for sensitivity, selectivity, reproducibility.
- 5. Fabricate and test electrochemical sensors using Co₃O₄, CuO, and NiO nanostructures in threeelectrode configurations optimized for H₂O₂ detection in aqueous and plant-derived samples.
- 6. Assess the selectivity and anti-interference capabilities of the sensors in the presence of common plant matrix interferents (e.g., ascorbic acid, glucose, citric acid) and validate their performance using calibration and real plant extract analysis.
- 7. Conduct electrochemical H₂O₂ measurements in plant samples under salt and glyphosate stress, and correlate the results with optical (chlorophyll content) and molecular (RAPD) stress indicators.
- 8. Demonstrate the utility of the sensors in monitoring the effectiveness of stress-mitigation strategies, such as the application of ZnO and Fe₃O₄ nanoparticles, by quantifying H₂O₂ levels.

During the conducted research the following methods were used:

- Hydrothermal syntesis
- Laser-assisted hydrothermal synthesis
- Scanning Electron Microscopy
- X-ray Diffractometry
- Energy Dispersive X-Ray Spectroscopy
- Cyclic Voltammetry
- Chronoamperometry
- Differential Pulse Voltammetry
- Electric Impedance Spectrometry
- Optical Spectrometry
- Random Amplified Polymorphic DNA analysis

The results of the following work are summarized in the following thesis points:

- 1. Laser-assisted and hydrothermal synthesis techniques enable the controlled fabrication of highly uniform and patterned ZnO nanoneedles, significantly enhancing their structural fidelity and suitability for application-specific design in electrochemical systems [1] [2].
- 2. Synthesis parameters were optimized to tailor the morphology of metal oxide nanostructures—including CuO nanopetals [3], Co₃O₄ nanofibers [4], and NiO nanowalls [5]—thereby improving their electrochemical activity, surface area, and stability for use in sensors targeting plant oxidative stress detection.
- 3. The developed electrochemical platforms demonstrate reliable and scalable performance in detecting analytes both in vitro and in situ. Tailored for applications including plant stress monitoring [6] [7], herbicide detection [8], and surface wetting studies [9], each platform showcases metal oxide based nanostructured sensor's adaptability to different sensing needs.
- 4. Nanostructured NiO, Co3O4, and CuO electrodes exhibit exceptional sensitivity and selectivity for hydrogen peroxide detection in plant extracts, enabling the real-time monitoring of oxidative stress under abiotic and herbicide-induced conditions [5] [7].
- 5. The sensing platform developed in this study demonstrates a strong correlation with physiological stress indicators, supporting the use of H₂O₂ as a reliable biomarker for assessing plant stress [5] [6].

Novel Aspects of the Research

- The study introduces a custom made original electrochemical platform based on metal oxide nanostructures, enabling the sensitive and selective detection of hydrogen peroxide in both controlled and real-world plant-based environments.
- A non-enzymatic electrochemical system was developed for the in situ assessment of oxidative stress in plants, offering a practical and scalable alternative to conventional analytical methods.
- The study demonstrates the utility of the developed electrochemical sensor platform in evaluating the stress-mitigating effects of Fe₃O₄ and ZnO nanoparticles, showing their potential to enhance plant resilience under abiotic and herbicide-induced stress conditions.

Practical and Applied Impact

The developed electrochemical sensors enable rapid, in situ detection of oxidative stress in plants, offering a valuable tool for precision agriculture and environmental monitoring. The study also highlights the potential of metal oxide nanoparticles as effective stress-mitigating agents, supporting the development of sustainable plant protection strategies.

2. Electrochemical sensors based on metal oxide nanostructures

Electrochemistry constitutes a specialized discipline within physical chemistry, focusing on the quantitative relationships between electrical parameters of electrochemical cells and the chemical identities of analytes. This field employs electrochemical methods wherein an electric current is passed through a sample while concurrently measuring the resulting potentials generated at the electrode-sample interface. These interactions, elaborated upon in subsequent sections, enable the characterization of chemical species through variations in current, potential, and their temporal dynamics.

The evolution of electronic instrumentation has catalyzed the development of highly sensitive electrochemical analyzers. Concurrently, advancements in computational techniques have facilitated the automation of electrochemical measurements, enhancing reproducibility and efficiency. Consequently, electrochemical analysis has emerged as a versatile analytical technique, with applications spanning the detection of herbicides, nucleic acids, atmospheric carbon monoxide, foodborne contaminants, and glucose levels in biological fluids.

A defining feature of electrochemical analysis is its reliance on current and potential measurements, offering a cost-effective alternative to more resource-intensive techniques such as mass spectrometry and chromatography. The inherent simplicity of electrochemical cells, coupled with their compact design, renders them particularly suitable for the development of portable analytical devices. The affordability and automatable nature of these systems further underscore their utility in chemical compound detection, particularly in aqueous matrices.

2.1. Electrochemical sensing theory

An electrochemical cell is a system designed to either convert chemical energy into electrical energy or induce chemical reactions via an applied electrical potential. Structurally, it comprises a sample reservoir and at least two electrodes fabricated from conductive materials, including metals, semiconductors, or carbon-based conductors [10]. Optional components, such as inert gas flow regulators, thermostats, and mixing apparatuses, may be integrated to optimize reaction conditions [11].

The operational principle of electrochemical cells is governed by interfacial reactions occurring at the electrode-electrolyte boundary [12]. These reactions determine both current generation and the initiation of selective chemical processes. The choice of electrode material is critical, as it influences the cell's sensitivity, selectivity, and overall electrochemical response [13]. Key material selection criteria include electrical conductivity, electrochemical stability, and surface properties, which dictate the cell's suitability for specific analytical applications.

Given the dependence of electrochemical performance on surface interactions, electrode modification techniques are routinely employed to enhance sensor functionality [14] [15] [16]. Surface treatments can be tailored to promote selective analyte detection via direct chemical interaction with the electrode material.

The simplest configuration of an electrochemical cell is the double-electrode system (Figure 1 A), consisting of two distinct electrodes immersed in an electrolyte solution to facilitate ion exchange [17]. These electrodes are connected via an external circuit, enabling electron transfer and subsequent electrochemical measurement.

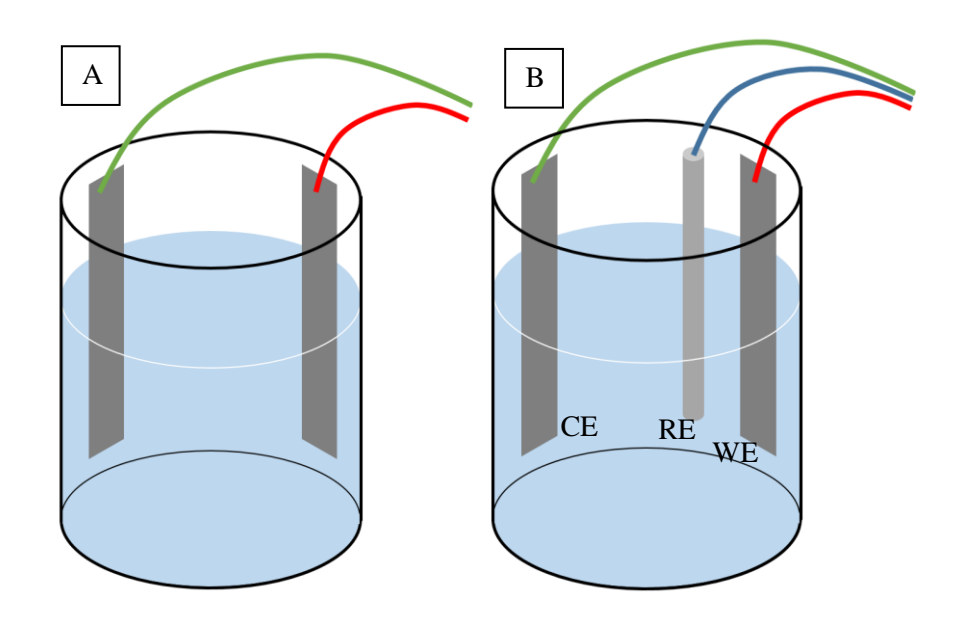


Figure 1. Schematic representation of a double-electrode (A) and triple-electrode (B) electrochemical cell. CE: counter electrode, WE: working electrode, RE: reference electrode

In certain configurations, this arrangement generates a spontaneous potential difference, dependent on the electrolyte composition and electrode materials. Such systems are classified as galvanic cells and are utilized for thermodynamic analysis. Alternatively, when an external potential is applied and current flow is measured, the system operates as an electrolytic cell, facilitating kinetic and mechanistic studies [17].

The theoretical framework of electrochemical cells is underpinned by the electrochemical series and the Nernst equation [18]. The electrochemical series ranks elements by their standard reduction potentials, predicting redox tendencies. Meanwhile, the Nernst equation quantifies electrode potentials under non-standard conditions, accounting for reactant/product concentrations and temperature effects.

2.1.1. The electrochemical cell potential

In a galvanic cell, the spontaneous generation of electrical energy from chemical reactions exemplifies the conversion of chemical potential energy into electrical work, adhering to the law of energy conservation. The electrical energy output is derived directly from the chemical energy of the participating atoms and ions engaged in the electrochemical processes [19]. The measured potential difference (voltage) between the electrodes quantifies the energy per unit charge transferred through the external circuit.

The thermodynamic relationship governing this conversion is expressed by the Gibbs free energy change associated with the cell reaction [17]:

$$-\Delta G = nFE_{\text{cell}} \tag{1}$$

Here, ΔG represents the Gibbs free energy change of the reaction, n denotes the number of electrons transferred, F is Faraday's constant, and E_{cell} corresponds to the electromotive force (EMF) or net potential difference between the electrodes. This equation establishes the principle that the electrical work performed by the cell is thermodynamically equivalent to the Gibbs free energy change driving the electrochemical process [19].

The electrochemical properties of the cell are intrinsically linked to the selection of electrode materials, which dictate the specific redox reactions occurring at the electrode-electrolyte interface [18]. The electrode potential (or reduction potential), reflecting the thermodynamic tendency of a species to gain electrons, varies significantly among different materials. Consequently, the cell potential (E_{cell}) and the associated Gibbs free energy change (ΔG) are determined by the electrode pair's composition [17]. By measuring the cell potential and calculating ΔG , it is possible to infer the chemical nature of the electrolyte through comparison with established reference values.

The electrochemical reactions within a cell are conceptualized as two distinct half-reactions, each occurring at separate electrodes. This compartmentalization underscores the principle that each electrode develops an individual potential relative to the electrolyte. The overall cell potential (E_{cell}) is mathematically defined as the difference between these electrode potentials [18]:

$$Ecell = Eeletrode B - Eeletrode A$$
 (2)

where *Eeletrode A* and *Eeletrode B* represent the potentials of electrodes A and B, respectively. This relationship is foundational to electrochemical theory, as the potential at each electrode is governed by:

- The intrinsic redox properties of the electrode material,
- The ion concentration gradients in the electrolyte, and
- The standard electrode potentials of the participating species.

The electrode exhibiting a higher reduction potential operates as the cathode, facilitating electron acceptance (reduction), while the electrode with a lower reduction potential functions as the anode, undergoing oxidation. This polarization is essential for sustaining the directional flow of current through the external circuit, enabling quantitative electrochemical analysis.

2.1.2. Standard Electrode Potentials and Reference Systems

The direct measurement of absolute electrode potentials relative to an electrolyte is experimentally impractical due to the absence of a universal reference state. This necessity led to the adoption of the standard hydrogen electrode (SHE) as an arbitrary zero-reference point. The SHE operates under defined standard conditions (1 atm pressure, 298.15 K) according to the half-reaction [18]:

$$2H^+ + 2e^- \leftrightarrow H_2 \tag{3}$$

By convention, the potential of this reaction is assigned a value of 0 V [18]. Consequently, the standard electrode potential (E^0) of any other electrode is determined as the potential difference observed when measured against the SHE under identical standard conditions. Using these standardized potentials in the cell potential equation (2) allows for the calculation of the standard cell potential for any electrochemical system. The sign of E_{cell} carries thermodynamic significance [8]:

- A positive E_{cell} indicates a spontaneous process, classifying the cell as galvanic (self-sustaining).
- A negative E_{cell} signifies a non-spontaneous process, requiring external energy input to drive the reaction (electrolytic cell).

This framework provides a quantitative basis for predicting reaction spontaneity and the direction of electron flow in electrochemical systems.

In experimental electrochemistry, a three-electrode cell configuration is commonly employed to decouple the measurement of potential from the measurement of current [18]. This configuration consists of a working electrode, a counter electrode, and a reference electrode, each fulfilling a distinct role in the system (Figure 1 B). The working electrode is the site where the electrochemical reaction of interest occurs, the counter electrode completes the electrical circuit by mediating the reverse reaction, and the reference electrode provides a stable and well-defined potential against which the working electrode's potential is measured. This separation allows for accurate control and measurement of the electrode potential without the interference of current flow through the reference electrode, which could otherwise perturb its potential and compromise the measurement [18].

Among the most widely used reference electrodes is the silver/silver chloride (Ag/AgCl) electrode, particularly in aqueous electrochemical systems [14]. The Ag/AgCl reference electrode is favored for its high reproducibility, chemical stability, and low hysteresis—that is, minimal potential drift upon polarization or prolonged use. It operates based on the redox couple [18]:

$$AgCl + e^- \leftrightarrow Ag + Cl^- \tag{4}$$

Ag/AgCl electrode potential is highly dependent on the chloride ion concentration in solution, typically 1 M KCl for standard conditions. The stability of this redox equilibrium ensures that the Ag/AgCl electrode can maintain a nearly constant potential even in the presence of small current fluctuations or changes in the working electrode environment. This stability is particularly important in electrochemical analysis, where

the accurate determination of electrode potentials is essential for both qualitative identification and quantitative evaluation of electroactive species.

2.1.3. Non-Standard Conditions and the Nernst Equation

While standard potentials describe equilibrium under ideal conditions, real-world applications often involve deviations from these parameters. The Nernst equation extends electrochemical theory to non-standard conditions by describing the relationship between applied potential and reaction quotient [17]:

$$E = E^{0} - \frac{RT}{nF} \ln \frac{[Red]}{[Ox]}$$
 (5)

Here E is the applied potential under non-standard conditions, E^{O} is the standard potential, R is the gas constant (8.314 J·mol⁻¹·K⁻¹), T is the temperature in kelvin, n is the number of electrons transferred per reaction, F is Faraday's constant (96,485 C·mol⁻¹), [Red] and [Ox] denote the molar concentrations of reduced and oxidized species, respectively.

Key implications of the Nernst equation:

- 1. Equilibrium Condition: When E=E^O, the concentrations of oxidized and reduced forms are equal ([Red]=[Ox]), resulting in zero net current.
- 2. Deviation from Equilibrium: If E differs significantly from E^o, the electrode surface undergoes complete oxidation or reduction, generating measurable current.
- 3. Reversibility Constraint: The Nernst equation applies only to reversible reactions, where the forward and reverse processes occur at comparable rates.

This thermodynamic model enables precise control over electrochemical systems, facilitating applications in sensors, batteries, and electroanalysis [17].

2.1.4. Current Flow in Electrochemical Cells

The majority of electrochemical analyses necessitate the application of an external potential to drive the electrochemical cell beyond its equilibrium state, resulting in a measurable current flow through the electrodes. This current is quantitatively described by the Butler-Volmer equation, which governs the relationship between overpotential and current density [18]:

$$\begin{cases}
j = j_0 \left(C_{Red} e^{\alpha_a \eta_{RT}^{nF}} - C_{Ox} e^{-\alpha_c \eta_{RT}^{nF}} \right) \\
\eta = E - E_{eq} \\
\alpha_a + \alpha_c = 1
\end{cases}$$
(6)

In this equation, j is the current density (A·m⁻²), T is the temperature, F is Faraday's constant, R is the ideal gas constant, n is the number of electrons transferred in the reaction, η is overpotential, E is electrode

potential, E_{eq} is equilibrium state electrode potential, C_{Red} and C_{Ox} are respectively reduced and oxidized reactant forms concentrations, α_a and α_c are the anodic and cathodic transfer coefficients. Current density jo denotes the exchange current density at equilibrium (A·m⁻²), a measure of the intrinsic reaction rate when forward and reverse processes are balanced. The overpotential (η), defined as the difference between the applied potential (E) and the equilibrium potential (E_{eq}), drives the electrochemical reaction. The equilibrium potential E_{eq} is determined using the Nernst equation (5) and depends on the concentrations of reduced and oxidized species in solution. The charge transfer coefficients (α_a and α_c), quantify the symmetry of the energy barrier for electron transfer. The values $\alpha_a = \alpha_c = 0.5$ represent ideally reversible reaction in which both oxidation and reduction occurs at equal rates, while $\alpha_a = 1$ or $\alpha_c = 1$ would represent the case of irreversible reaction.

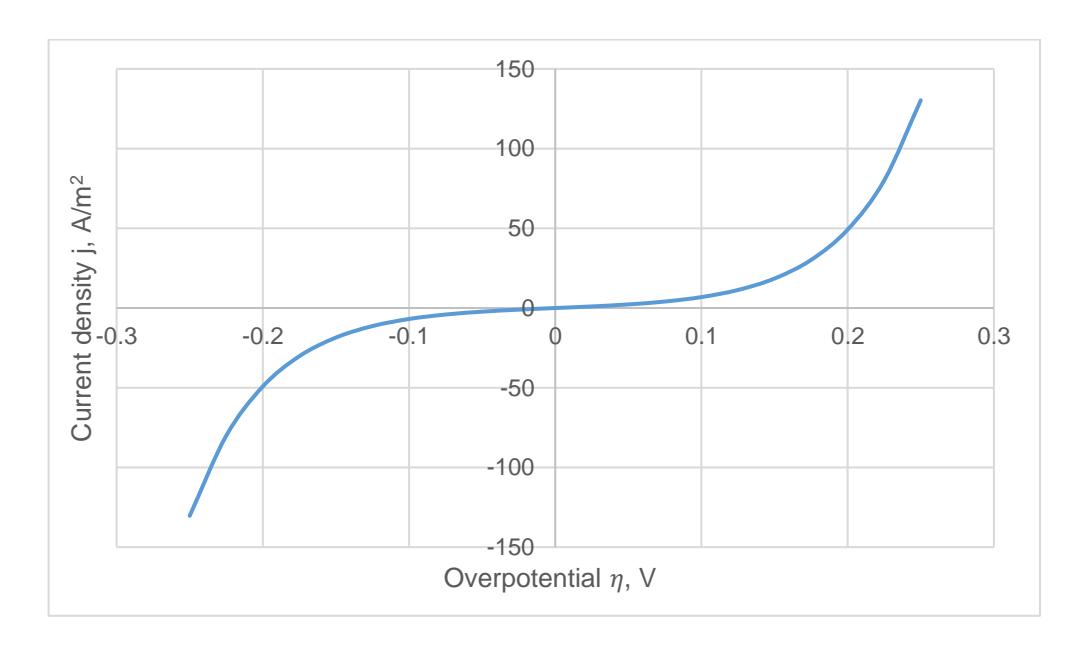


Figure 2. Current density j as function of overpotential η as defined by Butler-Volmer equation (6). This graph assumes that $j_0 = 1$ A/m², $\alpha_a = \alpha_c = 0.5$, n = 1, T = 298 K.

Under equilibrium conditions ($\eta = 0$), the Butler-Volmer equation simplifies to j = 0, reflecting the balance between oxidation and reduction. However, as η increases, one exponential term dominates, leading to an exponential rise in current density (Figure 2). This relationship enables quantitative analysis of reactant concentrations and electrochemical reaction kinetics by correlating measured current with applied overpotential.

2.2. Methods of Electrochemical Analysis

Electrochemical analysis involves the quantitative study of voltage and current dynamics in an electrochemical cell over time. This discipline employs distinct methodologies, each offering unique sensitivity and analytical capabilities. This section examines three fundamental techniques: chronoamperometry, cyclic voltammetry, and differential pulse voltammetry. All presented graphs are derived from computer simulations of electrochemical cell dynamics detailed in Appendix 1.

2.2.1. Chronoamperometry

Chronoamperometry (CA) is a fundamental electrochemical technique in which a constant potential is abruptly applied to an electrochemical cell, and the resulting current response is recorded as a function of time [17]. This method provides critical insights into electrochemical reaction mechanisms, diffusion processes, and the concentration of electroactive species in solution.

Upon application of the step potential, the current exhibits two distinct phases. First, a transient current spike occurs due to capacitive charging of the electrode-electrolyte interface, which reflects the rearrangement of charge at the double layer. This initial response is non-Faradaic in nature. Following this, the current decays over time as the electroactive species undergo diffusion-controlled redox reactions at the electrode surface. The temporal evolution of this current is governed by the Cottrell equation for simple reversible redox processes [18]:

$$I(t) = nFAc_0 \sqrt{\frac{D}{\pi t}}$$
 (7)

In this equation, I(t) represents the current at time t, n is the number of electrons transferred per redox event, F denotes Faraday's constant, A is the electrode area, c_0 is the bulk concentration of the electroactive species, and D is the diffusion coefficient. The equation assumes semi-infinite linear diffusion conditions, where the diffusion layer thickness grows with time.

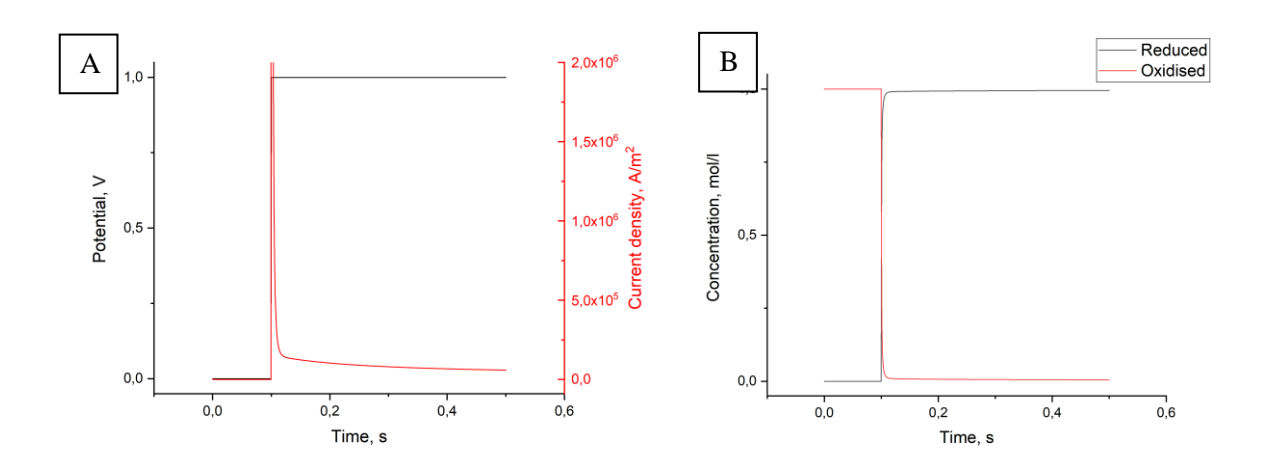


Figure 3. Computer simulation of chronoamperometry. A) The applied electrode potential and current density over time. B) The reduced and oxidized form of reactant over time near electrode surface. The simulation was carried out assuming $j_0=10000A/m^2$, $\alpha_a=\alpha_c=0.5$, T=298K, $E^0=0.5$ V, n=1.

A key analytical application of chronoamperometry lies in its ability to determine the concentration of electroactive species. By measuring the current-time response and fitting it to the Cottrell equation, one can quantitatively determine c_0 , provided the diffusion coefficient D is known or can be independently measured. Deviations from the ideal Cottrelian behavior may indicate the presence of additional electrochemical phenomena, such as coupled chemical reactions, adsorption processes, or non-linear diffusion effects.

2.2.2. Cyclic Voltammetry

Cyclic voltammetry (CV) is an electrochemical technique characterized by a triangular potential waveform, where the applied potential is linearly varied with time [20]. This method involves three distinct phases: an initial sweep from a starting potential to a predefined maximum (or minimum), a rapid potential reversal, and a return sweep to the initial value. The cycle can be repeated multiple times to study electrochemical reactions. The rate of potential change, known as the scan rate (typically expressed in V/s), is a critical experimental parameter that governs reaction kinetics and mass transport.

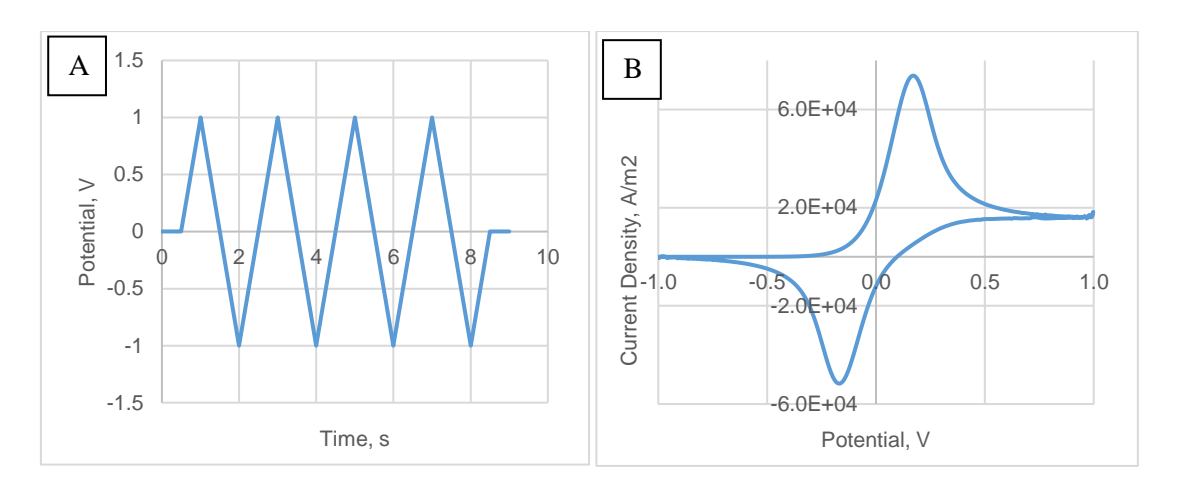


Figure 4. Cyclic voltammetry waveforms and resulting voltammogram. A) Applied potential waveform as a function of time. B) Typical voltammogram for a reversible electrochemical reaction, showing anodic and cathodic current peaks. The simulation was carried out assuming j0=10000A/m2, $\alpha_a=\alpha_c=0.5$, T=298K, $E^0=0.0$ V, n=1, bulk concentration of reduced and oxidized forms 0 M and 1 M respectfully.

For a simple reversible electrochemical reaction:

$$0x + ne \leftrightarrow Red$$
 (8)

the voltammogram exhibits two diagnostic current peaks occurring symmetrically around the standard potential of the redox couple. The Nernst equation (5) predicts that at the initial (minimal) potential, the electroactive species predominantly exists in its reduced form, while at the maximal potential, oxidized form prevails [17].

As the potential sweeps forward through the standard potential, an overpotential develops, driving the reduction reaction. This produces an initial current rise as electron transfer occurs, followed by a peak and subsequent decay as the reactant is depleted at the electrode surface [20]. The reverse sweep mirrors this behavior, with oxidation of the accumulated reduced species generating a second current peak.

The quantitative relationship between peak current (I_p) and experimental parameters is described by the Randles-Sevcik equation [18]:

$$i_n = 2.69 * 10^5 * AC\sqrt{n^3 D\nu} \tag{9}$$

This equation enables concentration determination through peak current measurements, while the peak potential positions allow identification of the electroactive species by comparison with reference redox potentials. The technique's sensitivity to both thermodynamic and kinetic parameters makes CV indispensable for studying electron transfer mechanisms, catalyst activity, and molecular interactions at electrodes.

2.2.3. Differential Pulse Voltammetry

Differential pulse voltammetry (DPV) is a sensitive and widely used electroanalytical technique that combines the advantages of controlled potential methods with advanced signal processing to achieve enhanced resolution and detection limits [20]. In DPV, the applied potential waveform consists of a linear potential sweep, or "background" voltage, composed of discrete steps, to which a small-amplitude voltage pulse is periodically added at each step. The pulse is typically applied for a short duration—usually in the range of 10 to 100 milliseconds—and its amplitude is generally in the range of a few millivolts to tens of millivolts. The potential step and pulse are repeated at fixed intervals throughout the sweep, which is usually conducted from a lower to an upper potential limit and then reversed or stopped.

During each pulse, the current response of the electrochemical system is measured twice: once at the end of the pulse (Figure 5, denoted as I_1) and once just before the pulse begins (Figure 5, denoted as I_0). The difference between these two current values, $\Delta I = I_1 - I_0$, is recorded as the electrochemical signal for the corresponding potential step and plotted against the applied base potential. This differential signal inherently subtracts out the capacitive current, which remains relatively constant during the pulse and is present in both I_1 and I_0 . As a result, the measured current is predominantly faradaic in nature, arising from the redox reaction occurring at the electrode surface.

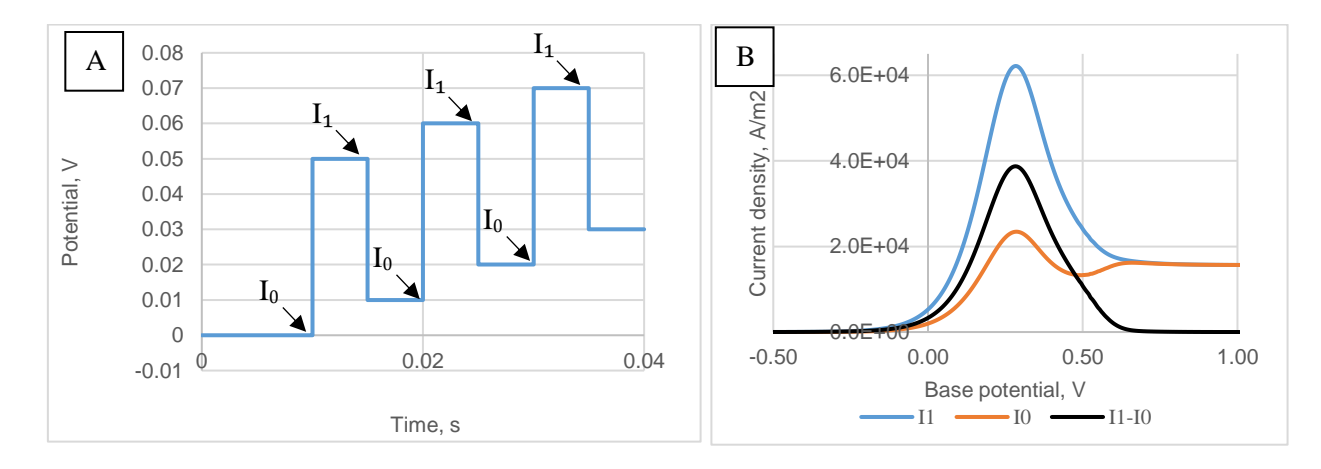


Figure 5. Differential pulse voltammetry waveforms and resulting voltammogram. A) Applied potential waveform as a function of time, With I_1 and I_0 measurement moments signified by arrows. B) Typical voltammogram for a reversible electrochemical reaction, showing anodic and cathodic current peaks. The simulation was carried out assuming j0=10000A/m2, $\alpha_a=\alpha_c=0.5$, T=298K, $E^0=0.0$ V, n=1, bulk concentration of reduced and oxidized forms 0 M and 1 M respectfully.

The theoretical basis for the superior performance of DPV lies in its ability to enhance the signal-to-noise ratio while minimizing background contributions. The subtraction of the pre-pulse current eliminates the steady-state double-layer capacitance and other non-faradaic effects, allowing for a clearer and more accurate representation of the actual electrochemical process. This is particularly advantageous when analyzing species present at low concentrations or in complex electrochemical environments where interferences are common.

Moreover, DPV provides a higher degree of peak resolution compared to conventional voltammetric techniques such as linear sweep voltammetry or cyclic voltammetry. The narrow width of the potential pulses limits the time during which diffusion can occur, thereby increasing method's sensitivity. This leads to better discrimination between closely spaced redox processes and facilitates the detection of minor components in a mixture.

An important theoretical consideration is that the small pulse amplitude ensures that the system remains close to thermodynamic equilibrium. This minimizes the perturbation of the system, preserving the accuracy of the measured electrochemical parameters such as peak potential and peak current. The combination of small perturbations and precise current subtraction makes DPV particularly well suited for studies involving fast electron transfer kinetics and reversible redox couples.

The practical utility of DPV is further enhanced by its compatibility with a variety of electrochemical cells and sensors. It is especially valuable in applications such as biosensing, environmental monitoring, pharmaceutical analysis, and the determination of electroactive species in biological and industrial samples. Its high sensitivity, low detection limits, and ability to resolve overlapping signals make it a preferred method in situations where conventional voltammetric techniques are insufficient.

2.3. Nanostructured Metal-Oxide Sensors (ZnO, CuO, Co₃O₄, NiO)

Zinc oxide (ZnO) nanostructures have emerged as a promising class of materials for electrochemical sensing due to their exceptional physical and chemical properties [16]. These include a wide bandgap (3.37 eV), high electron mobility, and excellent stability under a variety of environmental conditions [21]. The versatility of ZnO is further enhanced by its ability to be synthesized into various nanostructures, such as nanorods, nanowires, nanotubes, and nanotetrapods, each with unique morphological and functional characteristics [22]. The synthesis of ZnO nanostructures typically involves methods such as pulsed laser deposition (PLD), sputtering, sol-gel, and thermal evaporation [23] [24] [25] [26] [27]. Among these, the sol-gel method is particularly advantageous due to its low cost and scalability for large-area deposition [28]. The resulting nanostructures exhibit high surface-to-volume ratios, which are critical for enhancing the interaction with biomolecules and improving sensor performance [29] [15].

The electrochemical activity of ZnO nanostructures is further amplified by their ability to facilitate efficient electron transfer between the bioreceptor and the transducer [21]. This is crucial for biosensor applications, where low detection limits and high sensitivity are required [30]. For example, ZnO nanorods have been

immobilized with glucose oxidase (GOx) to create highly sensitive glucose biosensors, achieving rapid response times and excellent stability [31]. Similarly, ZnO nanowires have been used in amperometric biosensors for detecting hydrogen peroxide (H₂O₂), demonstrating superior sensitivity due to their high electron transport properties [32]. The integration of ZnO with other materials, such as multiwalled carbon nanotubes (MWCNTs) and chitosan, further enhances the performance of these sensors by improving conductivity and providing a stable matrix for enzyme immobilization [33] [34].

In addition to their applications in biosensors, ZnO nanostructures have shown significant potential in the detection of environmental pollutants and industrial analytes. For instance, ZnO-based phenol biosensors have been developed using electrostatic interactions between positively charged ZnO nanorods and tyrosinase enzymes, achieving a linear detection range and rapid response times [30]. ZnO nanorod arrays have also been employed in immunosensors for the detection of cancer biomarkers, such as prostate-specific antigen (PSA), demonstrating high specificity and sensitivity [35]. The ability to tailor the morphology and composition of ZnO nanostructures through controlled synthesis techniques allows for the optimization of these sensors for specific applications [22]. As research continues, the development of ZnO-based sensors is expected to play a pivotal role in advancing point-of-care diagnostics, environmental monitoring, and plant stress analysis, particularly in the context of oxidative stress biomarkers like H₂O₂ [36].

Cobalt oxide (Co₃O₄) has emerged as a pivotal material in non-enzymatic electrochemical sensing due to its tunable redox activity, high surface-to-volume ratio, and structural versatility [37] [38]. Its unique electronic properties stem from the variable oxidation states of cobalt (Co²⁺/Co³⁺), enabling efficient electron transfer and catalytic activity for a broad range of analytes, including hydrogen peroxide (H₂O₂), glucose, hydrazine, and heavy metals [39] [40]. The morphology of Co₃O₄ nanostructures—such as nanofibers, nanowires, hollow spheres, and nanocubes—can be precisely controlled via synthesis methods like hydrothermal [41], solvothermal [42], and MOF-derived pyrolysis [43]. These morphologies significantly influence performance by optimizing active site exposure and electron transport. For instance, porous Co₃O₄ nanofibers synthesized via hydrothermal methods exhibit exceptional sensitivity for H₂O₂ detection due to their high surface area and low charge transfer resistance [38]. Similarly, hierarchical structures such as urchin-like Co₃O₄ nanospheres demonstrate robust stability and wide linear ranges by minimizing interference from coexisting species [44].

The application of Co₃O₄ in non-enzymatic sensors is further enhanced through composite formation with conductive materials, such as reduced graphene oxide (rGO), carbon nanotubes (CNTs), or metal-doped frameworks. These composites address the inherent conductivity limitations of Co₃O₄ while amplifying electrocatalytic activity [45] [46]. For example, Co₃O₄/rGO composites achieve ultra-low detection limits (7.87 nM for H₂O₂) by leveraging the synergistic effects of rGO's high conductivity and Co₃O₄'s redox properties [43]. Additionally, sulfur-doped Co₃O₄ nanosheets exhibit improved selectivity for mercury ions (Hg²⁺) via enhanced surface defect density and Co²⁺/Co³⁺ valence cycling, achieving a sensitivity of 1027.46

μA μM⁻¹ cm⁻² and a limit of detection of 0.016 μM [47]. The adaptability of Co₃O₄ to complex matrices is underscored by its use in detecting H₂O₂ in plant extracts, where it demonstrates anti-interference capabilities against ascorbic acid and citric acid [48]. This positions Co₃O₄ as a promising candidate for monitoring oxidative stress in agricultural and environmental contexts.

Despite its advantages, optimizing Co₃O₄-based sensors requires addressing challenges such as morphological uniformity and long-term stability in real-world conditions [49]. Recent studies highlight the role of synthesis parameters—such as precursor ratios, calcination temperatures, and surfactant use—in tailoring nanostructure morphology for specific applications [38] [50]. For instance, ZIF-67-derived Co₃O₄ hollow spheres with uniform porosity and high metal site density enable real-time H₂O₂ monitoring in serum samples, achieving recoveries of 92.0–106.5% [38]. Furthermore, the integration of Co₃O₄ into scalable platforms like screen-printed electrodes (SPEs) and flexible substrates enhances practical applicability, as demonstrated in sensors for pharmaceuticals, heavy metals, and plant stress biomarkers [51] [52]. These advancements align with the broader goal of developing robust, low-cost electrochemical systems for in situ and point-of-care analysis, particularly in resource-limited settings where enzymatic sensors are impractical [4] [53]. By systematically refining synthesis strategies and hybrid architectures, Co₃O₄-based sensors are poised to bridge the gap between laboratory innovation and real-world deployment in biosensing, environmental monitoring, and plant health diagnostics.

Nickel oxide (NiO) has emerged as a promising metal oxide for electrochemical sensing due to its unique structural and electrochemical properties [14]. As a p-type semiconductor, NiO exhibits a high surface-to-volume ratio and excellent electron transport capabilities, making it suitable for the detection of a wide range of analytes [54]. The synthesis of NiO nanostructures, such as nanosheets, nanodentrites, and nanoflakes, can be achieved through various methods including hydrothermal, sol—gel, and chemical bath deposition [55] [56]. These methods allow precise control over morphology, surface area, and porosity, which are critical factors in enhancing sensor performance.

The high electrocatalytic activity of NiO is attributed to its ability to facilitate direct electron transfer between the analyte and the electrode surface, enhancing the sensor's response [56]. The ability to tailor the morphology and surface chemistry of NiO nanostructures through controlled synthesis techniques allows for the optimization of these sensors for specific applications. NiO has shown significant potential in the detection of biologically active molecules, for example, NiO nanoparticles were utilized for construction of metamphetamine sensor with limit of detection of 333.3 fM and linear range from 1pM to 50mM [57]. Another study demonstrated NiO-based sensor for methotrexate detection for cancer therapy, with limit of detection of 7.2 nM [58]. As research continues, the development of NiO-based sensors is expected to play a pivotal role in advancing point-of-care diagnostics, environmental monitoring, and plant stress analysis, particularly in the context of oxidative stress biomarkers like hydrogen peroxide (H₂O₂) [55].

Copper oxide (CuO) nanostructures have garnered significant attention in electrochemical sensing due to their exceptional catalytic activity, high electrical conductivity, and structural versatility. These properties make CuO an ideal candidate for the development of non-enzymatic biosensors, particularly for the detection of hydrogen peroxide (H₂O₂), glucose, and other biomarkers [59] [60]. The synthesis of CuO nanostructures, such as nanowires, nanoleaves, nanoflowers, and nanodentrites, can be achieved through various methods, including hydrothermal synthesis [59], co-precipitation [60], and laser-assisted techniques. These methods allow for precise control over the morphology and surface chemistry of the nanostructures, which in turn significantly influence their electrochemical performance.

The electrochemical activity of CuO is largely attributed to its ability to participate in redox reactions, facilitating efficient electron transfer between the analyte and the electrode surface. For example, CuO nanoflowers have been utilized in the non-enzymatic detection of glucose, demonstrating high sensitivity (1467.32 µA·mM⁻¹·cm⁻²) and a low limit of detection (12 nM) [59]. The high surface-to-volume ratio of CuO nanostructures enhances the interaction with target analytes, thereby improving the sensor's response time and sensitivity. Additionally, the integration of CuO with other materials, such as reduced graphene oxide (rGO) and chitosan, has been shown to further enhance the electrochemical performance by improving conductivity and providing a stable matrix for analyte immobilization [61] [62]. These results highlight the versatility and robustness of CuO nanostructures in various electrochemical sensing applications. Furthermore, the ability to tailor the morphology and composition of CuO through controlled synthesis techniques allows for the optimization of these sensors for specific applications, such as the detection of biomarkers [62].

This chapter has provided a comprehensive overview of the electrochemical sensing capabilities of nanostructured ZnO, CuO, Co₃O₄, and NiO, emphasizing their unique morphological and electronic features that enable high sensitivity, selectivity, and stability in both aqueous and complex biological matrices. These metal oxides, when synthesized into controlled nanostructures, offer enhanced surface-tovolume ratios, tunable redox properties, and improved electron transfer kinetics, which are essential for the development of next-generation non-enzymatic electrochemical sensors. The integration of these materials into tailored electrochemical platforms further expands their applicability in real-world scenarios, including the detection of oxidative stress biomarkers such as hydrogen peroxide in plant systems. The insights gained from this chapter lay the foundation for the subsequent experimental work in this thesis and highlight the potential of these metal oxide nanostructures to bridge the gap between laboratory-scale sensing and fielddeployable, scalable biosensing systems. Future research should focus on optimizing sensor fabrication for reproducibility, enhancing selectivity in plant-derived matrices, and integrating these systems into portable, low-cost analytical devices. The development of such sensors will not only advance electrochemical biosensing in environmental and agricultural monitoring but also contribute to the broader goals of precision agriculture, sustainable resource management, and plant stress mitigation under changing climatic conditions.

2.4. Morphology–Performance Relations in Nanostructured Electrochemical Sensors

The electrochemical sensing capabilities of nanostructured metal oxides have revolutionized analytical chemistry, offering unparalleled sensitivity, selectivity, and response times for detecting a wide range of biomolecules, environmental pollutants, and industrial analytes. The synthesis conditions—including temperature, precursor concentration, surfactant selection, reaction time, and post-treatment processes—dictate the final nanostructure morphology, which in turn influences key sensing parameters such as sensitivity, detection limit, selectivity, and stability. By systematically analyzing these relationships, this chapter provides a comprehensive framework for optimizing nanostructured sensors for specific applications, while also identifying critical gaps in the current literature that warrant further investigation.

The versatility of metal oxide nanostructures stems from their tunable physicochemical properties, which can be engineered through controlled synthesis. For example, ZnO can be synthesized as nanorods [9], nanowires [63], or hierarchical nanoflowers [64], each exhibiting distinct electrochemical behaviors due to differences in surface area, porosity, and electron transport pathways. Similarly, Co₃O₄ can be engineered into nanofibers [4], hollow nanospheres [65], or urchin-like structures [44], each offering unique advantages for non-enzymatic sensing applications. The ability to modulate these morphologies through precise synthesis parameters enables the development of sensors tailored for specific analytes, whether they be glucose, hydrogen peroxide, heavy metals, or biomarkers of disease. However, despite these advancements, challenges such as reproducibility, long-term stability, and scalability persist, necessitating further research to bridge the gap between laboratory-scale innovations and real-world applications.

The synthesis of metal oxide nanostructures involves a delicate balance of experimental parameters, each of which exerts a profound influence on the final morphology and, consequently, the electrochemical performance of the sensor. For instance, the synthesis of ZnO nanorods via hydrothermal methods typically involves temperatures ranging from 80°C to 100°C, where higher temperatures favor anisotropic growth, resulting in rod-like structures with lengths of several micrometers and diameters of hundreds of nanometers [1]. The addition of capping agents, such as cetyltrimethylammonium bromide (CTAB) [66] or polyvinylpyrrolidone (PVP) [67], can further modulate growth kinetics, promoting spherical or hexagonal morphologies under specific conditions. Similarly, the synthesis of Co₃O₄ nanowires via solvothermal methods benefits from the use of surfactants like sodium citrate [68], which not only stabilize the nanostructures but also introduce porosity, enhancing their active surface area for electrochemical reactions.

The choice of precursor compounds also plays a critical role in determining the final morphology. For example, zinc acetate and hexamethylenetetramine are commonly used in hydrothermal ZnO synthesis [1], where their molar ratio influences the nucleation and growth rates, ultimately dictating the aspect ratio of the resulting nanorods. In contrast, the use of metal-organic frameworks (MOFs) as sacrificial templates,

such as ZIF-67 for Co₃O₄ [43], enables the synthesis of hollow nanospheres with high porosity and uniform metal site density, which are highly desirable for enhancing sensor sensitivity. Post-synthesis treatments, such as thermal annealing or chemical etching, can further refine the morphology by removing residual surfactants or introducing surface defects that enhance catalytic activity.

The synthesis of hybrid nanostructures, such as ZnO@Au core-shell particles [69] or Co₃O₄/rGO composites [43], introduces additional complexity but also offers significant performance benefits. The deposition of Au nanoparticles onto ZnO nanorods, for instance, not only enhances electron transfer but also improves stability in biological matrices by preventing surface fouling. Similarly, the integration of graphene oxide (rGO) with Co₃O₄ nanofibers leverages the high conductivity of rGO while maintaining the redox properties of Co₃O₄, resulting in sensors with ultra-low detection limits and rapid response times. These examples underscore the importance of synthesis parameter optimization in achieving the desired nanostructure morphology for specific sensing applications.

The electrochemical performance of nanostructured sensors is intrinsically linked to their morphology, which governs key parameters such as surface area, porosity, electron transport pathways, and analyte accessibility. For instance, ZnO nanorods exhibit high sensitivity in glucose detection due to their porous structure [31], which facilitates efficient ion transport and enzyme immobilization, resulting in rapid response times (~1 s). However, their sensitivity is often compromised in the presence of fouling agents, necessitating surface modifications to enhance long-term stability [14]. In contrast, ZnO nanowires offer superior electron mobility along their longitudinal axis, enabling faster charge transfer and lower detection limits (as low as 0.5 nM when combined with MWCNTs) [16]. The high aspect ratio of nanowires also minimizes diffusion limitations, making them ideal for real-time monitoring applications.

Co₃O₄-based sensors demonstrate a similar morphology-dependent performance trend. Porous Co₃O₄ nanofibers synthesized via hydrothermal methods exhibit exceptional sensitivity (28.63 μ A·mM⁻¹) for hydrazine detection due to their high surface area and low charge transfer resistance [70]. However, their selectivity may be compromised in complex matrices, where interference from coexisting species can degrade performance. Hierarchical structures, such as urchin-like Co₃O₄ nanospheres, mitigate this issue by minimizing interference while maintaining wide linear ranges, making them suitable for real-world applications. The introduction of surface defects, such as through sulfur doping, further enhances selectivity for heavy metals like Hg²⁺, achieving sensitivities as high as 1027.46 μ A· μ M⁻¹·cm⁻² and detection limits of 0.016 μ M [47].

Trade-offs between sensitivity and response time are common in nanostructured sensors. For example, hierarchical ZnO nanoflowers enhance sensitivity by maximizing surface area but often suffer from slower diffusion rates due to their complex morphology [14]. Conversely, 1D nanostructures, such as Co₃O₄ nanowires, enable rapid electron transport but may require additional functionalization to improve long-term stability [37]. These trade-offs necessitate careful optimization of morphology for specific applications, balancing detection limits, linearity, and stability.

Hybrid composites, such as Co₃O₄/rGO or ZnO@Au, often combine the strengths of multiple materials, offering improved conductivity, stability, and catalytic activity. For instance, Co₃O₄/rGO composites achieve ultra-low detection limits (7.87 nM for H₂O₂) by leveraging the synergistic effects of rGO's high conductivity and Co₃O₄'s redox properties [43]. Similarly, ZnO@Au core-shell particles enhance electron transfer while maintaining the high surface area of ZnO nanorods, resulting in sensors with superior stability in biological matrices [69]. These comparisons underscore the importance of material selection and hybridization in achieving optimal sensor performance for specific applications.

Despite significant advancements, several challenges persist in the field of nanostructured electrochemical sensors. Reproducibility remains a major concern, as slight variations in synthesis conditions can lead to inconsistent nanostructure morphologies, compromising sensor performance. Scaling up production for industrial applications is another hurdle, particularly for complex architectures like tetrapodal nanostructures or MOF-derived hollow spheres. Additionally, long-term stability in biological or environmental matrices is often understudied, with fouling and degradation limiting sensor lifetimes.

2.5. Scalable and Miniaturized Fabrication (PCB, Microcells, SPEs)

The development of scalable and miniaturized electrochemical sensing platforms is a critical step in advancing the practical applicability of nanostructured metal-oxide sensors. Traditional fabrication techniques, while effective in laboratory settings, often face limitations in terms of cost, reproducibility, and compatibility with mass production requirements. Recent efforts have therefore focused on integrating nanostructured electrodes into scalable and portable systems, such as printed circuit boards (PCBs), microfluidic cells, and screen-printed electrodes (SPEs). These platforms not only enable the production of compact and robust sensor systems but also facilitate the simultaneous detection of multiple analytes in complex or low-volume samples. A notable example is the use of industrial-standard PCBs as disposable electrodes for DNA biosensing, which leverages the low-cost and high-throughput manufacturing capabilities of the electronics industry to create near-zero-cost electrochemical sensors [71].

In the study by Toldrà et al. [71], PCBs were repurposed as functional electrodes by modifying their surface chemistry through gold electroplating, enabling the immobilization of thiolated DNA capture probes. The resulting sensors were integrated with a custom-designed, open-source, and portable potentiostat, demonstrating the feasibility of low-cost, scalable, and miniaturized electrochemical detection systems. The use of PCBs as a substrate not only ensures high reproducibility in electrode fabrication but also allows for the integration of multiple functional layers, such as microfluidics, sensors, and electronics, into a single device. This approach aligns well with the broader goal of creating lab-on-a-chip systems that are both cost-effective and suitable for point-of-care applications [72] [73].

The integration of PCB-based sensors with portable electronics represents a significant advancement in the field of electrochemical sensing. The open-source potentiostat developed in this study was designed to be low-cost, compact, and capable of performing common electrochemical techniques such as cyclic

voltammetry (CV), chronoamperometry (CA), and square-wave voltammetry (SWV) [71]. With a potential range of -2.9 to +0.4 V and a current range of -20 to +10 μ A, the potentiostat is well-suited for on-site analysis, particularly in resource-limited settings. The system's low power consumption (50 mW) and compatibility with USB interfaces make it highly adaptable for field deployment. Furthermore, the modular design of the potentiostat allows for future enhancements, such as the inclusion of battery power and wireless communication, which would further improve its portability and usability [71] [74].

Microfluidic integration is another key aspect of scalable and miniaturized electrochemical platforms. The study demonstrated the potential of PCBs to support microfluidic systems by utilizing epoxy-based solder masks as liquid barriers, thereby enabling the precise control of sample flow and reagent delivery [71]. This is particularly important for applications requiring high-throughput or in situ analysis, where the ability to manage small volumes and prevent cross-contamination is crucial. The integration of microfluidics with PCB-based electrodes not only enhances the analytical performance of the sensor but also facilitates the automation of detection processes, reducing the need for manual intervention [72].

Screen-printed electrodes (SPEs) have become a fundamental technology in the advancement of portable, cost-effective, and highly reproducible electrochemical sensors [75]. Their fabrication through thick-film deposition on plastic or ceramic substrates allows for straightforward, economical, and rapid on-site analysis with exceptional reproducibility, sensitivity, and accuracy [76]. The scalability of SPE production makes them particularly well-suited for applications requiring disposable sensors, such as point-of-care diagnostics, environmental monitoring, and food safety testing [76]. Their adaptability stems from the ability to fabricate them using various conductive materials—including gold, silver, platinum, and carbon—and to enhance their electrochemical performance through nanomaterial modifications [77].

A major advantage of SPEs is their seamless integration with miniaturized electrochemical systems. Unlike conventional glassy carbon or platinum electrodes, SPEs can be effortlessly incorporated into microfluidic devices, enabling precise control over sample volumes and reagent delivery [78]. Their planar design allows for straightforward functionalization with recognition elements—such as enzymes, DNA probes, or antibodies—via techniques like drop-casting, electrodeposition, or ink mixing [79]. This versatility has paved the way for disposable biosensors capable of detecting a broad spectrum of analytes, including hydrogen peroxide (H₂O₂), heavy metals, and biomolecules [80] [81].

The combination of SPEs with portable potentiostats further enhances their utility for field applications. Modern SPE-based systems often feature compact, open-source potentiostats capable of performing techniques like cyclic voltammetry (CV), chronoamperometry (CA), and square-wave voltammetry (SWV) [75]. These devices are engineered for low cost, energy efficiency, and wireless connectivity, making them ideal for remote sensing and real-time monitoring [82]. Additionally, integrating SPEs with microfluidic channels (e.g., paper-based or polymer-based) enables automated sample processing, reducing manual handling and improving assay consistency [83].

However, ensuring batch-to-batch reproducibility remains a challenge, particularly when modifying SPEs with nanomaterials. Electrochemical pretreatment methods, such as cyclic voltammetric conditioning or potential stepping, are frequently employed to activate the electrode surface and optimize electron transfer kinetics [84] [85]. Furthermore, the incorporation of conductive inks—containing materials like graphene, carbon nanotubes, or metal nanoparticles (e.g., gold, platinum)—can significantly enhance sensitivity and stability [86] [87]. The composition of these inks, including conductive particles, binders, and solvents, critically influences the electrochemical performance of the resulting electrodes [81] [88].

Despite their benefits, SPEs are currently constrained to planar substrates, limiting their use in non-flat geometries. Future advancements in flexible electronics and 3D printing may mitigate this restriction by enabling the development of conformal and wearable sensors [78]. Continued innovation in SPE-based platforms, coupled with progress in nanomaterial modifications and portable electronics, holds significant potential for expanding electrochemical sensing applications in both laboratory and field settings.

The incorporation of metal oxide nanostructures into scalable and miniaturized electrochemical platforms—such as PCB-based sensors, microfluidic cells, and SPEs—marks a significant advancement toward practical, field-deployable sensing systems. This chapter demonstrates how these technologies address traditional constraints in cost, reproducibility, and portability, facilitating real-world applications in environmental diagnostics and plant stress monitoring. By utilizing low-cost fabrication methods and open-source electronics, these platforms enable high-throughput, selective, and sensitive analyte detection, particularly in complex matrices like plant extracts. Future research should focus on refining nanomaterial integration with these scalable systems, addressing challenges such as long-term stability in harsh environments and further miniaturization for wearable or in vivo applications.

2.6. H₂O₂ Detection in Plant and Complex Matrices for Oxidative Stress Monitoring

Hydrogen peroxide (H₂O₂) is a pivotal plant signaling molecule and oxidative stress biomarker, playing dual roles in cellular regulation and damage under abiotic and biotic stresses [89]. Its real-time, in situ detection in plants is critical for understanding stress responses, optimizing agricultural practices, and developing early warning systems for crop health. Electrochemical sensors have emerged as a promising alternative to traditional analytical methods (e.g., fluorescence-based assays) due to their portability, cost-effectiveness, and compatibility with complex biological matrices.

The choice of electrode material and modification strategies significantly influences sensor performance. Platinum (Pt) has been widely used due to its high catalytic activity toward H₂O₂ reduction and oxidation. A dual-functional Pt disk microelectrode was employed to detect H₂O₂ in Agave tequilana leaves after bacterial treatment, revealing dynamic changes in H₂O₂ release during pathogen colonization [90].

However, the high cost of Pt electrodes limits their scalability, necessitating the exploration of alternative materials. Stainless steel (SS) wires, modified with electrodeposited gold nanoparticles (AuNPs), have been successfully used for in situ H₂O₂ monitoring in tomato leaf veins under salinity stress. The AuNP modification enhanced electron transfer kinetics, improving sensitivity and selectivity while maintaining low fabrication costs [91].

Nanomaterial-based modifications further enhance sensor performance. Palladium nanoparticles (PdNPs) and carbon nanomaterials (e.g., reduced graphene oxide, MWCNTs) have been integrated into glassy carbon electrodes (GCEs) to detect H₂O₂ in Arabidopsis leaves under salt stress [92]. Similarly, polyoxometalate-modified electrodes demonstrated improved sensitivity and stability for H₂O₂ detection in plant extracts, offering a non-enzymatic alternative to traditional enzymatic sensors [93]. These modifications exploit the high surface area and catalytic properties of nanomaterials to lower detection limits and enhance response times.

Plant tissues present unique challenges for electrochemical sensing, including low analyte concentrations, matrix interference, and physical barriers to electrode insertion. Carbon fiber electrodes, while sensitive, struggle with mechanical resilience, making SS wires a more practical alternative for penetrating plant tissues [94]. Paper-based analytical devices (PADs) coupled with AuNP-modified indium tin oxide (ITO) electrodes have been used to detect H₂O₂ in tomato leaves infected with Botrytis cinerea, demonstrating the feasibility of minimally invasive sampling [91]. Additionally, 3D-printed hollow microarrays integrated with screen-printed electrodes (SPEs) facilitated H₂O₂ extraction and detection in leaves, addressing issues of electrode size and sample access [95].

Selectivity remains a critical challenge, as plant extracts contain numerous redox-active species (e.g., ascorbic acid, glucose, citric acid). The SS electrode modified with carbon cement and MWCNTs exhibited selective H₂O₂ detection in tomato leaf veins, ignoring interferents like malic acid and jasmonic acid [92]. However, further optimization is needed to mitigate cross-reactivity in complex matrices. Enzymatic sensors, such as horseradish peroxidase (HRP)-modified electrodes, offer high selectivity but suffer from enzyme degradation and limited stability [96]. Non-enzymatic sensors, leveraging metal oxide nanoparticles (e.g., Co₃O₄, NiO) or conductive polymers, present a more robust alternative for long-term monitoring.

The integration of electrochemical sensors with automated measurement systems could enable real-time data analysis and automated stress detection in agricultural settings. Flexible sensors, based on conductive polymers or nanomaterial-coated textiles, hold promise for non-invasive, long-term monitoring of plant health. Additionally, the development of multi-analyte sensors capable of detecting H₂O₂ alongside other stress-related molecules (e.g., nitric oxide, salicylic acid) would provide a more comprehensive understanding of plant stress responses.

Standardizing sensor fabrication and validation protocols is essential for translating laboratory successes into practical agricultural tools. The miniaturization of electrochemical sensors, coupled with advancements in microfabrication (e.g., PCB-based chips, droplet-based microcells), could facilitate their deployment in field settings. Furthermore, the use of machine learning algorithms to interpret electrochemical signals could enhance sensor accuracy and adaptability to varying environmental conditions.

In summary, electrochemical sensors offer a versatile platform for H₂O₂ detection in plants, with significant potential for advancing precision agriculture and environmental monitoring. Addressing challenges in selectivity, scalability, and real-world applicability will be key to realizing their full potential in plant stress research.

3. Synthesis and Morphological Characterization of Metal Oxide Nanostructures

3.1. Laser-assisted and Hydrothermal Synthesis of ZnO Nanoneedles with Tailored Morphology

Zinc oxide (ZnO) is a versatile semiconductor material that is widely used in optoelectronic devices, sensors, and catalytic applications. Among its various nanostructural forms, ZnO nanoneedles have attracted significant attention due to their high surface-to-volume ratio and unique physical and chemical properties. The controlled synthesis of ZnO nanoneedles with tailored morphology is essential for optimizing their performance in specific applications. Two prominent methods for synthesizing ZnO nanoneedles are the hydrothermal method and laser-assisted synthesis.

Hydrothermal synthesis is a widely adopted technique for the fabrication of ZnO nanostructures [2]. It involves the reaction of metal precursors in a water-based solution under elevated temperature and pressure. This method facilitates the growth of uniform and well-aligned ZnO nanoneedles due to its low-temperature, solvent-based, and scalable nature. In the context of the hydrothermal approach, the growth of ZnO nanorods and nanoneedles can be influenced by various parameters such as pH, precursor concentration, temperature, and the presence of seed layers. Hydrothermal synthesis was employed in this study to fabricate ZnO nanostructures from an equimolar solution of Zn(NO₃)₂ and Hexamethylenetetramine (HMTA) (0.025 M and 0.05 M, respectively) [2]. The synthesis was carried out in a programmable oven at 90 °C for 1.5 hours, resulting in the formation of well-aligned ZnO nanoneedles on pre-deposited ZnO seed layers. The seed layers were applied via drop-casting of a 25 mM zinc acetate solution in ethanol, followed by thermal annealing at 350 °C for 30 minutes.

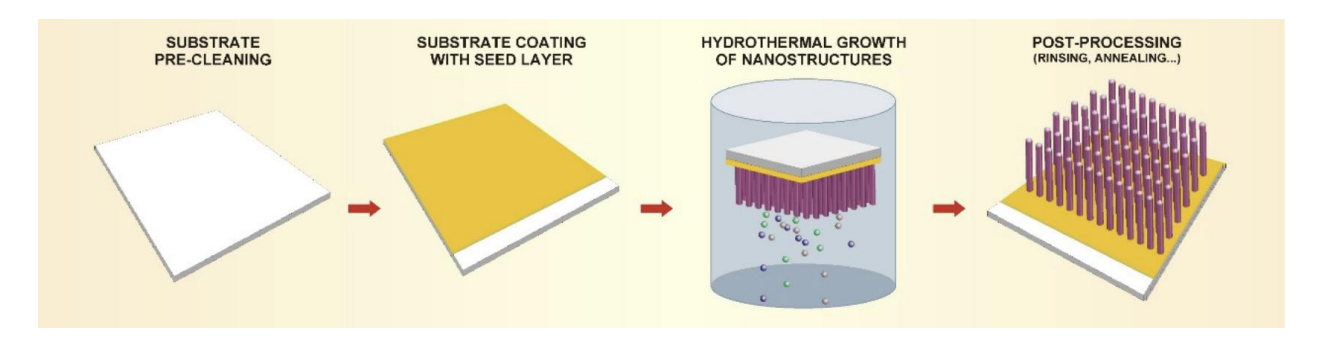


Figure 6. Basic process of hydrothermal synthesis [2].

The hydrothermal process was initiated by placing the substrate with the pre-deposited ZnO seed layer into a reaction vessel containing the solution of Zn(NO₃)₂ and HMTA [2]. The vessel was then sealed and placed in the oven, where it was heated to 90 °C for the duration of the reaction (Figure 6). The elevated temperature promotes the decomposition of HMTA, releasing ammonia (NH₃) and increasing the pH of the solution. This leads to the formation of OH⁻ ions, which are critical for the nucleation and growth of ZnO

nanostructures. The increased pH environment accelerates the reaction, allowing the nanostructures to grow perpendicularly on the seed layer in a well-ordered and uniform manner. After the growth process, the samples were rinsed with distilled water and either air-dried or sonicated to remove any unwanted nanostructures that may have formed in non-targeted areas. This method not only ensures high-quality ZnO nanostructures but also offers the advantage of being a low-temperature and scalable technique suitable for various applications such as sensors and electrode fabrication.

The zinc acetate solution was applied to the substrate via drop-casting. In this process, a 25 mM zinc acetate solution in ethanol was deposited onto the surface of the substrate. To investigate the effect of seed layer uniformity on nanostructure growth, the application was conducted under two different thermal conditions: (1) on a room-temperature substrate, and (2) on a preheated substrate at 100 °C. Scanning electron microscopy (SEM) analysis revealed a significant difference in the resulting nanostructural morphology (Figure 7). On room-temperature substrates, the seed layer exhibited a ring-like pattern due to the "coffee stain" effect [97], which led to heterogeneous ZnO nanostructure growth—dense, vertically aligned nanoneedles along the periphery and sparse, 3D nano-urchin-like formations in the center. In contrast, preheating the substrate effectively suppressed thermocapillary convection, promoting a more uniform evaporation of the solvent and, consequently, a homogeneous distribution of seed particles. This, in turn, resulted in a more even and uniform growth of nanoneedles across the surface, as evidenced by the SEM images.

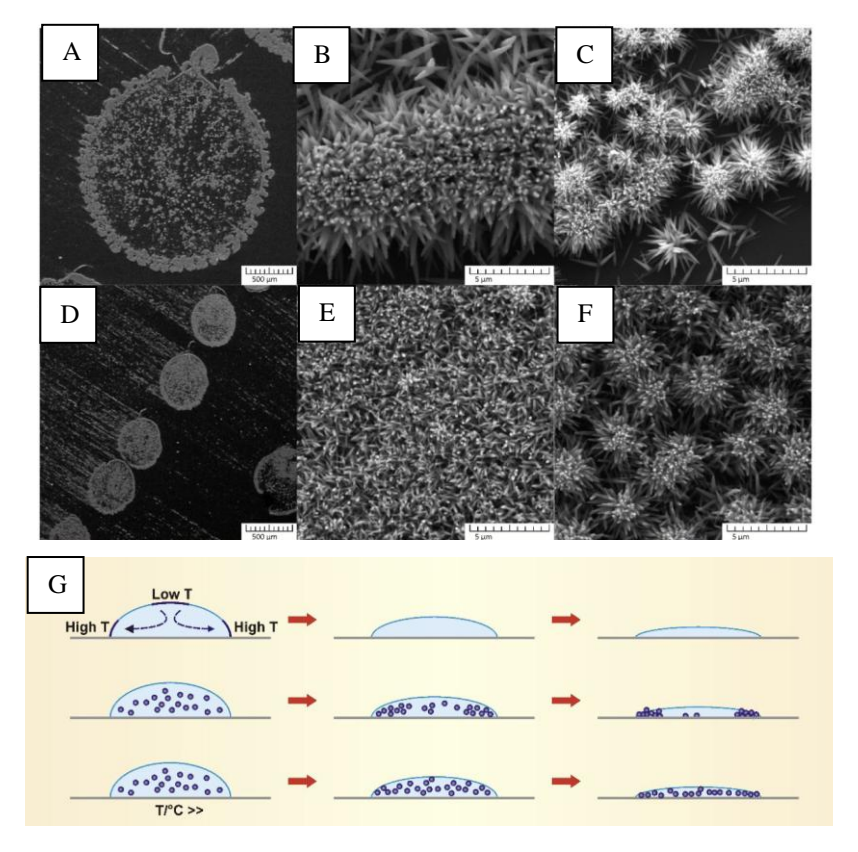


Figure 7. Analysis of the "cofee stain" efect, where (a), (b), and (c) nanostructures were obtained by applying ZnO precursors on a room-temperature substrate, and (d), (e), and (f) on a pre-heated substrate [2]. Hydrothermal synthesis was carried out in 0.025 M Zn(NO3)2 and 0.05 M HMTA aqueous solutions at 90 °C for 1.5 h. (g) Graphic illustration of the cofee stain efect formation process [97].

To further enhance selectivity and minimize parasitic nanostructure growth in non-seeded areas, a protective glass screen was employed during the hydrothermal process. The screen was positioned at a 2–3 mm gap from the substrate surface. The use of the protective screen significantly reduced the deposition of unintended nanostructures on non-seeded regions. Specifically, samples grown without a screen exhibited noticeable nanostructure growth in the interdroplet regions, whereas those grown under the screen showed negligible or no nanostructure growth outside the targeted area. This result was corroborated by multiple repetitions of the experiment under identical hydrothermal conditions, confirming the effectiveness of the protective screen in improving the selectivity and quality of the nanostructured coatings [2].

In addition to the application of protective screens, the influence of laser-assisted selective thermal decomposition of zinc acetate was explored as an alternative method to create patterned seed layers [1]. A 532 nm laser with a power of 60 mW and a scan speed of 55 mm/min was used to irradiate a spin-coated zinc acetate layer deposited on a Cr-coated substrate Figure 8. The laser-induced thermal decomposition selectively converted zinc acetate into ZnO seeds along the irradiated trajectory, enabling the formation of patterned nanostructures after subsequent hydrothermal growth. SEM analysis confirmed that the laser method produced well-defined, micron-scale ZnO nanoneedle patterns with sharp boundaries and high fidelity to the laser path [1]. Notably, the morphology of the nanostructures obtained via laser-assisted seeding was indistinguishable from those obtained using furnace-annealed seed layers, as confirmed by XRD and EDS analysis. Both techniques yielded ZnO nanostructures with high crystallinity and no secondary phases [2].

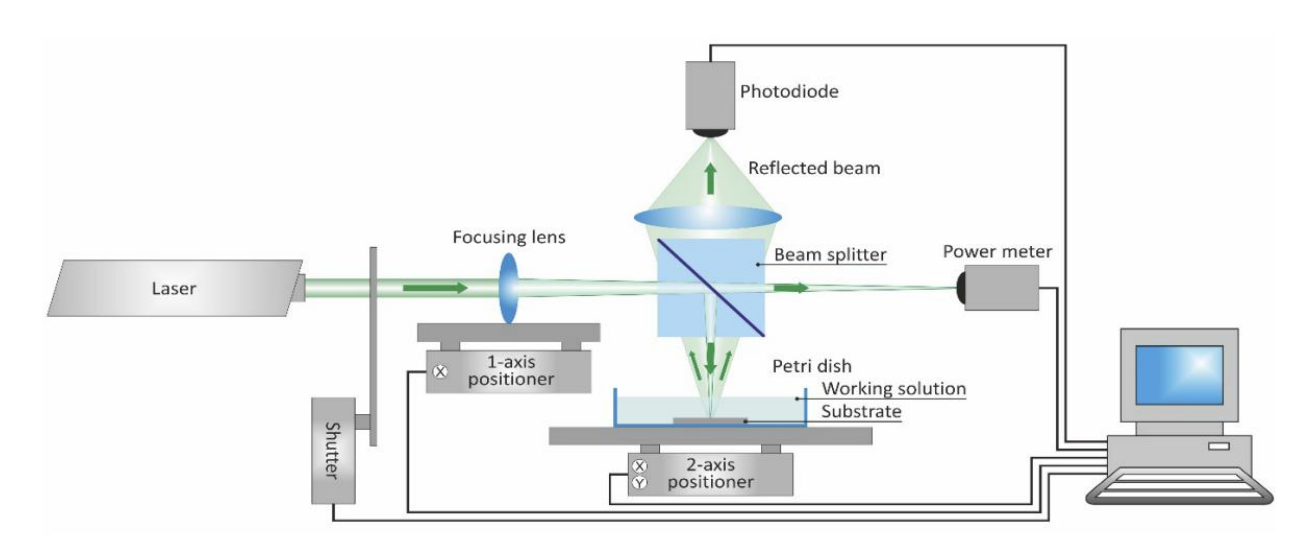


Figure 8. Schematic representation of the setup for laser-induced hydrothermal synthesis [1].

To further test the reproducibility and scalability of the laser-assisted method, multiple samples with varying line widths were produced by adjusting the laser power between 50 and 160 mW. The results demonstrated a direct correlation between laser power and the width of the seeded lines, with higher power leading to wider lines due to increased thermal diffusion in the metal layer. However, the morphology of the resulting nanostructures remained consistent across all samples, indicating that the laser-assisted

method does not affect the structural quality of the ZnO nanostructures beyond the initial seed layer formation. Importantly, post-growth ultrasonic treatment effectively removed parasitic nanostructures formed in unirradiated regions, although some residual nanostructures were observed in cases where the Cr substrate provided unintended nucleation sites [1].

Further incorporating the data from the laser-induced hydrothermal synthesis study, it becomes evident that the manipulation of external thermal stimuli—particularly through localized laser irradiation—can significantly refine the morphology and spatial distribution of ZnO nanostructures. When equimolar solutions of Zn(NO₃)₂ and HMTA are exposed to laser heating, the resulting microstructures exhibit a pronounced dependence on both laser power and exposure duration. At 50 mW and 120 seconds, for instance, the synthesis yields well-defined microrods with a relatively uniform height and diameter, but increasing the laser power to 80–100 mW while maintaining the same time leads to greater height variation (Figure 10) and the emergence of two distinct growth regions: a central high-area and a surrounding lowarea (Figure 11). This dual-regime growth is attributed to the radial temperature gradient created by the laser spot, where the central zone experiences more intense heating, accelerating growth kinetics and promoting taller nanostructures [1]. Such insights highlight the importance of laser parameters in determining not only the size but also the spatial uniformity of the microstructures, offering a powerful tool for selective patterning in advanced applications.

Moreover, the introduction of polyethyleneimine (PEI) into the synthesis solution dramatically alters the growth dynamics. PEI acts as a capping agent that preferentially interacts with specific ZnO crystal facets, thereby directing anisotropic growth and promoting longer, more elongated nanorods. Specifically, in experiments with 0.20 M PEI, the addition significantly reduces the height variation among microstructures and accelerates their growth, leading to a more consistent length across the irradiated area. However, this enhanced growth rate comes with trade-offs: the vertical alignment of the microstructures is compromised, and parasitic structures begin to form outside the intended growth region, blurring the boundary between patterned and unpatterned areas. These findings underscore the complex interplay between surfactant-assisted growth and spatial control, suggesting that while PEI can be beneficial for achieving longer microrods, its use must be carefully balanced with other parameters to maintain structural fidelity and minimize unwanted deposition.

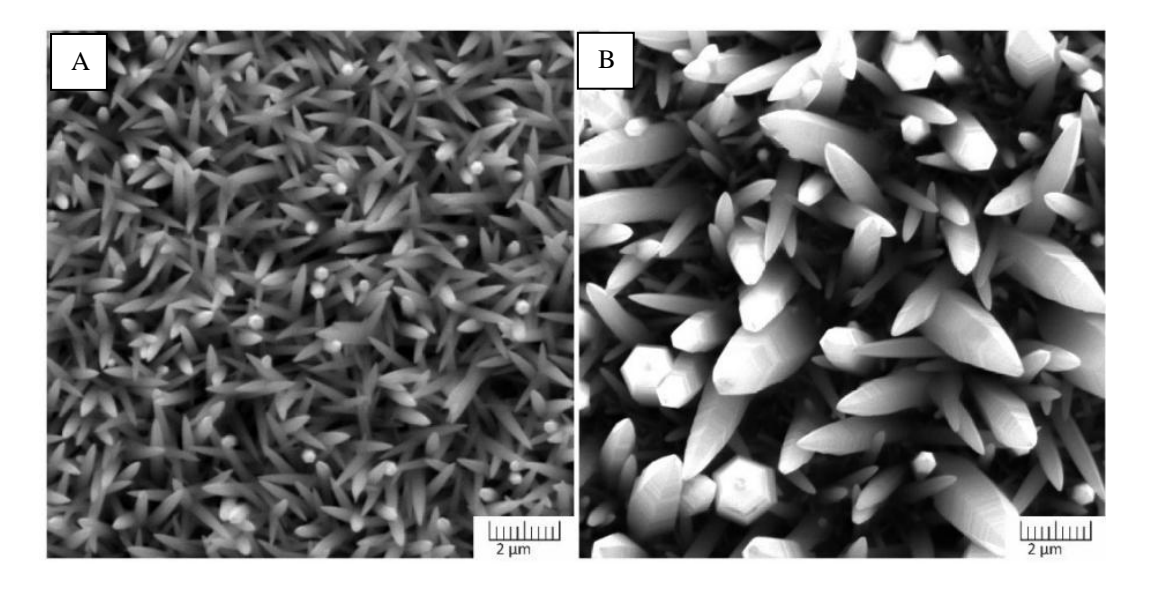


Figure 9. The effect of precursor concentration on ZnO microstructures. A) 0.0125 M zinc acetate; b) 0.2M zinc acetate [1].

Finally, the study also revealed that while higher reagent concentrations (e.g., 0.2M) can lead to larger nanostructures, they often do so at the expense of morphological consistency (Figure 9). The increased precursor availability leads to rapid nucleation and growth, but the high density of adjacent nanostructures inhibits surface diffusion, preventing the formation of the ideal hexagonal prisms. Instead, the nanostructures adopt a needle-like or agglomerated morphology due to the "hit and stick" mechanism of precursor deposition [1]. This phenomenon aligns with the observed effects in the furnace-annealed seed layer approach, where higher zinc acetate concentrations in the seeding solution led to denser but less uniform nanoneedle arrays. Therefore, while higher concentrations may be desirable for certain applications requiring larger structures, they necessitate careful optimization of other parameters—such as laser power and irradiation time—to achieve the desired balance between growth rate and structural regularity.

Finally, the electrochemical deposition method was assessed for its ability to selectively coat metal electrodes with ZnO nanostructures. Using a 0.005 M Zn(NO₃)₂·0.1 M NaNO₃ solution and a current density of 90 μA/cm² at 80 °C, dense and uniform ZnO nanoneedles were selectively deposited on Cr-coated electrodes without requiring a seed layer. The interelectrode spaces remained free of nanostructures, demonstrating the method's inherent selectivity. SEM imaging confirmed the high density and uniformity of the nanoneedles, with no observable defects or secondary phases detected via EDS and XRD analysis. The method's precision, speed, and ability to produce sub-micron-scale features make it particularly suitable for applications where high-resolution and area-selective nanostructured coatings are required.

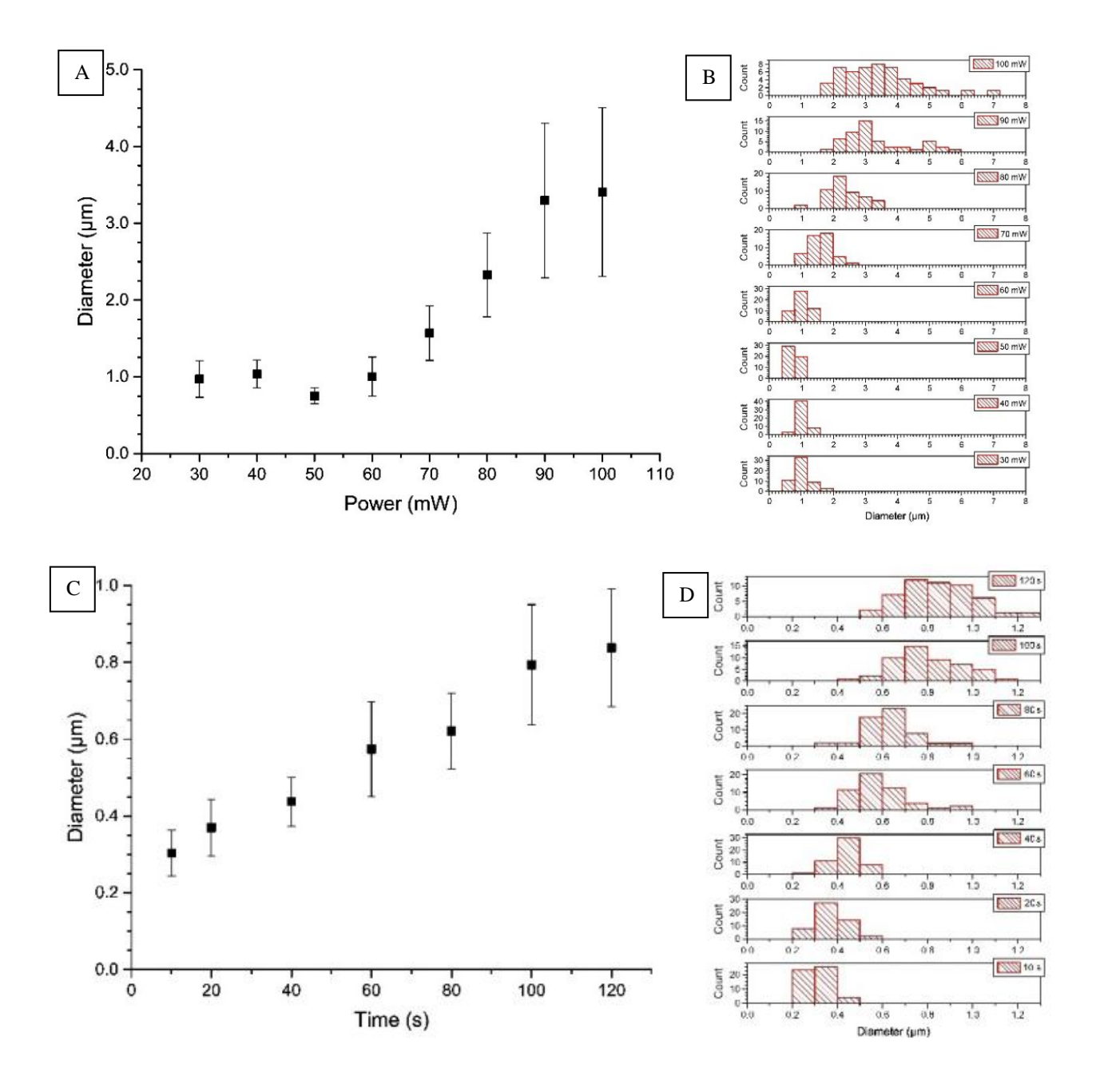


Figure 10. The effect of laser power and exposure time on ZnO structure size. A, B) The diameters of the synthesised rods depending on the incident beam power. C, D) The diameters of the synthesised rods depending on the synthesis time. [1].

In summary, the experimental results demonstrate that hydrothermal synthesis can be effectively modified through the use of protective screens, laser-assisted patterning, and electrochemical deposition to achieve high-quality, area-selective ZnO nanostructured coatings. These techniques offer valuable strategies for tailoring nanostructure morphology and growth selectivity, with direct applicability in sensor fabrication, optoelectronics, and biosensing technologies.

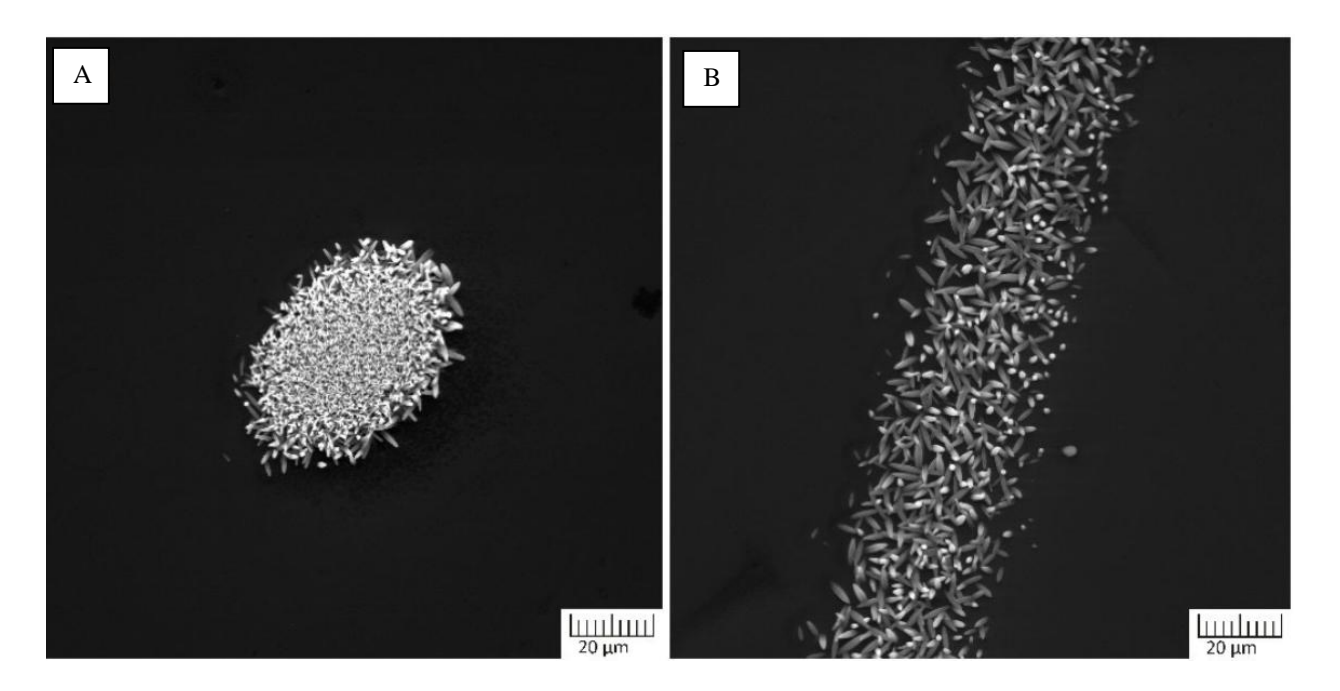


Figure 11. Samples of laser-induced hydrothermally synthesized ZnO oxide microstructures.

A) single dot, B) continuous line [1].

Another critical factor influencing the morphology and alignment of ZnO nanostructures is the initial seed layer. In the context of laser-assisted hydrothermal synthesis, the study revealed that the use of a dense, uniformly distributed seed layer—such as a 10 nm thick magnetron-sputtered ZnO film—plays a central role in promoting vertical alignment through competitive growth. In such cases, nanostructures oriented along the (0001) crystallographic axis outcompete those growing at oblique angles due to the energetic favorability of vertical growth. Conversely, in regions with sparse or non-uniform seed distributions, nanostructures exhibit lateral growth tendencies, leading to the formation of urchin-like or pyramidal morphologies. This highlights the importance of seed layer quality in hydrothermal processes: not only does it dictate the initial nucleation sites, but it also governs the subsequent growth direction and uniformity. These observations are consistent with the controlled seed layer application described in the study, where preheating substrates prior to zinc acetate deposition suppressed convective effects and led to a more homogeneous seed distribution, ultimately enhancing the uniformity of the resulting nanoneedles.

The wettability dynamics of ZnO nanostructured surfaces are closely tied to their morphology, size, and surface coverage [9]. According to the study, nanostructured ZnO thin films exhibit a wide range of wetting behaviors, from highly hydrophobic to distinctly hydrophilic. For instance, ZnO nanoneedles, characterized by a low surface coverage of approximately 23%, displayed a very high initial water contact angle (WCA) of 127°, which decreased to 70° after 10 minutes [9]. This behavior is attributed to the needle-like shape and low surface coverage that promote the formation of an air-trapping "Fakir" or "lotus" surface, consistent with the Cassie–Baxter wetting regime [98]. In contrast, thick nanorods with a high surface coverage (87%) showed a marked hydrophilic behavior, with a WCA of only 19° at the onset of the experiment, dropping further to 7.5° after 10 minutes, indicating a transition to the Wenzel regime where the liquid fully penetrates the nanostructure gaps.

The nanoplate morphology, with a relatively high surface coverage and an increased area of metastable [0002] planes, demonstrated even more pronounced hydrophilic characteristics, with an initial WCA of 12° that reduced to 3° within 10 minutes. This result highlights the role of the dominant (0002) plane in enhancing surface hydrophilicity. ZnO nanotubes, despite having a moderate surface coverage (40%), also showed strong hydrophilicity with an initial WCA of 40°, which decreased to 17° after 10 minutes. The enhanced wettability is likely due to a high density of active adsorption sites on the inner walls of the nanotubes, created during the etching process.

The study further utilized electrochemical impedance spectroscopy (EIS) to track wetting dynamics in real time [9]. The saturation time, defined as the moment when all nanostructure voids are fully wetted, varied significantly between morphologies. Hydrophobic surfaces, such as nanoneedles and thin rods, required 7–9 minutes to reach saturation, while hydrophilic surfaces, such as thick rods and nanoplates, achieved full wetting in just 2–4 minutes. EIS provided detailed insights into the transition from the Cassie–Baxter to the Wenzel wetting model, with the impedance measurements reflecting the progressive filling of nanostructure voids by water. These findings underscore the importance of considering nanostructure morphology in the design of electrochemical and optical sensors, where complete surface wetting is essential for optimal performance.

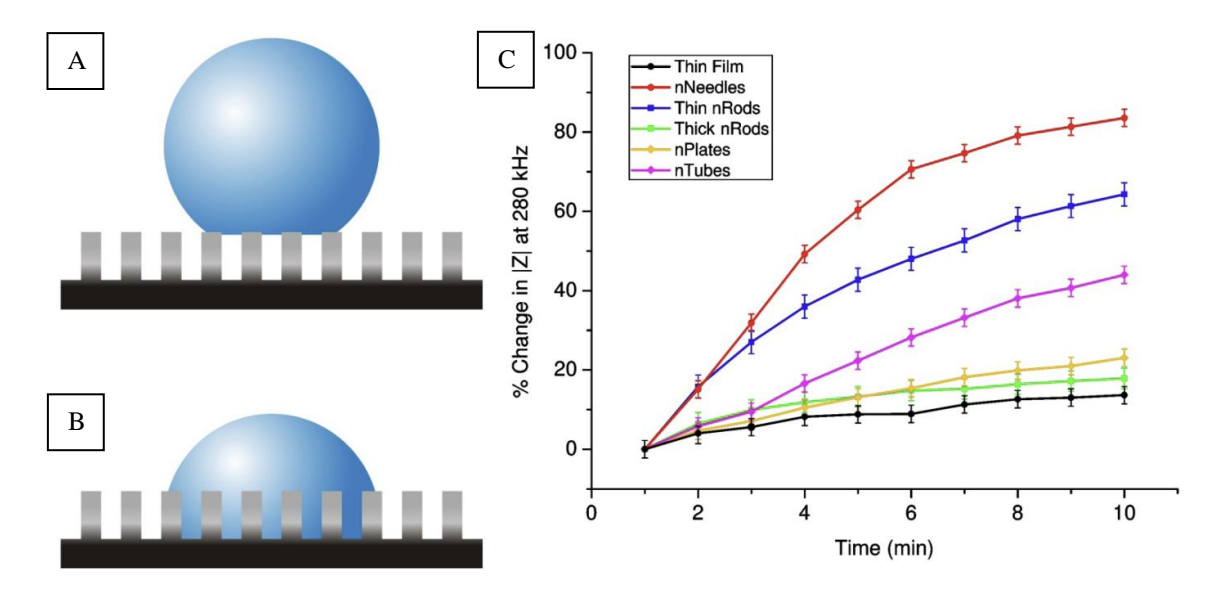


Figure 12. Schematic illustration of (a) Cassie–Baxter and (b) Wenzel regimes of nanostructure wettability. (c) Characterization of water permeation progress by relative change of the impendance module |Z| versus time for different ZnO nanostructure morphologies at 280 kHz [9].

3.2. Synthesis and Morphological Characterization of Copper Oxide Nanostructures

Copper oxide (CuO) nanostructures have been synthesized using two different methods: a one-step chemical hydrothermal oxidation route and thermal oxidation [3]. These methods produce nanostructured CuO films on copper wire substrates, which exhibit high homogeneity, adhesion, and electrochemical sensitivity. The resulting nanostructures were characterized using field-emission scanning electron microscopy (FESEM), energy-dispersive spectroscopy (EDS), and X-ray diffraction (XRD) to analyze their morphology, composition, and crystallinity.

The hydrothermal synthesis method was employed to create nanostructured CuO coatings on copper wire substrates. This method involved the immersion of copper wire in a solution composed of 10 mL of 10 M NaOH, 5 mL of 1 M (NH₄)₂S₂O₈, and 26 mL of distilled water. The wires were immersed in the solution and placed in a heat-resistant glass beaker inside an oven preheated to 90 °C for 3 hours. The process was followed by thorough rinsing with distilled water and drying at 90 °C for 3 hours. The hydrothermal growth of CuO nanostructures followed a series of chemical reactions [3]:

$$Cu + 2 NaOH + (NH_4)_2 S_2 O_8 \rightarrow Cu(OH)_2 + Na_2 SO_4 + (NH_4)_2 SO_4$$
 (10)

$$Cu(OH)_2 + 2OH^- \rightarrow [Cu(OH)_4]^{2-}$$
 (11)

$$[Cu(OH)_4]^{2-} \rightarrow CuO + 2OH^- + H_2O$$
 (12)

At a higher concentration of NaOH (10–15 M), the dissolution–secondary precipitation mechanism activates, which involves the formation of Cu(OH)₂ and its reaction with OH⁻ ions to form the complex [Cu(OH)₄]²⁻. These complex ions then decompose to CuO, releasing hydroxyl ions and water. The resulting nanostructures on the copper wire exhibited a dense, uniform layer of CuO nanopetals, with 3D flower-like formations (Figure 13 A).

The CuO nanostructures formed via hydrothermal oxidation demonstrated excellent adhesion to the copper surface and mechanical stability during post-processing. The surface morphology showed a high degree of uniformity and a large surface area due to the porous and hierarchical arrangement of the nanostructures.

In comparison, the CuO film obtained via thermal oxidation was prepared by annealing copper wire in an oxygen atmosphere at 500 °C for 30 minutes. The process resulted in a polycrystalline, homogeneous CuO film composed of irregularly shaped grains. However, this film exhibited poor adhesion to the substrate and was mechanically less stable than the hydrothermally synthesized nanostructures.

Field emission scanning electron microscopy (FESEM) was used to analyze the surface morphology of the CuO nanostructures. The results showed a dense and uniform CuO layer composed of nanopetals approximately several nanometers thick. The nanostructures formed micrometer-sized 3D flower-like formations, which contributed to an increased surface area and enhanced electrochemical activity [3].

X-ray diffraction (XRD) analysis confirmed the high crystallinity of the CuO nanostructures. The XRD pattern showed the presence of only crystalline CuO phases, indicating high purity with no extraneous inclusions. The diffraction peaks were consistent with the CuO (tenorite) lattice, with dominant orientations corresponding to the (002) and (111) planes [3]. The XRD pattern for the hydrothermally synthesized CuO film displayed a higher degree of crystallinity compared to the thermally oxidized CuO film.

The influence of the hydrothermal synthesis time on the morphology and electrochemical performance of the CuO nanostructures was studied by varying the synthesis duration to 1 h, 3 h, and 6 h. FESEM images revealed that [3]:

- 1 h of synthesis produced nanopetals with greater thickness and lower height, resulting in a reduced active surface area and sensitivity.
- 3 h of synthesis (the optimal time) produced nanostructures with the most uniform and densely packed morphology, leading to the highest electrochemical sensitivity.
- 6 h of synthesis caused the nanostructures to aggregate and form dense spherical formations, which decreased the accessible surface area and electrochemical activity.

The optimal synthesis time of 3 h was determined to provide the best balance of morphology, surface area, and electrochemical sensitivity for H₂O₂ detection. Energy-dispersive spectroscopy (EDS) confirmed the chemical purity of the CuO nanostructures. The EDS microanalysis showed that the samples consisted of 58.96 atom % Cu and 41.04 atom % O, with no detectable foreign impurities, confirming the high quality of the synthesized CuO nanostructures.

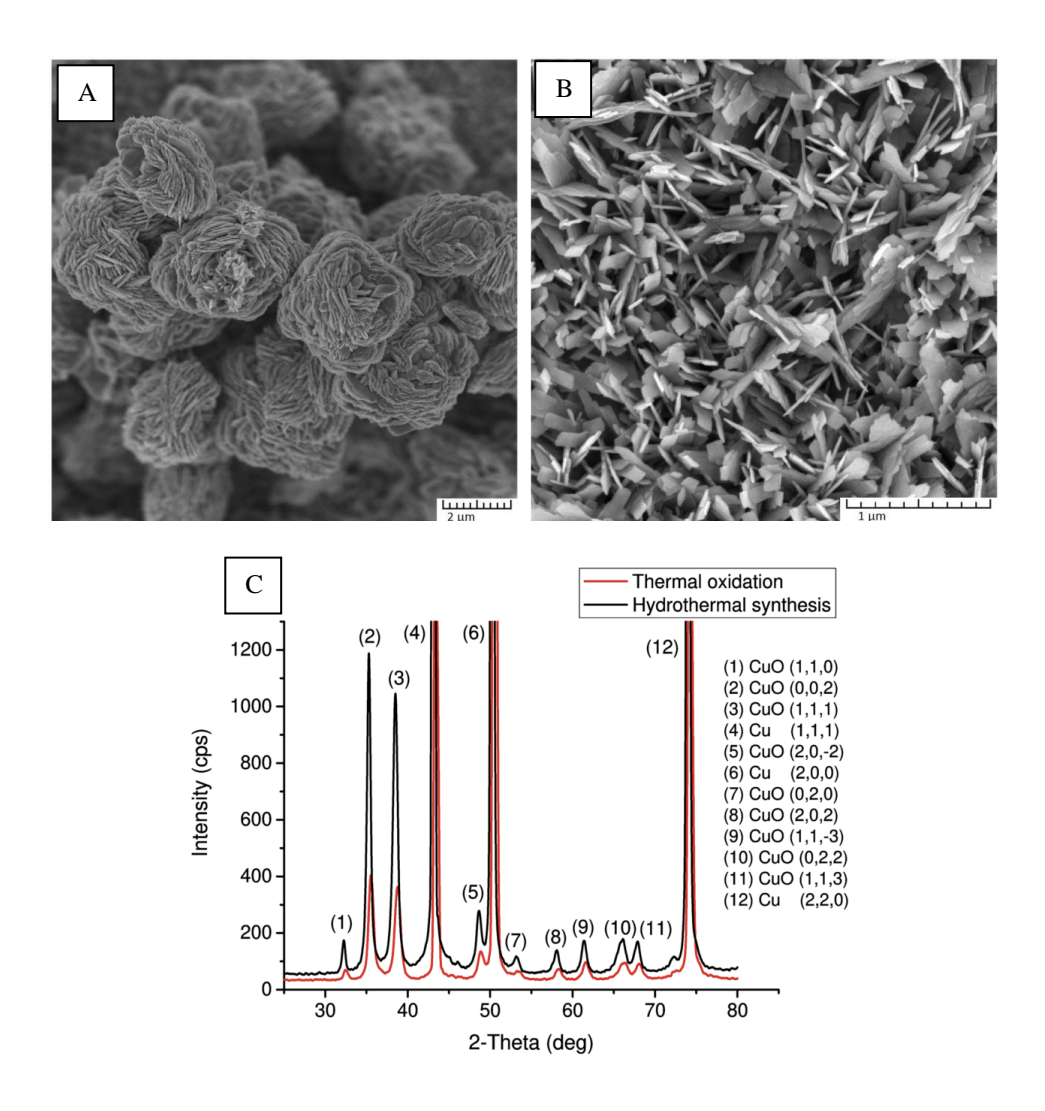


Figure 13. The synthesized CuO nanostructures. A) Nanopetals arranged in flower-like formations; B) Uniform nanopetalpayer inbetween flower-like formations; C)XRD pattern of synthesizedCuO film. [3]

The hydrothermally synthesized CuO nanostructures were compared to those obtained via thermal oxidation. The results showed that the hydrothermal method produced more uniform and porous nanostructures with a larger surface area, leading to superior electrochemical performance in terms of sensitivity and selectivity for H₂O₂ detection.

3.3. Synthesis and Morphological Characterization of Cobalt Oxide (Co₃O₄) Nanostructures

Cobalt oxide (Co₃O₄) nanostructures were synthesized using the hydrothermal method on iron wire substrates [4]. The synthesis process was carefully controlled to produce nanostructures with desired morphologies and functionalities. Two types of anions—chloride and acetate—were used as precursors to study their influence on the morphology of the resulting nanostructures.

3.3.1. Chloride Anion-Assisted Synthesis

The synthesis began with iron wire (99.9% purity, 2 mm thickness) as the base substrate. The wire was first treated with fine sandpaper and immersed in 0.1 M HCl to increase the surface roughness and improve the adhesion of the nanostructures. An equimolar aqueous solution of 0.1 M CoCl₂·6H₂O and 0.1 M hexamethylenetetramine (CH₄N₂O) was prepared in 80 mL of distilled water. The solution had a reddishviolet color and was stirred until the solid reagents dissolved completely.

The formation of Co₃O₄ nanostructures involved the following key chemical reactions [4]:

$$CoCl_2 \rightarrow Co^{2+} + 2Cl^- \tag{13}$$

$$CO(NH_2)_2 + 2 H_2O \rightarrow 2 NH_3 + CO_2 \uparrow$$
 (14)

$$NH_3 + H_2O \rightarrow NH_4^+ + OH^-$$
 (15)

$$Co^{2+} + 2OH^{-} \rightarrow Co(OH)_{2}$$
 (16)

$$3 Co(OH)_2 \rightarrow Co_3O_4 + H_2O + H_2 \uparrow$$
 (17)

The pretreated iron wire was immersed in the growth solution and placed in a preheated oven. The hydrothermal growth occurred for 5 hours at 95°C, resulting in the formation of a dull pink Co(OH)₂ coating on the wire. The growth process was followed by thermal decomposition at 450°C for 1 hour to convert Co(OH)₂ into black, homogeneous Co₃O₄ nanostructures.

3.3.2. Acetate Anion-Assisted Synthesis

The synthesis was repeated under the same conditions as the chloride precursor, but 0.1 M (CH₃COO)₂Co·4H₂O was used instead of CoCl₂·6H₂O [4].

The presence of acetate anions significantly altered the morphology of the Co₃O₄ nanostructures. Instead of forming long nanofibers as in the chloride-assisted case, the acetate precursor led to the formation of thin, petal-like nanostructures assembled into honeycomb-like agglomerates. The honeycombs formed using the acetate anion were smaller and less uniform compared to those formed with the chloride precursor.

Acetate ions acted as capping agents during the growth of the nanostructures. These ions selectively attached to specific crystallographic planes, thereby influencing the growth direction and morphology. The blocking of several crystallographic planes by acetate ions resulted in the formation of 2D-like nanostructures with reduced crystallinity [4].

The synthesized Co₃O₄ nanostructures were characterized using Scanning Electron Microscopy (SEM) and X-ray Diffraction (XRD) to study their surface morphology and crystalline structure.

3.3.3. The comparison of Chloride and Acetate anoin-assisted synthesized nanostructures

SEM images of Chloride Anion-Assisted Co₃O₄ revealed the formation of long, uniform nanofibers assembled into honeycomb-like structures. The nanofibers were densely packed and exhibited excellent adhesion to the iron substrate. The nanofibers were observed to be several micrometers in length and exhibited a high degree of uniformity in size and shape.

SEM images of Acetate Anion-Assisted Co₃O₄ showed petal-like nanostructures assembled into honeycomb-like agglomerates (Figure 14). These structures were significantly smaller and less uniform compared to the nanofiber-based morphology. The petal-like nanostructures exhibited poor adhesion and were prone to aggregation, resulting in a reduction in the active surface area.

XRD patterns confirmed the formation of pure Co₃O₄ without any extraneous phase inclusions. The diffraction peaks corresponded to the crystallographic planes of Co₃O₄, indicating its high crystallinity. The dominant orientation was perpendicular to the (311) planes.

The intensity of the diffraction peaks was higher for the chloride precursor samples, suggesting a higher degree of crystallinity compared to the acetate-assisted samples (Figure 15). The lower peak intensity observed in the acetate-assisted samples was attributed to their amorphous nature and the blocking of active crystallographic planes by acetate ions.

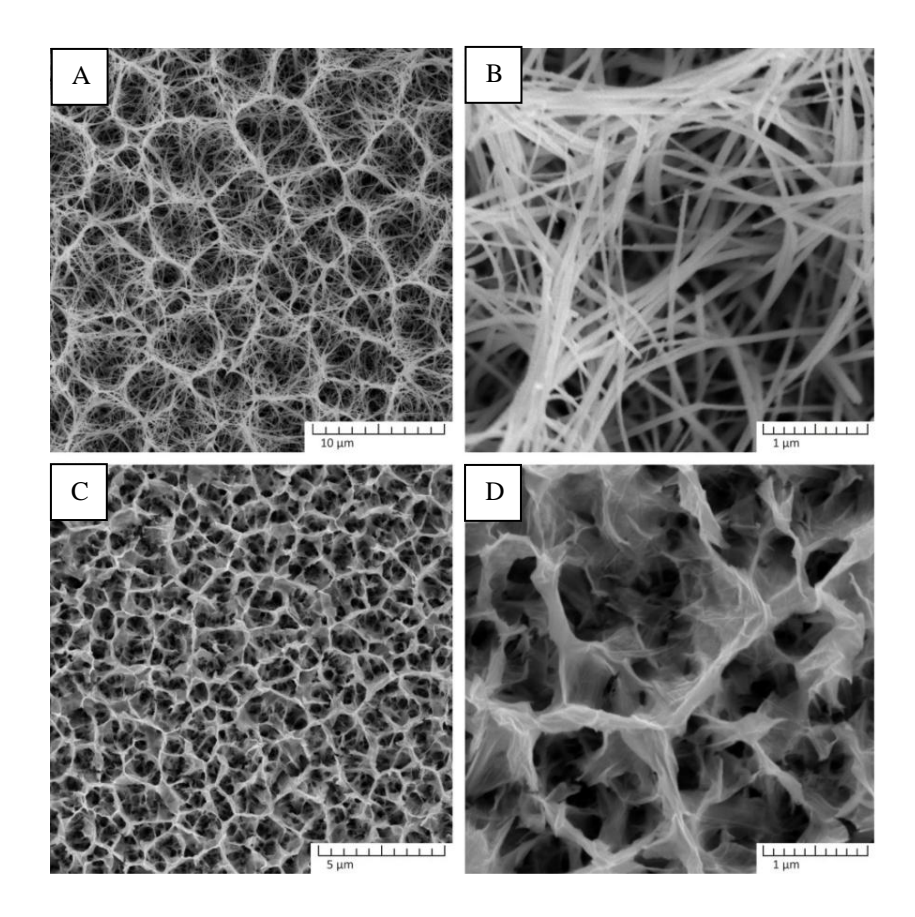


Figure 14. The study of the anion efect on the morphology of the Co₃O₄ nanostructures. A, B) Co₃O₄ nanostructures obtained from the precursor of cobalt chloride and urea, C, D) Co₃O₄ nanostructures obtained from the precursor of cobalt acetate and urea [4].

EDS microanalysis confirmed the high chemical purity of the synthesized Co₃O₄ samples. The composition consisted predominantly of cobalt (47.22 at.%) and oxygen (52.78 at.%) [4]. The absence of impurities confirmed the successful synthesis of pure Co₃O₄ nanostructures, suitable for electrochemical applications.

The honeycomb-like nanofiber morphology obtained with the chloride precursor was found to be highly suitable for electrochemical sensing applications. The fibrous structure provided a large active surface area, good adhesion, and enhanced electron charge transfer, which are critical for efficient H₂O₂ detection.

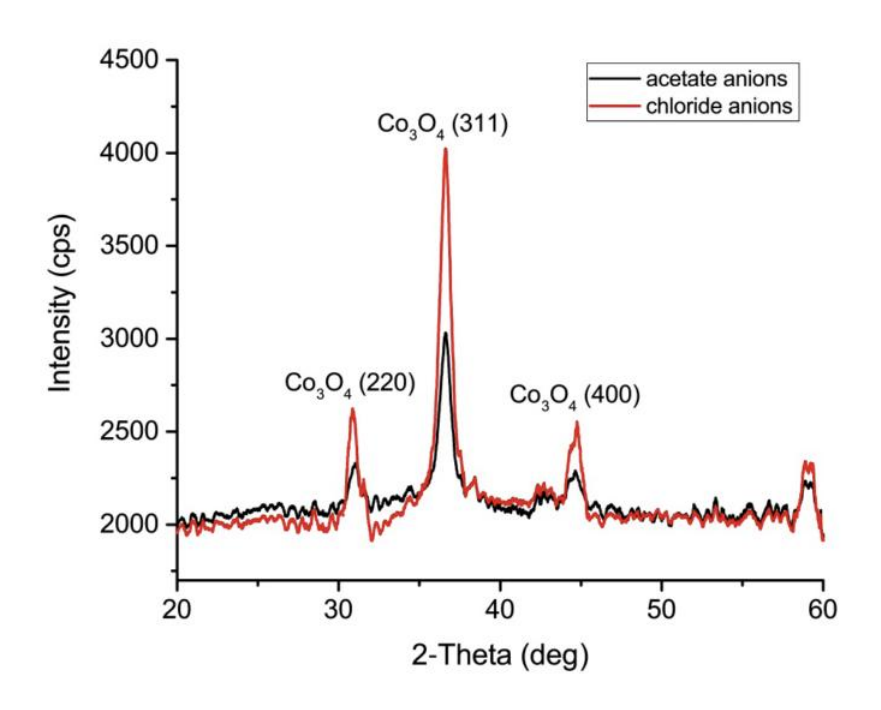


Figure 15. XRD pattern of synthesized Co₃O₄ nanostructures [4].

In conclusion, the synthesis and morphological characterization of Co₃O₄ nanostructures reveal the significant influence of the precursor anion on the resulting morphology. The chloride precursor yielded highly sensitive and stable nanofiber structures ideal for electrochemical sensor applications, whereas the acetate precursor produced nanostructures with reduced performance. These findings underscore the importance of precursor selection in tailoring the morphology and functionality of nanostructures for specific applications.

3.4. Synthesis and Morphological Characterization of Nickel Oxide Nanostructures

In this study, nickel oxide (NiO) nanostructures were synthesized using a hydrothermal method, offering a cost-effective and controllable approach for producing nanostructures with well-defined morphologies [5]. The synthesis was carried out using a 0.1 M equimolar mixture of nickel nitrate hexahydrate (Ni(NO₃)₂·6H₂O) and hexamethylenetetramine (C₆H₁₂N₄) dissolved in 75 mL of distilled water. The iron wire, serving as the substrate for nanostructure growth, was initially cut into 6 cm pieces, cleaned with sandpaper, and treated with a weak hydrochloric acid solution for 2 minutes. This pretreatment modified the wire's microstructure, increased surface roughness, and enhanced adhesion for the subsequent deposition of nanostructures.

The hydrothermal reaction involved the dissolution of the nickel nitrate and hexamethylenetetramine mixture under continuous stirring. The resulting greenish colloidal solution was transferred into a borosilicate glass container, and the iron wires were immersed. The setup was then placed in an oven preheated to 95 °C for 5 hours. During this time, a light green Ni(OH)₂ precipitate formed due to the reaction between Ni²⁺ and OH⁻ ions. The reaction can be described using the following steps [5]:

$$C_6H_{12}N_4 + 6H_2O \rightarrow 4NH_3 + 6HCHO$$
 (18)

$$NH_3 + H_2O \rightarrow NH_4^+ + OH^-$$
 (19)

$$Ni^{2+} + 2OH^- \to Ni(OH)_2$$
 (20)

After hydrothermal treatment, the wires were washed several times with distilled water and subsequently annealed at 450 °C for 3 hours. This thermal treatment decomposed Ni(OH)₂ into NiO [5]:

$$Ni(OH)_2 \rightarrow NiO + H_2O$$
 (21)

This multi-step process ensured the formation of a uniform and stable NiO nanostructured coating on the iron wires.

The morphological features of the synthesized NiO nanostructures were analyzed using Scanning Electron Microscopy (SEM). The SEM images revealed a nanostructured coating consisting of a uniform and dense layer of nanowalls, forming a porous labyrinthine structure. At higher magnifications, the surface was observed to be covered with nanowalls that extended in multiple directions, creating a complex three-dimensional architecture.

Additionally, spherical flower-like formations were observed atop the nanowall layer [5]. These formations are composed of nanopetals and have a micrometer-scale structure. The presence of these spherical agglomerates suggests the formation of second-generation nanostructures, where nucleation and growth occur within the working solution volume. The influence of gravity was evident, as these structures were deposited onto the first-generation layer of nanowalls, where they adhered and further developed.

To investigate the crystal structure of the synthesized NiO nanostructures, X-ray diffraction (XRD) was employed. The resulting XRD pattern revealed the crystalline phase of NiO. However, a prominent amorphous background was also observed, likely attributed to the thinness of the nanostructures. Several well-defined peaks with relatively high intensity were identified, confirming the crystalline nature of NiO.

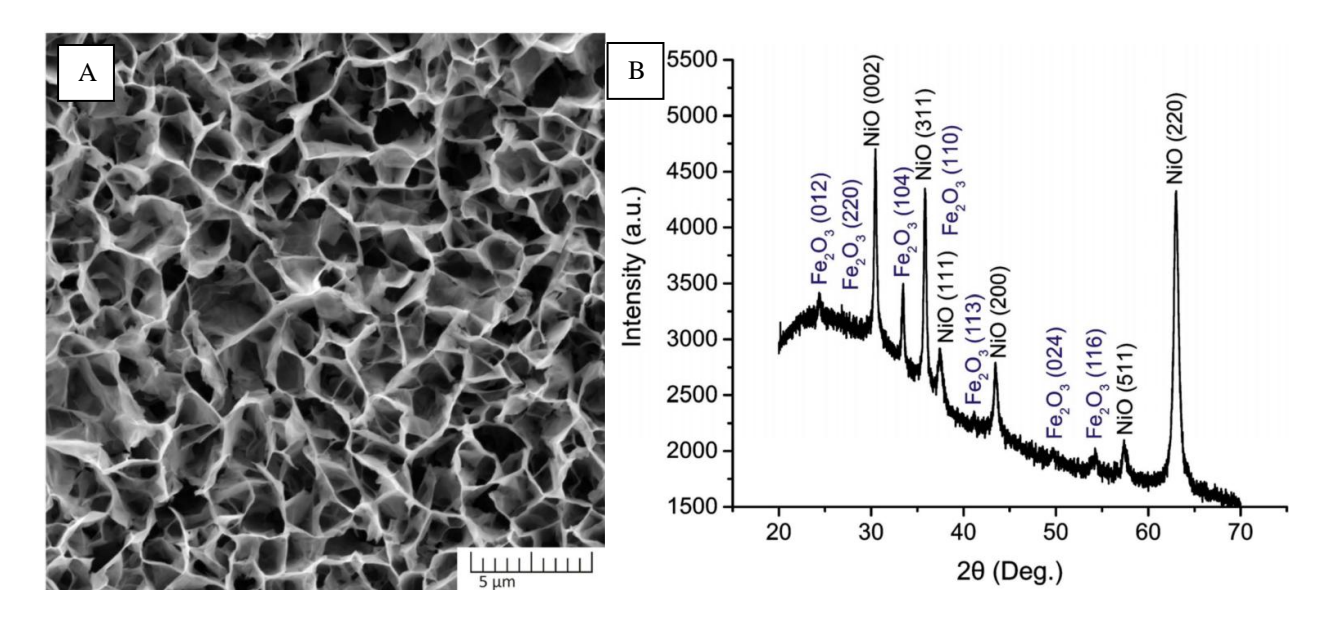


Figure 16. A) The synthesized NiO nanostructures; B) XRD spectrum of synthesized NiO coating on Fe substrate [5].

In addition to NiO, small inclusions of the Fe₂O₃ crystalline phase were observed. These inclusions can be attributed to the absence of nanostructure growth at the locations where the wire was attached in the synthesis beaker. The annealing process applied to the iron wire itself also contributed to the presence of these Fe₂O₃ inclusions.

The XRD data provided valuable insights into the crystallinity and structural characteristics of the synthesized NiO nanostructures. The presence of NiOOH species and the formation of oxyhydroxide species (NiOOH) at relatively high applied potentials were critical for the electrocatalytic efficiency of the NiO nanostructures in hydrogen peroxide (H₂O₂) detection.

The hydrothermal synthesis method successfully produced NiO nanostructures with a unique combination of wall-shaped nanowalls and spherical agglomerates. The SEM and XRD analyses confirmed the formation of a uniform and dense NiO coating with a porous and labyrinthine structure, which is conducive to enhancing the surface area and electrochemical performance of the sensor. The presence of NiOOH species and the observed crystalline NiO phase were essential for the catalytic activity of the sensor, particularly in the context of H₂O₂ detection in plant samples.

Overall, the morphological and structural characteristics of the synthesized NiO nanostructures laid a solid foundation for their application in the development of a high-performance electrochemical sensor for oxidative stress biomarker detection in rye seedlings under salt stress conditions.

4. Cell Designs Utilized in Electrochemical Sensing Studies

In the development and testing of various electrochemical sensors for the detection of analytes such as hydrogen peroxide released due to stress in plant samples and glyphosate, several distinct electrochemical cell designs were employed. These designs were tailored to accommodate the specific requirements of the sensing application, including the type of electrode material, the nature of the analyte, and the need for reproducibility and ease of sample handling.

4.1. Custom-Built Electrochemical Cell with Nanostructured Electrodes

A custom-built electrochemical cell was utilized in multiple studies [5] [6] [99] involving nanostructured electrodes for the detection of hydrogen peroxide and other analytes. The cell was constructed using a glass beaker housed within a temperature-regulated water bath and integrated with a magnetic stirrer to ensure uniform mixing and consistent temperature (typically 25 °C).

The working electrode (WE) was a nanostructure coated wire electrode, fabricated through a two-step process involving hydrothermal synthesis and thermal decomposition, as detailed in the synthesis section (Page 32). The counter electrode (CE) was made of carbon, and the reference electrode (RE) was a Ag/AgCl electrode.

To ensure consistent positioning and reproducibility across measurements, the cell featured a custom 3D-printed ABS (acrylonitrile butadiene styrene) lid with a fixed height, designed to hold the working electrode in place. A heat-shrink polymer was used to seal the wire electrode, exposing only the sensing area (typically 1–2 cm) to the analyte solution.

The lid also included a central hole for the addition of the analyte via micropipette and the integration of additional equipment, such as a thermometer or pH meter during measurements. All electrochemical measurements were conducted using the Zahner Zennium electrochemical workstation, allowing precise control over parameters such as voltage, scan rate, and measurement duration.

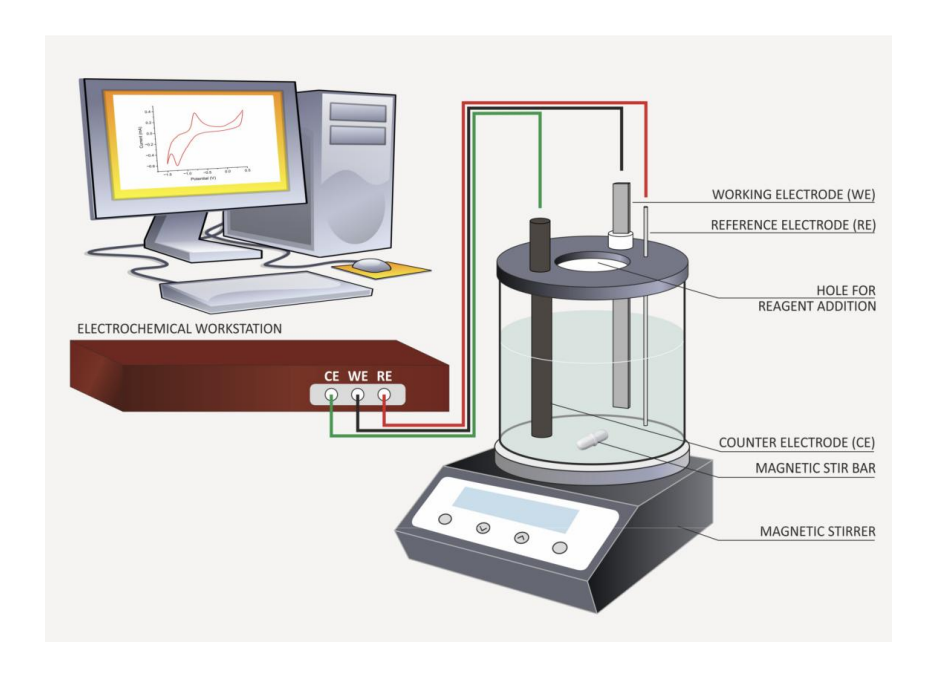


Figure 17. Schematic representation of utilized electrochemical measurement cell [99].

This design was particularly suitable for studying plant-based analytes such as barley and rye under stress conditions, where the electrochemical response to H_2O_2 could be monitored with high sensitivity and selectivity. Additionally, the design supported chronopotentiometric, cyclic voltammetry (CV), and chronoamperometric measurements. The cell design facilitated both calibration and interference testing, and the use of 70 mL of analyte per measurement allowed for sufficient statistical analysis.

4.2. Mass-Produced PCB Chip Electrochemical Cell

In other studies [100] [8], a mass-produced PCB (printed circuit board) chip was used as the electrochemical cell, eliminating the need for a traditional beaker-based setup. The PCB chip featured eight gold-coated copper electrodes arranged in a compact configuration, fabricated using the ENIG (Electroless Nickel Immersion Gold) process on an FR-4 glass-reinforced epoxy laminate.

The PCB chip was designed to fit into a quick-change connector within the electrochemical cell, ensuring easy and consistent electrode alignment. Each electrode had an individual copper track and a $150 \times 125 \,\mu m$ exposed gold surface. The chip supported three-electrode configurations, with each electrode potentially serving as a working, counter, or reference electrode. The tracks were covered with a protective dielectric polymer, and the chip was designed to allow flexible electrode configurations.

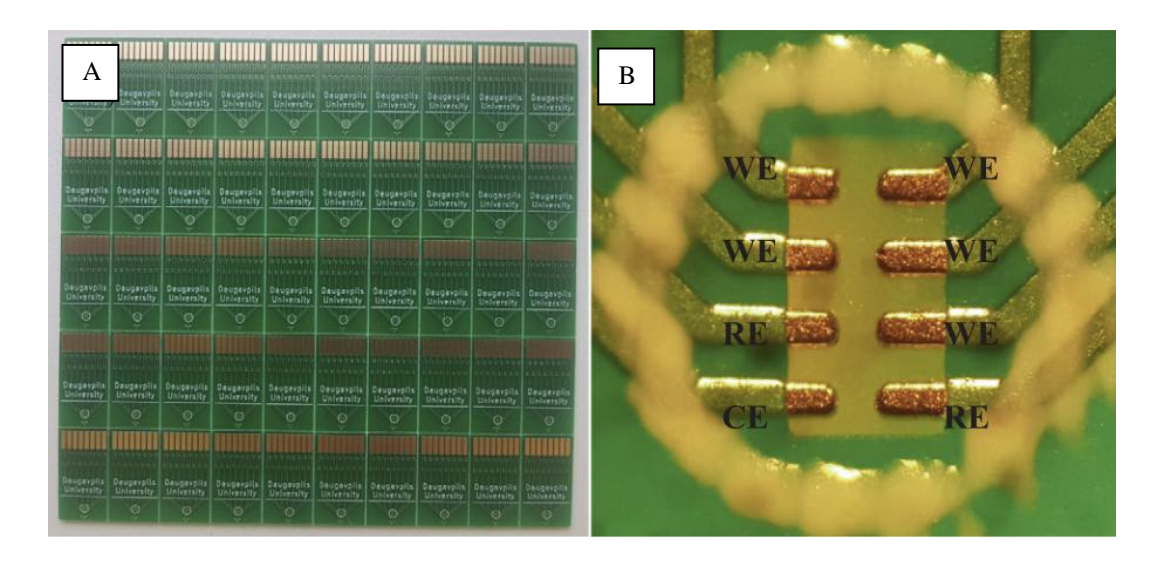


Figure 18. a) Mass-produced PCB chips with Au-coated electrodes. b) Chip electrode configuration. WE=working electrode, CE=counter electrode, and RE=reference electrode. The diameter of the white ring is 1 mm [8].

Electrochemical measurements were performed using the Zahner Zennium workstation in square wave voltammetry (SWV) mode. This chip-based cell was particularly suitable for high-throughput screening, miniaturized sensors, and portable device development, and its modular and scalable nature made it ideal for integration into lab-on-chip systems.

This setup was used for electrochemical detection in various sample matrices and allowed for the replacement of electrodes before each measurement, ensuring sample-specific calibration and cross-contamination-free operation. The integration of a temperature-regulated water bath and magnetic stirrer was also maintained, depending on the specific requirements of the measurement protocol.

4.3. Miniaturized Droplet-Based Electrochemical Cell for Surface Morphology Studies

In a study focused on the impact of surface morphology on wetting dynamics, a miniaturized droplet-based electrochemical cell was used [9]. This design was particularly innovative for in situ electrochemical impedance spectroscopy (EIS) measurements, where nanostructure-coated Cr electrodes served as both the counter and working electrodes.

A 250 μ L droplet of the target liquid was placed on the cell, and phase shift dependence on frequency was measured immediately and repeated every minute for 10 minutes. The setup allowed for the investigation of dynamic wetting behavior in response to surface structure, and an average of eight measurements was taken at different spots on the sample.

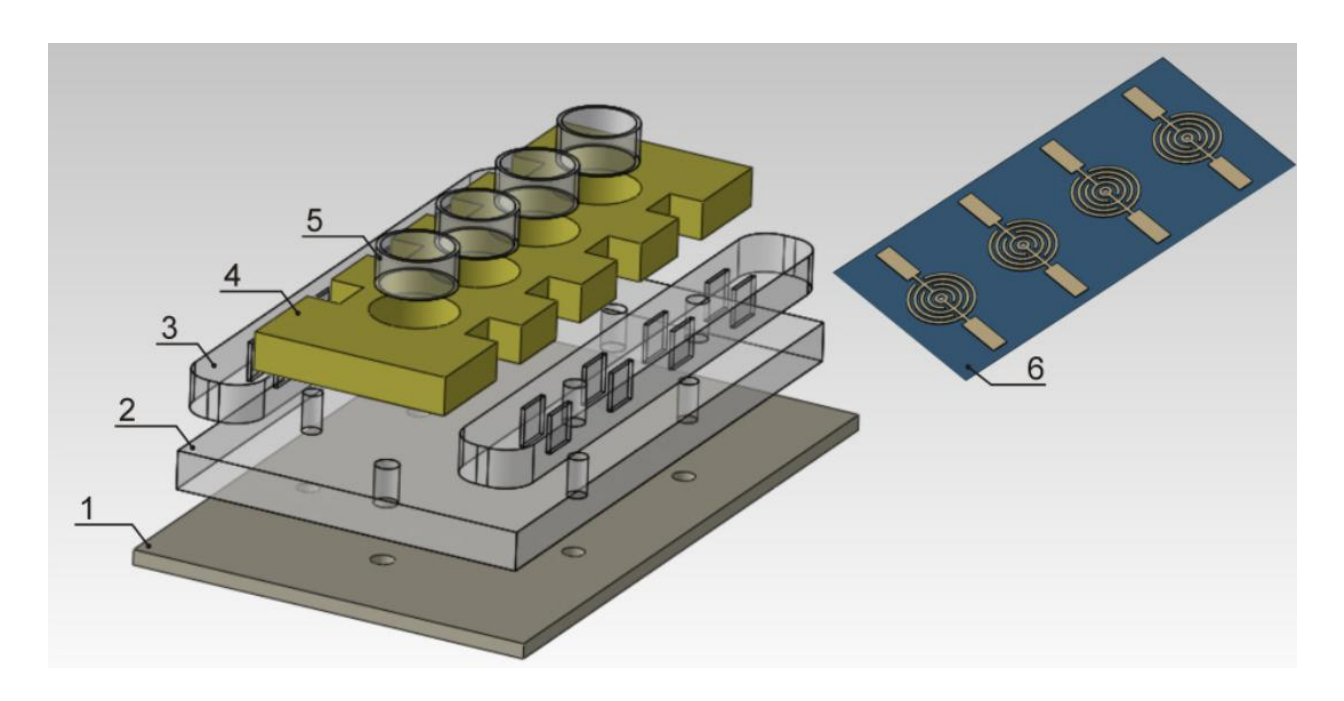


Figure 19. Structure of the electrical measurement cell (left) and electrodes (right). The measurement cell consists of the following parts: a corps (1), an interlayer (2) with push-in contacts (3), a sealing rubber mask (4) with replaceable plastic cylinders (5). Sample (6) consists of four electrodes, which allow four independent analyte measurements to be performed consistently [9].

This design was particularly suited for surface science and material studies, where the morphology of nanostructured surfaces directly influenced electrochemical and interfacial properties.

Cell	Electrode		Measurement		
Туре	Configuration	Electrolyte	Technique	Key Features	Use Case
Fe/Co ₃ O ₄ Wire	WE: Fe/Co ₃ O ₄ , CE: Carbon, RE: Ag/AgCl	0.1 M NaOH (pH 13)	CV, Chronoamperometry	ABS lid, magnetic stirrer, temperature-controlled	H ₂ O ₂ in barley under salt stress [6]
Fe/NiO Wire	WE: Fe/NiO, CE: Carbon, RE: Ag/AgCl	Alkaline Buffer	CV	Pre-treatment required, cyclometric scanning	H ₂ O ₂ in rye under salt stress [5]
PCB Chip	8 Au-coated Cu electrodes	Varies	SWV	Mass-produced, modular, flexible configuration	High-throughput screening [8]
PCB Electrode	WE/CE on PCB, RE separate	Varies	CV, EIS	Replaceable, standardized, quick- change design	General-purpose electrochemical analysis [100]
Droplet- Based	ZnO-coated Cr electrodes	Various liquids	EIS	Miniaturized, 250 μL droplet, dynamic measurement	Surface morphology and wetting dynamics [9]

Table 1. List of electrochemical cells and electrode modifications used in this study.

These diverse electrochemical cell designs reflect the adaptability and versatility required in the development and validation of electrochemical sensors for different analytes and sample types. Each design was selected based on the specific analytical goals, including selectivity, sensitivity, reproducibility, and compatibility with complex matrices such as plant extracts.

5. Glyphosate Detection Using Electrochemical Sensors

Glyphosate, the most widely used herbicide globally, has raised significant concerns due to its potential health risks, including respiratory malfunction, altered consciousness, neurotoxic effects, increased cancer risk, and even death. Despite its widespread application in agriculture, detecting glyphosate in plant samples and environmental matrices remains a challenge. Conventional detection techniques are often expensive, time-consuming, and require complex instrumentation and extensive sample preparation. Moreover, many modern analytical laboratories fail to detect glyphosate at low concentrations in food products, underscoring the urgent need for a robust, cost-effective, and portable detection method.

This study presents a novel approach to glyphosate detection using electrochemical sensors based on mass-produced printed circuit board (PCB) electrodes. The sensors rely on the principle of indirect glyphosate detection, exploiting its ability to form water-soluble complexes with copper ions (Cu²⁺). This interaction reduces the electrochemical activity of Cu²⁺, which can be monitored using square wave voltammetry (SWV) [8]. The method eliminates the need for sensor surface modification or enzyme-based recognition systems, simplifying the detection process.

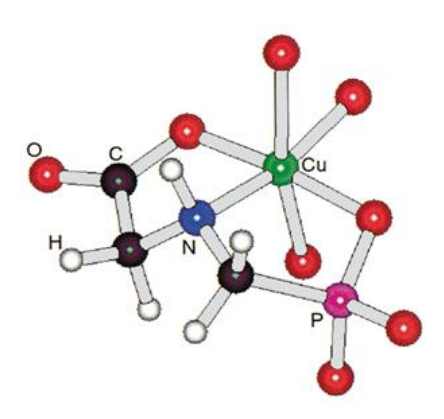


Figure 20. Glyphosate-copper complex [101].

The application of these sensors is particularly relevant in agricultural and environmental monitoring, where on-site, real-time glyphosate detection is crucial. The proposed method is portable, scalable, and compatible with automation, making it ideal for integration into field-deployable systems. Furthermore, the sensor's ability to distinguish between glyphosate-contaminated and uncontaminated plant juices, as demonstrated through both electrochemical and molecular analyses, highlights its potential for monitoring glyphosate uptake in crops.

5.1. Experimental Procedures

The experimental procedures for glyphosate detection were designed to assess both the performance of the electrochemical sensor and its practical applicability in real-world conditions. The study was conducted in multiple phases [8]:

Synthetic Samples and Calibration

To evaluate the sensor's sensitivity and reproducibility, synthetic solutions of glyphosate were prepared by dissolving the herbicide in 15 mmol/L Cu(NO₃)₂ solutions. A series of calibration standards were prepared, covering a concentration range of 0 to 1.5 mmol/L. These solutions were used to determine the sensor response under controlled conditions.

Plant Sample Preparation

To test the applicability of the sensor in real-world scenarios, 7-day-old rye plant seedlings were treated with a 1:10 dilution of a commercial glyphosate-based herbicide (360 g/L as isopropylamine salt) and allowed to grow for five additional days. Plant juice was extracted by crushing the plant tissue and filtering the suspension through a coarse mesh. The filtered juice was then mixed with highly concentrated Cu(NO₃)₂ to achieve a final concentration of 15 mmol/L Cu(NO₃)₂ in the solution. Control plant samples (untreated with glyphosate) were processed in parallel for comparison.

Electrochemical Sensor Preparation and Operation

Prior to use, the mass-produced PCB chips (Figure 18) were cleaned with ethanol and purged with a nitrogen jet to remove any manufacturing residues or contaminants. Each chip was fabricated using electroless nickel/immersion gold (ENIG) plating on an FR-4 glass-reinforced epoxy laminate, resulting in a durable and chemically inert surface. The working surface of each electrode was defined by a 150 \times 125 μm gold-coated area, and each chip contained eight individual electrodes connected by copper tracks.

For electrochemical measurements, 10 μ L of solution (either synthetic or plant juice supernatant) was placed on the working area of the chip. In the case of plant juice samples, a 30-minute incubation period was allowed before centrifugation to remove solid residues. 10 μ L of the resulting supernatant was then applied for SWV analysis.

The electrochemical measurements were conducted using a Zennium Electrochemical Workstation, with the chip configured as a three-electrode system: working electrode (WE), counter electrode (CE), and reference electrode (RE), all of which were integrated on the chip. Each sample was tested using a new chip from the same production batch to ensure consistency and minimize variability.

5.2. Data Analysis and Automation Potential

The voltammetric data collected from the workstation was used to generate square wave voltammetry (SWV) curves, allowing the quantification of the sensor response to varying glyphosate concentrations. The main peak amplitude, typically observed between 50–300 mV, corresponded to the reduction of Cu²⁺ ions and showed a linear decrease in amplitude with increasing glyphosate concentrations up to 1.5 mmol/L, after which the sensor became saturated [8].

The SWV peak amplitude was normalized to the maximum current observed in the control (0 mmol/L glyphosate) solution. This normalization enabled clear differentiation between glyphosate-contaminated and uncontaminated samples, with glyphosate-treated plant juice showing 10% decrease in main peak amplitude when compared to control samples.

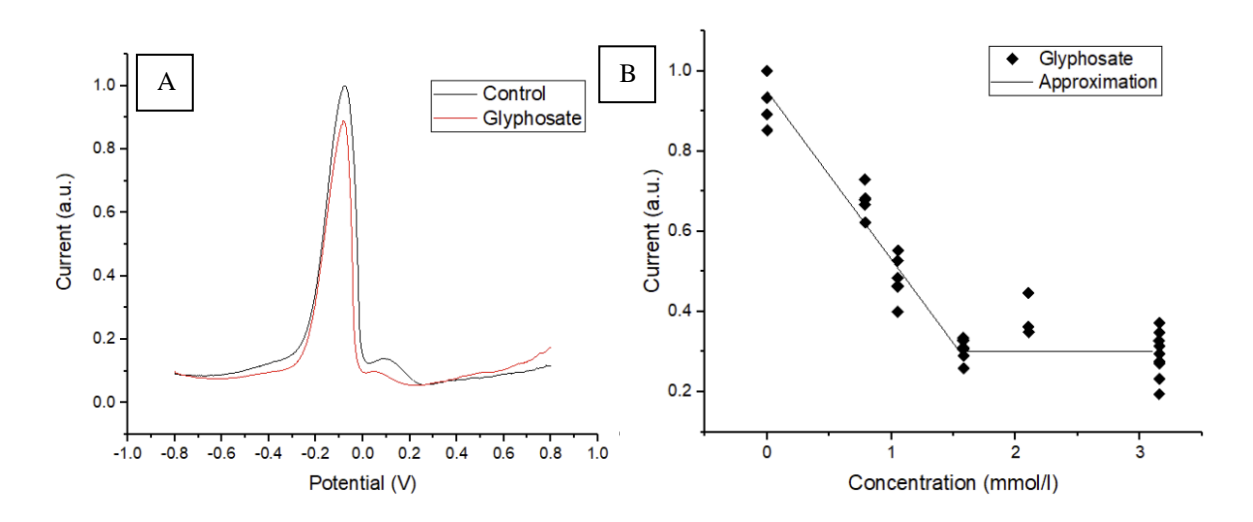


Figure 21. A) Averaged SWV curve for rye samples. B) The main-peak maximum from SWV versus glyphosate concentration. [8]

Based on the consistency and reproducibility of the SWV signals across multiple chips and concentrations, automated detection protocols were developed. These algorithms utilized threshold-based classification, enabling the system to classify samples as either contaminated or uncontaminated based on peak amplitude. This high degree of reproducibility supports the integration of the sensor into automated field detection systems.

5.3. Molecular Validation of Glyphosate Effects

To further validate the presence of glyphosate in treated plants and its potential genotoxic effects, genomic DNA was extracted from 60 plant samples: 30 from glyphosate-treated rye seedlings and 30 from control samples. DNA was isolated using a modified DNeasy Plant Mini Kit protocol, and RAPD (Random Amplified Polymorphic DNA) analysis was performed using five selected primers (OPA-02, OPA-07, OPA-11, OPD-18, and OPN-15) [8].

PCR products were separated using capillary electrophoresis (QIAxcel system), and the RAPD profiles were analyzed for the presence or absence of DNA bands. The results showed significant differences in the

DNA banding patterns between the control and glyphosate-treated groups. Specifically, 15 new bands appeared, and 12 bands disappeared in the glyphosate-treated samples compared to the controls [8]. These changes are indicative of genotoxic alterations, including point mutations, deletions, and strand breaks.

The RAPD findings corroborate the electrochemical results and confirm that glyphosate exposure leads to detectable DNA changes in plants, reinforcing the validity of the sensor in identifying glyphosate-contaminated plant material.

Discussion and Implications

The use of mass-produced PCB-based sensors for glyphosate detection demonstrates a highly effective, low-cost, and scalable approach for monitoring herbicide use in agricultural settings. The indirect detection mechanism based on Cu²⁺ ion complexation with glyphosate eliminates the need for sensor modification or expensive reagents. The SWV-based electrochemical method is sensitive, specific, and suitable for real-time, on-site detection, even in small-volume plant juice samples.

The molecular validation using RAPD analysis further supports the electrochemical findings, confirming that glyphosate uptake by plants leads to genetic alterations, and thus, the sensor can serve as a biomonitoring tool in addition to a detection system.

This method provides a comprehensive framework for glyphosate detection and monitoring in agricultural and environmental contexts, with clear implications for improving food safety, regulatory compliance, and sustainable herbicide use.

6. Electrochemical Sensors for Hydrogen Peroxide Detection Using Metal Oxides

Hydrogen peroxide (H₂O₂) is a vital molecule in biological, environmental, and industrial systems, often serving as an indicator of oxidative stress, a marker for disease detection, and a reagent for various applications. The development of electrochemical sensors for H₂O₂ detection has gained significant attention due to their advantages of high sensitivity, rapid response, and feasibility for integration into portable analytical devices. Among the materials investigated, metal oxides have emerged as promising candidates for sensor fabrication due to their unique electrochemical properties, structural tunability, and catalytic activity.

This chapter explores the electrochemical detection of H₂O₂ using various metal oxides, including cobalt oxide (Co₃O₄), copper oxide (CuO), and zinc oxide (ZnO). The approach adopted involves a systematic experimental workflow: first, cyclic voltammetry (CV) is used to identify characteristic redox peaks that are indicative of the electrochemical activity of the sensor; second, amperometric measurements quantify the sensitivity of the sensor to H₂O₂; and third, interference analysis assesses the selectivity of the sensor in the presence of common interferents.

6.1. Cyclic Voltammetry for Electrochemical Hydrogen Peroxide Detection

Cyclic voltammetry is the first step in evaluating the electrochemical behavior of the metal oxide-modified electrodes. This technique helps identify the characteristic oxidation and reduction peaks that arise from the interaction of H₂O₂ with the metal oxide surface. By varying the scan rates and concentrations of H₂O₂, the redox properties of the sensor can be comprehensively understood, which is crucial for subsequent amperometric and interference studies.

6.1.1. Cobalt Oxide (Co₃O₄) Electrodes

The Co₃O₄ electrodes, prepared via hydrothermal synthesis (page 43), demonstrated excellent electrochemical activity toward H₂O₂. The CV measurements were conducted in a 0.1 M NaOH solution containing H₂O₂ concentrations ranging from 0.2 mM to 2 mM. The CV results revealed two distinct pairs of redox peaks: anodic peaks at approximately -0.8 V (peak I) and -0.15 V (peak II), and cathodic peaks at around -1.23 V (peak III) and 0.35 V (peak IV).

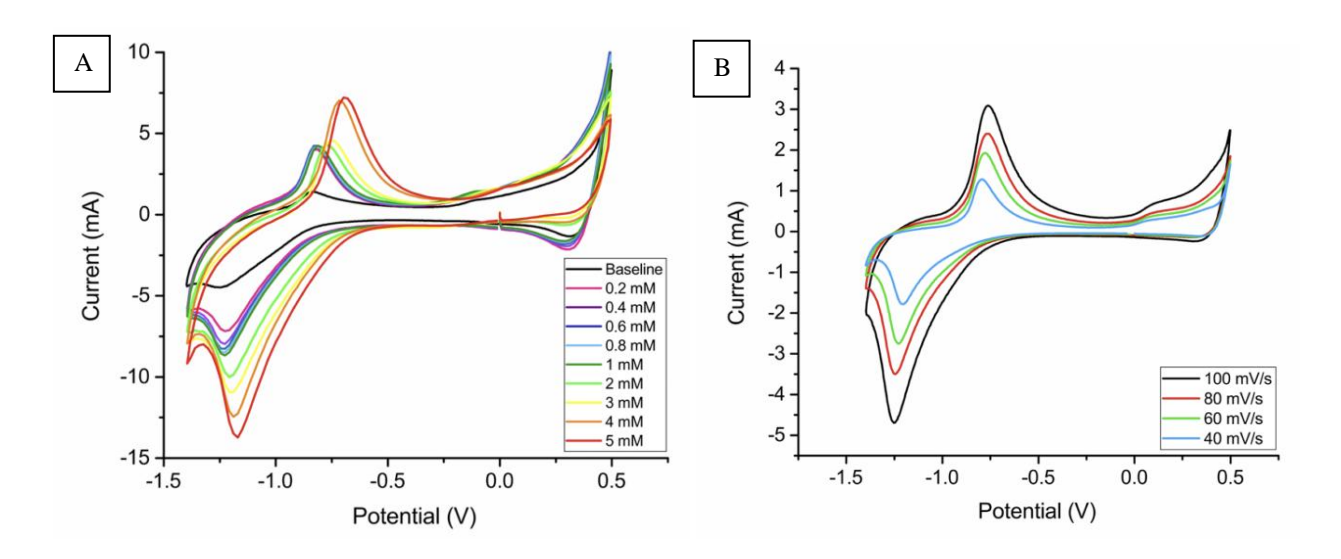


Figure 22. CV voltammograms of a nanostructured Co_3O_4 film derived from chloride anions. A) The dependence of voltammogram on H_2O_2 concentration (scan rate = 100 mV/s), b) The dependence of voltammogram on scan rate.

Measurements were performed in 0.1 M NaOH buffer solution (pH = 13) [4].

In the absence of H₂O₂, these redox peaks were attributed to the reversible transitions between Co₃O₄, CoOOH, and CoO₂. The first redox pair (I/III) was associated with the transition between Co₃O₄ and CoOOH, while the second redox pair (II/IV) corresponded to the further conversion between CoOOH and CoO₂. These reactions can be described as follows [4] [6]:

$$C_{03}O_4 + OH^- + H_2O \rightarrow 3CoOOH + e^-$$
 (22)

$$CoOOH + OH^{-} \rightarrow CoO_2 + H_2O + e^{-}$$
(23)

Upon the addition of H₂O₂, the shape of the CV curve significantly changed. Notably, the oxidation peak (I) and reduction peak (III) exhibited a marked increase in peak current. The peak (III) current value showed a linear relationship with the concentration of H₂O₂ added. Additionally, peak (I) demonstrated a less pronounced increase, and its position along the x-axis shifted with increasing H₂O₂ concentration, reaching -0.7 V at higher concentrations. Peaks (II) and (IV) showed minimal changes over the entire concentration range.

The electrocatalytic reaction of H₂O₂ on the Co₃O₄ electrode can be described by the following reaction [4] [6]:

$$6C_0OOH + H_2O_2 \rightarrow 2C_{03}O_4 + O_2 + 4H_2O$$
 (24)

These findings highlight the exceptional electrochemical response of Co_3O_4 electrodes to H_2O_2 , as evidenced by the significant changes in peak currents and the linear correlation between the current and H_2O_2 concentration.

6.1.2. Copper Oxide (CuO) Electrodes

The CuO electrodes, synthesized via a one-step chemical hydrothermal oxidation method (page 40), exhibited remarkable electrochemical activity toward hydrogen peroxide (H₂O₂). The cyclic voltammetry (CV) measurements were carried out in a 0.1 M NaOH solution, with H₂O₂ concentrations ranging from 0.1 mM to 5 mM. The CV curves revealed two distinct pairs of redox peaks: anodic peaks at approximately -0.2 V (peak I) and 0.1 V (peak II), and cathodic peaks at around -0.7 V (peak III) and -0.8 V (peak IV) [3].

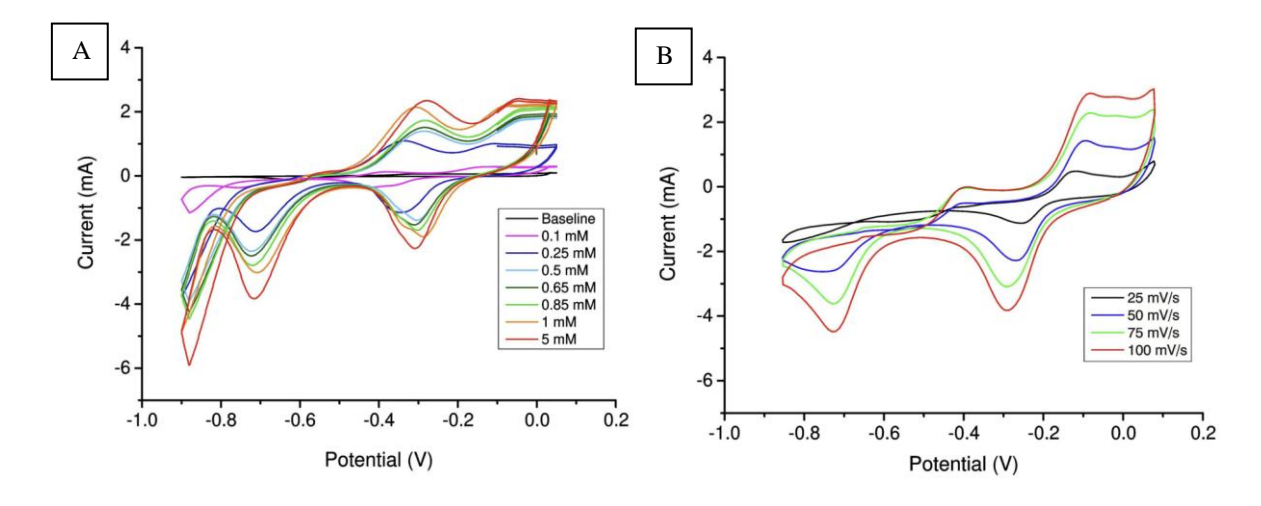


Figure 23. CV voltammograms of a nanostructured CuO film. A) The dependence of voltammogram on H_2O_2 concentration, b) The dependence of voltammogram on scan rate. Measurements were performed in 0.1 M NaOH buffer solution [3].

In the absence of H₂O₂, these redox peaks were primarily attributed to the reversible redox transitions involving copper species, such as Cu⁰/Cu⁺ and Cu⁺/Cu²⁺. The first redox pair (peak I/peak III) was associated with the transition from Cu⁰ to Cu⁺ and back, while the second redox pair (peak II/peak IV) corresponded to the transition from Cu⁺ to Cu²⁺. These transitions can be described by the following simplified reactions [3]:

$$Cu^0 \rightarrow Cu^+ + e^- \tag{25}$$

$$Cu^+ \to Cu^{2+} + e^- \tag{26}$$

Upon the introduction of H₂O₂ into the solution, the shape and magnitude of the CV peaks underwent significant changes. Notably, the oxidation peak (peak I) and the reduction peak (peak III) showed a marked increase in peak current as the concentration of H₂O₂ increased. The current at peak III demonstrated a linear correlation with the H₂O₂ concentration over the studied range, indicating a strong electrochemical response to the analyte. Peak I also exhibited an increase in current, although its position shifted with increasing H₂O₂ concentration, moving to approximately -0.1 V at higher concentrations. In contrast, peaks II and IV showed minimal change across the entire range of H₂O₂ concentrations tested, suggesting limited involvement in the electrocatalytic process.

The catalytic reaction of H₂O₂ on the CuO electrode surface can be summarized by the following reaction mechanism [3]:

$$Cu^{2+} + H_2O_2 \rightarrow Cu^+ + O_2 + H_2O$$
 (27)

$$Cu^{+} + OH^{-} \rightarrow Cu^{2+} + e^{-}$$
 (28)

These reactions indicate that the CuO surface acts as a redox mediator, cycling between Cu⁺ and Cu²⁺ states during the decomposition of H₂O₂ into oxygen and water. This mechanism not only contributes to the high electrochemical sensitivity observed but also underscores the stability and reusability of the CuO electrode under continuous operation.

The CV results highlight the high electrochemical activity of CuO electrodes toward H₂O₂, as evidenced by the significant increase in peak current values and the linear dependence of current on H₂O₂ concentration.

6.1.3. Nickel Oxide (NiO) Electrodes

The NiO electrodes, fabricated via hydrothermal synthesis of wall-shaped nanostructures on iron wire substrates (page 47), exhibited robust electrochemical activity toward hydrogen peroxide (H_2O_2) [5]. Cyclic voltammetry (CV) measurements were performed in a 0.1 M NaOH solution, with H_2O_2 concentrations varying between 100 μ M and 2 mM. The CV curves revealed two well-defined redox peaks: an anodic peak at approximately -0.4 V (peak I) and a cathodic peak at around -1.4 V (peak II). These peaks corresponded to the reversible redox transitions of nickel species, specifically the Ni(II)/Ni(III) system, involving Ni(OH)₂ and NiOOH. These redox processes can be represented by the following reactions [5]:

$$Ni(OH)_2 + OH^- \rightarrow NiOOH + H_2O + e^-$$
(30)

$$NiOOH + H_2O + e^- \rightarrow Ni(OH)_2 + OH^-$$
 (31)

In the absence of H_2O_2 , the CV responses were primarily governed by these Ni-based redox processes. However, upon the introduction of H_2O_2 into the solution, a significant electrochemical response was observed, particularly at the cathodic peak (-1.4 V), which demonstrated a linear dependence on H_2O_2 concentration. This peak, corresponding to the reduction of NiOOH to Ni(OH)₂ in the presence of H_2O_2 , became the dominant feature in the catalytic oxidation process. The anodic peak at -0.4 V also showed a noticeable increase in current, although it remained less responsive to H_2O_2 compared to the cathodic peak.

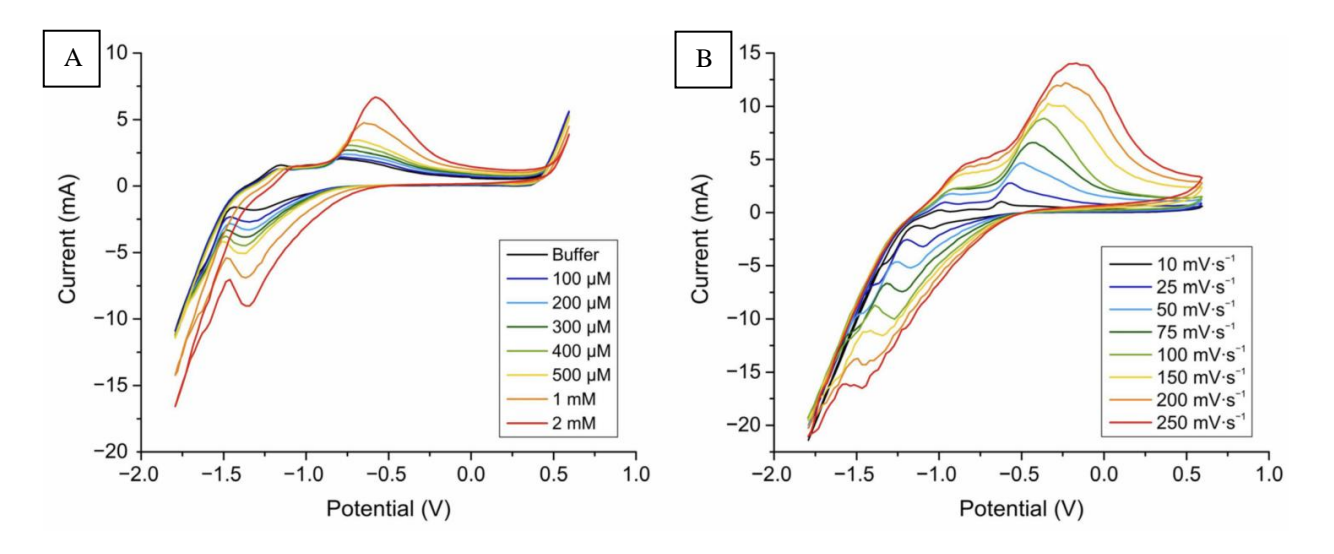


Figure 24. A) CV graph of a nanostructured NiO nanowall-based electrode obtained in a 0.1 M NaOH supporting electrolyte and in solutions containing H_2O_2 in a concentration range of 100 μ M to 2 mM. B) Dependence of the electrochemical response of the NiO electrode on the scanning speed. Scanning was performed in a 0.1 M NaOH solution containing 2 mM H_2O_2 [5].

The catalytic reaction of H₂O₂ on the NiO electrode surface is summarized by the following reaction mechanism [5]:

$$2NiOOH + H2O2 \rightarrow 2Ni(OH)2 + O2 \uparrow$$
 (32)

This mechanism indicates that the NiO surface functions as a redox mediator, cycling between Ni(II) and Ni(III) states during the decomposition of H₂O₂ into oxygen and water. The ability of NiOOH to oxidize H₂O₂ efficiently at relatively high applied potentials, especially in alkaline conditions, contributes to the sensor's high electrocatalytic efficiency.

The CV results underscore the excellent electrochemical response of NiO electrodes to H_2O_2 . The cathodic peak current at -1.4 V showed a strong linear correlation with the concentration of H_2O_2 across the tested range, demonstrating the sensor's sensitivity and reliability.

The electrochemical activity of the NiO electrode was further influenced by experimental parameters such as pH, scan rate, and stirring speed. The optimal pH was determined to be 13 (0.1 M NaOH), where the sensor achieved maximum sensitivity and peak definition. Increasing the scan rate led to a noticeable shift in peak positions due to kinetic limitations, while a scan rate of 100 mV·s⁻¹ was found to balance sensitivity and signal stability. Additionally, the stirring speed was optimized to 1290 rpm, ensuring efficient mass transfer of H₂O₂ to the electrode surface without compromising electrode integrity [5].

The sensor also demonstrated excellent long-term stability, retaining over 95% of its initial performance after 30 days of storage. SEM analysis revealed that the nanostructured NiO surface retained its morphological integrity after multiple uses, although some fusion of nanostructures occurred, leading to a minor reduction in surface area and, consequently, a slight decrease in sensitivity after the 10th cycle. This durability highlights the practicality of NiO electrodes for repeated measurements in real-world applications, including plant stress monitoring.

In summary, the NiO electrodes, with their wall-shaped nanostructures, offer a promising platform for the electrochemical detection of H₂O₂. Their high sensitivity, broad linear range, low detection limit, and excellent stability make them ideal candidates for real-time monitoring of oxidative stress in biological systems, particularly in plant physiology and environmental sensing applications.

6.2. Sensitivity Analysis of Metal Oxide Electrodes for H₂O₂ Detection

After characterizing the electrochemical behavior of the metal oxide electrodes using cyclic voltammetry, amperometry was employed as the primary method to assess the sensitivity, linearity, and limit of detection (LOD) of each electrode toward hydrogen peroxide (H₂O₂). Amperometry is a well-suited technique for this study due to its ability to provide real-time, quantitative current measurements in response to the analyte concentration under constant potential conditions. It is particularly advantageous for sensor development as it allows for the direct measurement of the electrochemical signal (current) produced by the oxidation or reduction reaction at the working electrode, without the influence of scan rate or waveform.

The amperometric experiments were conducted at a fixed potential, typically chosen based on the redox peak identified in the CV study for maximum sensitivity and minimal interference. The parameters measured in these experiments included the steady-state current response of the electrode to varying concentrations of H₂O₂, the linearity of the current–concentration relationship (i.e., the calibration curve), the sensitivity (slope of the calibration curve), and the limit of detection (LOD), calculated as three times the standard deviation of the baseline noise divided by the sensitivity.

6.2.1. Copper Oxide (CuO) Electrode

Amperometric measurements for the petal-like CuO electrode were carried out in 0.1 M NaOH at -0.2 V (vs. Ag/AgCl), a potential that maximized the sensitivity of the electrode toward H₂O₂ while minimizing interference from other species [3]. The current response increased linearly with the concentration of H₂O₂ across a wide range (from 20 μM to 1300 μM).

- Calibration Curve: The calibration curve showed an excellent linear relationship between the current and H₂O₂ concentration, with a regression coefficient (R²) of 0.9997.
- Sensitivity: The sensitivity of the CuO electrode was measured as $505.11~\mu\text{A/mM}$ (or 0.5051~A/mM), which is among the highest reported values for H_2O_2 detection using CuO-based sensors.
- Limit of Detection (LOD): The LOD was calculated as 1.05 μM, indicating the electrode's ability to detect very low concentrations of H₂O₂.

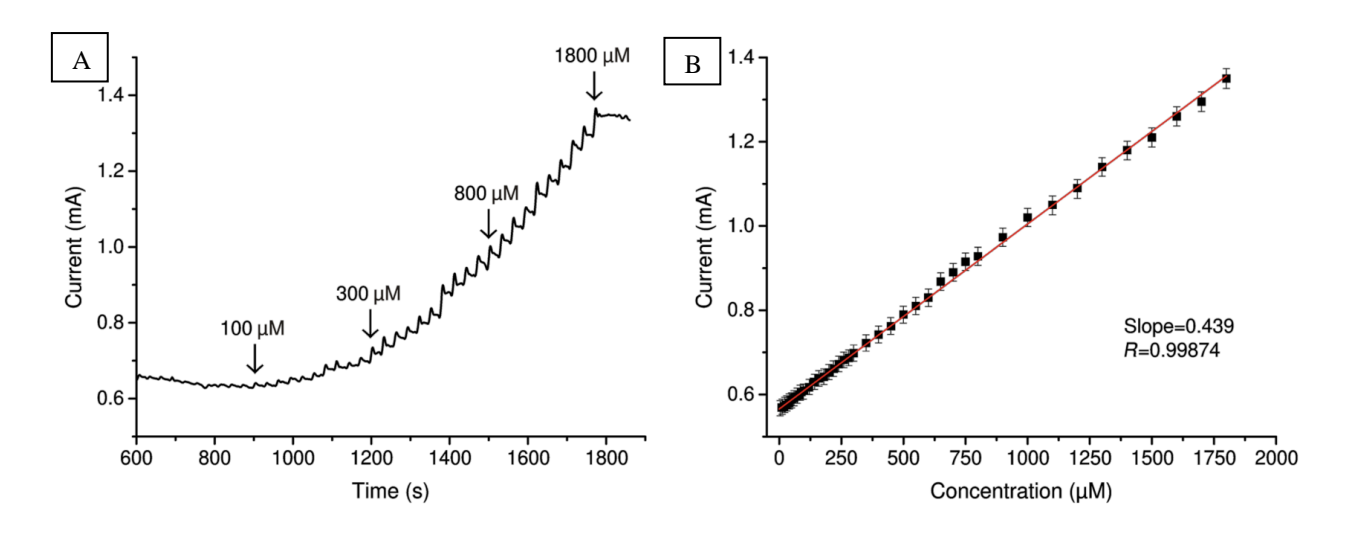


Figure 25. A) Amperometric response of the nanostructured CuO electrode in 0.1 M NaOH with stepwise addition of H_2O_2 .

B) The corresponding calibration curve [3].

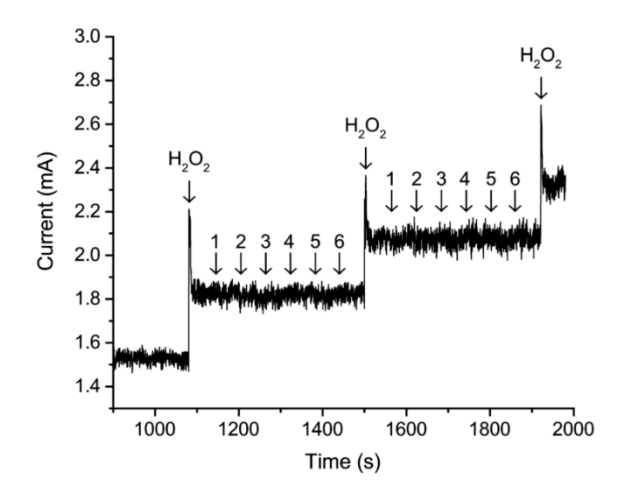


Figure 26. Amperometric response of the nanostructured CuO electrode in 0.1 M NaOH with stepwise addition of H₂O₂ at concentrations from 100 to 300 μM and the most common interfering substances: (1) ascorbic acid, (2) uric acid, (3) dopamine, (4) NaCl, (5) glucose, and (6) acetaminophen [3].

In addition to these performance parameters, the CuO electrode demonstrated high selectivity toward H₂O₂ in the presence of common interferents such as ascorbic acid, uric acid, dopamine, and NaCl. The signal from these substances did not significantly alter the baseline current or interfere with the H₂O₂ detection signal.

6.2.2. Cobalt Oxide (Co₃O₄) Electrode

The Co₃O₄ electrode, fabricated by hydrothermal synthesis, was tested at a fixed potential of -1.23 V (vs. Ag/AgCl), chosen based on the CV results to optimize sensitivity toward H₂O₂ [4]. Amperometric experiments showed a steady and measurable increase in current with increasing H₂O₂ concentration.

- Calibration Curve: The calibration curve showed a linear correlation between the current and H_2O_2 concentration in the range from 0.2 mM to 2 mM, with $R^2 = 0.9976$.
- Sensitivity: The sensitivity of the Co₃O₄ electrode was determined to be 22 μA/mM, which is lower than that of the CuO electrode but still suitable for practical applications, particularly in healthcare and environmental monitoring.

• Limit of Detection (LOD): The LOD for the Co₃O₄ electrode was 7.14 μM, which is comparable to that of CuO in certain conditions, and well within the biologically relevant range of H₂O₂ in body fluids.

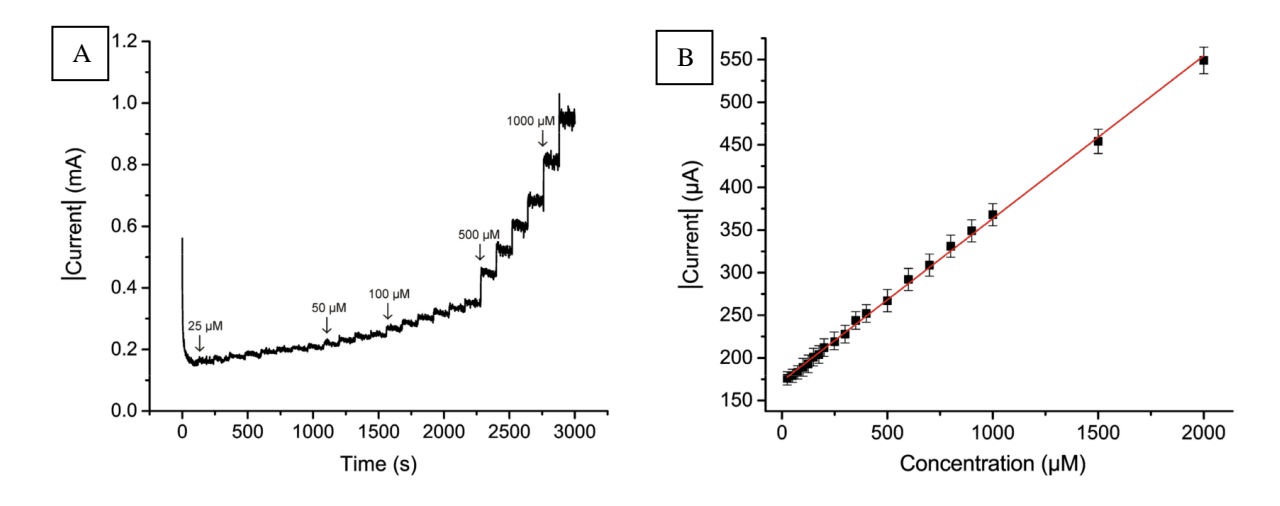


Figure 27. A) Chronoamperograms obtained in a 0.1 M NaOH supporting electrolyte for Co_3O_4 nanostructured electrode for -1.2 V peak potential obtained by gradually adding H_2O_2 . B) Calibration curve for concentration-current dependence [4].

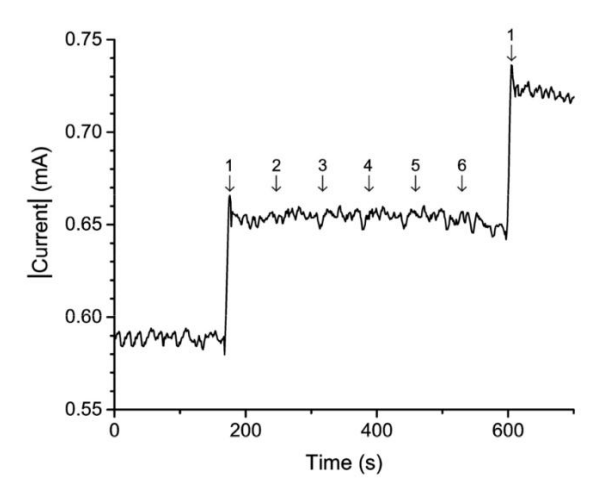


Figure 28. Interference study with the addition of H_2O_2 (1) and potential interferents NaCl (2), KNO3 (3), glucose (4), citric acid (5), and ascorbic acid (6). (e) Chronoamperograms obtained in a 0.1 M NaOH supporting electrolyte [4].

Notably, the Co₃O₄ electrode exhibited a good response in real samples such as milk and contact lens storage solution, with a recovery rate exceeding 95%. This confirms the suitability of the electrode for quantitative analysis in complex matrices. The selectivity was also evaluated, showing minimal interference from common biological and chemical species.

6.2.3. Nickel Oxide (NiO) Electrode

Amperometric measurements for the wall-shaped NiO nanostructure electrode were conducted in a 0.1 M NaOH solution at a working potential of -1.4 V (vs. Ag/AgCl) [5]. This potential was chosen to optimize the sensitivity of the NiO-based electrode toward hydrogen peroxide while minimizing interference from other electroactive species. The electrode exhibited a clear and reproducible current response to the addition of H₂O₂, with a strong dependence of the current on the H₂O₂ concentration.

The electrochemical behavior of the NiO electrode was characterized over a broad range of H_2O_2 concentrations, from 25 μ M to 4 mM. A stable and linear current response was observed, indicating the electrode's suitability for quantitative H_2O_2 detection in complex matrices such as plant extracts.

The calibration curve for the NiO electrode was obtained by measuring the current response at -1.4 V with incremental additions of H₂O₂. The resulting data showed a highly linear relationship between the current and the H₂O₂ concentration, with a correlation coefficient (R²) of 1.00 (as implied by the stepwise increase in current in response to H₂O₂). This linear relationship was consistent across the entire range of H₂O₂ concentrations tested, highlighting the electrode's reliability and accuracy.

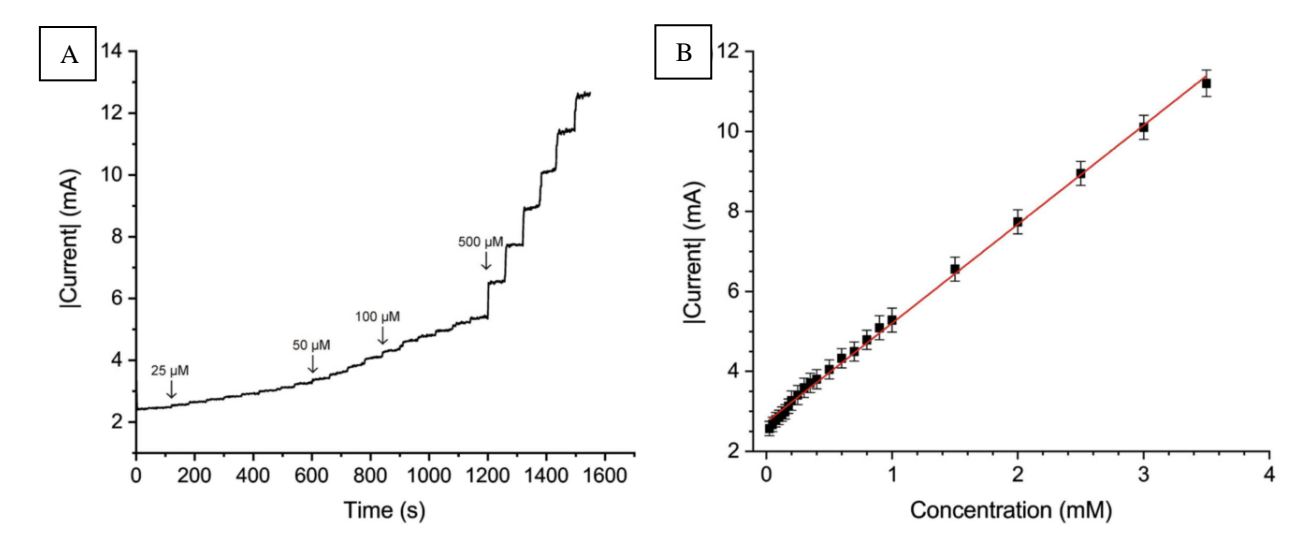


Figure 29. A) The chronoamperogram captured in a 0.1 M NaOH supporting electrolyte for the NiO nanostructured electrode at a peak potential of -1.4 V, obtained with gradual addition of H_2O_2 . B) A calibration curve illustrating the concentration—current relationship [5].

The sensitivity of the NiO electrode was calculated as 2474 μ A·mM⁻¹ (or 15.46 mA·mM⁻¹·cm⁻²) based on the slope of the calibration curve. This value is exceptionally high when compared to previously reported NiO-based electrochemical sensors, indicating the superior detection capability of the wall-shaped NiO nanostructure configuration. The high sensitivity is attributed to the large surface area provided by the nanostructured coating, which enhances the catalytic activity of the NiO electrode toward H₂O₂ oxidation.

The limit of detection (LOD) for the NiO electrode was determined using the 3:1 signal-to-noise (S/N) ratio criterion. Based on the noise observed in the baseline current measurements, the LOD was calculated to be 1.59 μ M. This low LOD demonstrates the electrode's ability to detect trace levels of H₂O₂, making it suitable

for applications in plant stress biomarker detection, where the concentration of H₂O₂ can be very low but physiologically significant.

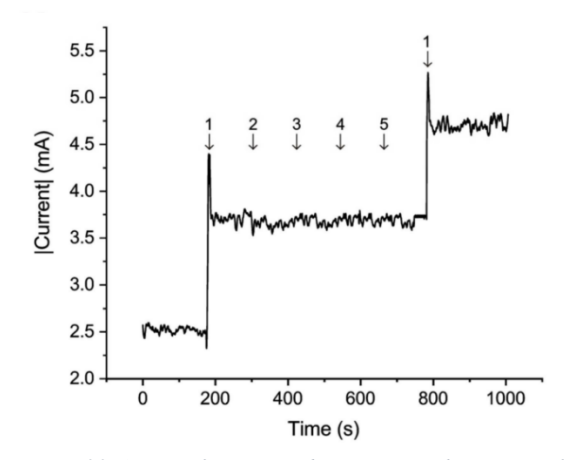


Figure 30. An interference study examining the impact of H_2O_2 addition (1) alongside common plant interferents, including NaCl (2), glucose (3), citric acid (4), and ascorbic acid (5) [5].

The NiO electrode exhibited excellent selectivity toward H₂O₂ in the presence of common interferents typically found in plant extracts, such as ascorbic acid, glucose, citric acid, and sodium chloride. No significant changes in the baseline current or in the response to H₂O₂ were observed when these substances were introduced to the working solution. The electrode's resistance to interference was likely due to the catalytic specificity of the NiO surface, which preferentially oxidized H₂O₂ while remaining largely unaffected by the redox properties of the interfering species.

The stability of the NiO electrode over time was assessed by performing repeated measurements of the current response at -1.4 V in a 0.1 M NaOH solution containing 2 mM H₂O₂. The peak current value decreased by less than 4% over a 30-day period, indicating that the electrode retained its functionality and sensitivity with minimal degradation. Additionally, the electrode demonstrated stable performance even after multiple reuse cycles, with only a 7% reduction in sensitivity after the tenth measurement [5]. Scanning electron microscopy (SEM) analysis of the electrode surface after ten uses revealed that while some thin nanostructures had fused, the overall surface morphology remained intact, preserving the electrode's sensing capabilities.

In summary, the NiO electrode based on wall-shaped nanostructures demonstrated excellent performance in the detection of H₂O₂, with high sensitivity, low LOD, and good selectivity and stability. These characteristics make it a promising candidate for real-time monitoring of oxidative stress in plants, particularly in the context of salt stress tolerance studies.

7. Plant Stress Detection Using H₂O₂ Electrochemical Sensors

7.1. Sensor Application

Hydrogen peroxide (H₂O₂) is a central reactive oxygen species (ROS) that functions both as a signaling molecule and an indicator of oxidative stress in plants under abiotic and biotic stress conditions. Elevated levels of H₂O₂ reflect disruptions in cellular redox homeostasis induced by salinity, herbicides, or other environmental stressors. Electrochemical detection of H₂O₂ provides a robust approach for real-time monitoring of plant stress responses. By integrating these nanostructured electrodes into electrochemical systems, researchers can assess the impact of stress factors on plants and monitor the effectiveness of stress mitigation strategies, such as the application of nanoparticles. This makes them valuable tools for agricultural and environmental research.

This study employed non-enzymatic electrochemical sensors fabricated using nanostructured metal oxides—Co₃O₄, CuO, and NiO. These sensors exploit the intrinsic electrocatalytic activity of transition metal oxides toward H₂O₂ oxidation, further amplified by nanostructuring. The morphological engineering of the sensing layer, particularly into petal-like, nanowall, and fiber-like architectures, resulted in significantly enhanced electroactive surface areas, promoting higher sensitivity and selectivity.

Each sensor type was tailored to specific applications:

- Co₃O₄ nanopetals were optimized for barley extracts and demonstrated excellent catalytic response
 in complex matrices.
- NiO nanowalls enabled effective H_2O_2 sensing in rye under salt stress, offering a high surface area and low detection limit (LOD = 1.59 μ M, sensitivity = 2474 μ A·mM⁻¹).
- CuO nanostructures, used in a multisensor configuration with Co₃O₄, provided complementary selectivity, enhancing overall signal fidelity in rye extracts subjected to salt and herbicide stress.

7.2. Experimental Procedures

Electrochemical measurements were conducted in three-electrode cells with Ag/AgCl as the reference and carbon as the counter electrode. The working electrodes were nanostructured Co₃O₄, CuO, or NiO on metal wires (iron or copper substrates), synthesized by hydrothermal and chemical oxidation methods.

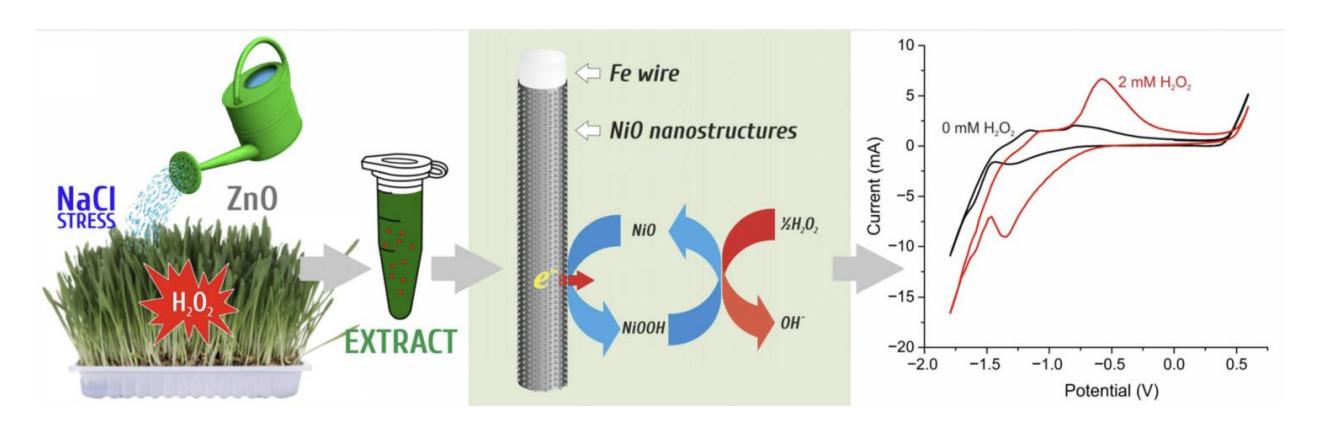


Figure 31. Shematic display of the process of electrochemical detection of H₂O₂ in rye samples with induced salt stress [5].

Plant Material and Treatments:

- Species: Barley (Hordeum vulgare L.) [6] and Rye (Secale cereale L.) [5] [7].
- Stress Induction: Plants were exposed to 0.2 M NaCl to simulate salinity stress. Additional groups received Fe₃O₄ or ZnO nanoparticles to mitigate induced stress tolerance.
- Duration: Total cultivation lasted 4 weeks, with stress/nanoparticle treatments applied during the final 3 weeks.

Sample Preparation:

- Green plant tissues (typically 10 g per 250 mL) were extracted in 0.1 M NaOH and stored under cold, dark conditions to stabilize H₂O₂.
- For optical measurements, chlorophyll was extracted in ethanol for stress validation via photosynthetic pigment loss.

Electrochemical Calibration and Interference Tests:

- Sensors were calibrated using H₂O₂ standards from 25 μM to 7 mM.
- Interference resistance was evaluated against NaCl, glucose, citric acid, and ascorbic acid. Petallike Co₃O₄ structures exhibited the best resilience to interferences from plant matrix components

Data were acquired using CV, SWV, and amperometry. CV scans typically ranged from -1.3 V to +0.5 V (vs. Ag/AgCl), with scan rates of 100 mV·s⁻¹. Amperometric detection was carried out at a fixed potential (e.g., -1.2 V) corresponding to the H_2O_2 oxidation peak.

7.3. Plant stress detection using CuO and Co3O4 nanostructured electrochemical sensors

In this studies [5] [6] [7], plant samples subjected to NaCl- and glyphosate-induced stress exhibited significantly elevated H_2O_2 concentrations compared to the control group, with increases of up to 163.02 μ M and 223.03 μ M, respectively. These findings were further supported by optical absorption measurements, which revealed a substantial decrease in chlorophyll content—up to 35% in the most severely stressed samples (Table 2). The inverse correlation between H_2O_2 concentration and chlorophyll levels underscores the role of oxidative stress in impairing photosynthetic efficiency and overall plant health. These results confirm that H_2O_2 is not only a byproduct of stress, but a key indicator of its physiological impact on plants.

Moreover, the study demonstrated that the presence of H₂O₂ is not limited to abiotic stressors. Exposure to glyphosate, a potent herbicide, resulted in H₂O₂ accumulation at levels comparable to those observed under salt stress, indicating that organic stressors can elicit similar oxidative responses. This suggests that H₂O₂ can serve as a universal marker of stress in plants, regardless of the type or source of stressor.

Importantly, the addition of low concentrations of H₂O₂ to irrigation water had a positive effect on plant growth, as evidenced by increased shoot length and chlorophyll content compared to the control [7]. This indicates that H₂O₂ is not inherently harmful, but becomes problematic only when its concentration exceeds the plant's capacity to neutralize it. The results highlight the delicate balance that plants must maintain between ROS production and scavenging, and the critical role of H₂O₂ as a signal for stress.

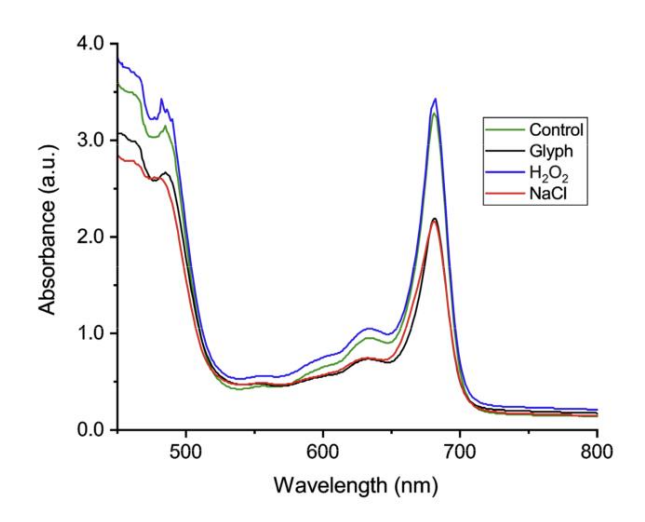
Previously developed non-enzymatic electrochemical sensors using nanostructured CuO and Co₃O₄ electrodes were utilized for plant stress detection. These materials were chosen based on their high catalytic activity, stability, and compatibility with electrochemical detection methods. The sensors demonstrated excellent performance in detecting H₂O₂ in a complex plant matrix such as rye and barley juice, with detection limits of 1.34 μM for CuO and 1.05 μM for Co₃O₄ (pages 62 and 63). Both sensors exhibited good linear dependence over a wide concentration range (20 μM to 7 mM), high selectivity toward H₂O₂, and resistance to interference from other organic and inorganic compounds present in plant tissue.

The ability of the sensors to detect H₂O₂ in the presence of a complex matrix underscores their practicality for use in real-world agricultural and environmental applications. Unlike enzymatic sensors, which are prone to degradation and require careful temperature control, the non-enzymatic sensors based on CuO and Co₃O₄ are stable, durable, and suitable for field deployment. The miniaturization of these sensors also makes them ideal for integration into portable devices, enabling on-site monitoring of plant stress in agricultural settings.

7.4. Correlation Between H₂O₂ Accumulation and Plant Vital Functions

The relationship between H₂O₂ levels and plant physiological functions was further validated by comparing the results of electrochemical H₂O₂ detection with optical chlorophyll measurements. A clear inverse correlation was observed: as H₂O₂ concentrations increased, chlorophyll levels decreased, particularly in samples exposed to NaCl and glyphosate. The control samples, which showed minimal H₂O₂ accumulation, exhibited the highest chlorophyll content and longest shoot lengths. In contrast, stressed samples showed reduced chlorophyll levels and stunted growth, indicating impaired photosynthetic activity and overall plant vigor.

The study also revealed that H₂O₂-irrigated plant samples exhibited enhanced chlorophyll content and improved growth characteristics compared to the control. This suggests that small, controlled amounts of H₂O₂ may act as a beneficial signaling molecule, promoting root development and nutrient uptake. The positive effects observed in H₂O₂-treated samples contrast sharply with the detrimental effects of unregulated H₂O₂ accumulation in stressed plants, further emphasizing the dual nature of H₂O₂ in plant physiology.



Stress Factor	As Prepared Samples		
	Chl(a), (mg/g)	Chl(b), (mg/g)	
H ₂ O ₂	47.80	19.27	
Control	45.88	17.82	
Glyphosate	31.39	14.40	
NaCl	30.10	19.21	

Table 2. The decrease in chlorophyl contents for various stress inducers in rye [7]. The stress inducers were applied during irrigation.

Figure 32. Light absorbance spectrum for rye samples [7].

The data obtained from the electrochemical sensors align closely with the optical measurements, providing a consistent and comprehensive picture of stress-induced changes in rye plants. This cross-verification strengthens the argument that H_2O_2 can be used not only as a stress marker, but as a quantitative indicator of stress severity. The combination of electrochemical and optical methods offers a powerful multi-faceted approach to stress assessment in plants.

Hydrogen peroxide (H₂O₂) has been unequivocally established as a reliable biomarker of plant stress, with its concentration directly linked to the severity of stressors such as salt and herbicides. The development of non-enzymatic electrochemical sensors based on nanostructured CuO and Co₃O₄ electrodes has provided a

robust and sensitive method for detecting H_2O_2 in plant tissues. These sensors demonstrated excellent performance in terms of sensitivity, selectivity, and stability, even in the complex matrix of rye juice. The correlation between elevated H_2O_2 levels and reduced chlorophyll content further validates the use of H_2O_2 as an indicator of oxidative stress in plants.

The application of these sensors in agricultural and environmental research offers a powerful tool for understanding plant responses to stress and for developing strategies to enhance crop resilience and productivity.

7.5. Utilization of Nanoparticles for Stress Mitigation and Sensor Application Field Expansion

The integration of nanoparticles into agricultural practices has opened new avenues for stress mitigation, with these nanomaterials playing a pivotal role in alleviating oxidative stress in plants. In this context, the sensors developed in this study, based on NiO, CuO and Co₃O₄ nanostructures, demonstrate significant potential as monitoring tools to detect varying stress levels before, during, and after nanoparticle application. By quantifying hydrogen peroxide (H₂O₂) in plant tissues, the sensors can effectively assess the efficacy of nanoparticles in reducing oxidative damage. For instance, the addition of ZnO [5] or Fe₃O₄ [6] nanoparticles to irrigation water has been shown to significantly reduce H₂O₂ concentrations in rye under salt stress, as demonstrated in earlier studies. These nanoparticles not only help in scavenging reactive oxygen species (ROS) but also enhance the plant's natural antioxidant systems. The sensors, with their high sensitivity and selectivity, enable real-time tracking of H₂O₂ levels, providing a dynamic feedback loop to evaluate stress mitigation success. This capability is crucial for optimizing nanoparticle application rates and timing, ensuring that plants receive the most effective treatment.

Plant Species	Type of Stress	Stress Mitigator	H ₂ O ₂ Concentration (μM)
Rye (Secale cereale	Salt stress (NaCl)	— (Control, no mitigation)	500
L.)		ZnO nanoparticles (50 mg·L ⁻¹)	190
		ZnO nanoparticles (100 mg·L ⁻¹)	130
Barley (Hordeum	Salt stress (NaCl)	— (Control, no mitigation)	500
vulgare L.)		Fe ₃ O ₄ nanoparticles (72 mg·L ⁻¹)	150

Table 3. Comparison of detected H_2O_2 levels in plants with and without stress mitigation via nanoparticle irrigation.

The versatility of the NiO, CuO and Co₃O₄-based sensors extends further into ariculture: they can be employed in a feedback-driven system to monitor the physiological response to fertilizers and chemical interventions. For example, by continuously measuring H₂O₂ levels in treated plants, farmers and researchers can adjust fertilizer dosages and application methods based on real-time data. This adaptive approach enhances the precision of stress management strategies, potentially leading to improved crop

yields and resilience. Moreover, the sensors' ability to function in complex plant matrices, such as rye juice, underscores their robustness and reliability in field conditions. The non-enzymatic nature of these sensors also ensures their longevity and stability, making them suitable for long-term deployment in agricultural settings. Thus, the development of these sensors not only advances our ability to detect stress biomarkers but also facilitates the practical application of fertilizers and chemicals in stress mitigation, creating a powerful synergy between advanced materials and electrochemical sensing technologies.

7.6. Chapter Summary

After presenting the detailed electrochemical performance of each metal oxide electrode—namely CuO, Co₃O₄, and NiO—in detecting hydrogen peroxide, it is important to summarize and compare their key analytical parameters in order to assess their relative merits and suitability for different applications. Each electrode demonstrated distinct characteristics in terms of sensitivity, linear range, limit of detection, selectivity, and long-term stability. To facilitate a direct and structured comparison, a summary table is provided below, which consolidates the most relevant performance metrics for each material. This comparative overview highlights the strengths of each system and aids in determining the optimal electrode for specific sensing environments, such as biomedical, environmental, or plant physiological monitoring.

Parameter	Copper Oxide (CuO)	Cobalt Oxide (Co ₃ O ₄)	Nickel Oxide (NiO)	
Electrolyte	0.1 M NaOH	0.1 M NaOH	0.1 M NaOH	
Applied Potential	-0.2 V (vs. Ag/AgCl)	-1.23 V (vs. Ag/AgCl)	-1.4 V (vs. Ag/AgCl)	
Linear Detection Range	20 μM to 1300 μM	0.2 mM to 2 mM	25 μM to 4 mM	
Correlation Coefficient (R²)	0.9997	0.9976	1.00	
Sensitivity	505.11 μA/mM (0.5051 A/mM)	22 μA/mM	2474 μA/mM (15.46 mA/mM·cm²)	
Limit of Detection (LOD)	1.05 μM (3σ/sensitivity)	7.14 μΜ	1.59 μΜ	
Selectivity	High; no significant interference from ascorbic acid, uric acid, dopamine, NaCl	Good; minimal interference from NaCl, KNO ₃ , glucose, citric acid, ascorbic acid	Excellent; no interference from ascorbic acid, glucose, citric acid, NaCl	
Application Suitability	High for low-concentration H ₂ O ₂ detection (biological, environmental)	Suitable for healthcare and environmental monitoring	· · · · · · · · · · · · · · · · · · ·	

Table 4. Comparative Performance of CuO, Co₃O₄, and NiO Electrodes for H₂O₂ Detection

Conclusions

- 1. Laser-assisted and hydrothermal synthesis techniques enable the controlled fabrication of highly uniform and patterned ZnO nanoneedles, significantly enhancing their structural fidelity and suitability for application-specific design in electrochemical systems.
 - a. The synthesis of ZnO nanoneedles was successfully controlled through both hydrothermal and laser-assisted methods. ZnO nanoneedles synthesized using hydrothermal techniques on preheated substrates yielded highly uniform structures. The laser-assisted method, using a 532 nm laser at 15,5 MW/m2 with a scan speed of 55 mm/min, enabled selective and precise patterning of ZnO nanostructures with minimal parasitic growth.
- 2. The morphology of metal oxide nanostructures—such as CuO nanopetals, Co₃O₄ nanofibers, and NiO nanowalls—can be systematically tuned via synthesis parameters to optimize electrochemical activity, surface area, and stability, offering tailored sensor performance for diverse applications.
 - a. The synthesis of CuO nanostructures via hydrothermal oxidation yielded nanopetals with a flower-like morphology (page 59) that exhibited superior electrochemical activity. The optimal synthesis duration for CuO was 3 hours at 90°C in a solution composed of 10 mL of 10 M NaOH, 5 mL of 1 M (NH₄)₂S₂O₈, and 26 mL of distilled water.
 - b. Co₃O₄ chloride-assisted synthesis led to the formation of long, uniform nanofibers assembled into honeycomb-like structures (page 57), which demonstrated high adhesion, large surface area, and excellent electrochemical response. The optimal synthesis duration for Co₃O₄ was 5 hours at 95°C in equimolar aqueous solution of 0.1 M CoCl₂·6H₂O and 0.1 M hexamethylenetetramine (CH₄N₂O).
 - c. For NiO, hydrothermal synthesis on iron wires produced wall-shaped nanowalls with a complex three-dimensional architecture and spherical flower-like formations (page 60). The optimal synthesis duration for NiO was 5 hours at 95°C 0.1 M equimolar mixture of nickel nitrate hexahydrate (Ni(NO₃)₂·6H₂O) and hexamethylenetetramine (C₆H₁₂N₄).
- 3. The development of electrochemical platform designs enabled targeted detection of analyte in diverse applications:
 - a. Custom-Built Electrochemical Cell with Nanostructured Electrodes (page 49) demonstrated high suitability for plant extract analysis for stress monitoring.
 - b. Mass-Produced PCB Chip Electrochemical Cell (page 50) demonstrated the capability of analyzing small volume samples (down to 10 uL) for herbicide application monitoring.
 - c. Miniaturized Droplet-Based Electrochemical Cell (page 51) provides capabilities to perform wettability dynamics studies for various nanostructure morphologies.

- 4. Nanostructured NiO, Co₃O₄, and CuO electrodes exhibit exceptional sensitivity and selectivity for hydrogen peroxide detection in plant extracts, enabling the real-time monitoring of oxidative stress under abiotic and herbicide-induced conditions.
 - a. Electrochemical sensors based on nanostructured NiO, Co₃O₄, and CuO were tested for H₂O₂ detection in rye and barley.
 - i. The NiO-based sensor demonstrated detection limit (LOD) of 1.59 μM and a sensitivity of 2474 $\mu A \cdot m M^{-1}$.
 - ii. Co₃O₄ electrodes demonstrated LOD of 7.14 μM and sensitivity of 22 μA·mM⁻1.
 - iii. CuO sensors exhibited LOD of 1.05 μM and sensitivity of 505 μA·mM⁻¹.
 - iv. These sensors were successfully tested against common plant interferents.
- 5. The developed electrochemical sensors, validated through complementary optical and molecular methods, demonstrate high correlation with physiological stress indicators, establishing H₂O₂ as a reliable biomarker for plant stress assessment.
 - a. The electrochemical detection of H_2O_2 was validated using optical measurements (chlorophyll content) and molecular analyses (RAPD). During this study, it was established that for stressed rye samples:
 - i. The chlorophyll content were reduced by up to 35% when compared to control;
 - ii. The created sensors detected H_2O_2 levels up to 223.03 μM with stressed rye samples;
 - iii. The control samples had H2O2 levels less than LOD.
 - b. Additionally, glyphosate-stressed plant samples exhibited significant genotoxic effects as evidenced by RAPD analysis, indicating DNA-level changes. The integration of electrochemical data with optical and molecular validation methods strengthens the credibility of H_2O_2 as a key physiological marker and supports the use of developed sensors in agricultural monitoring systems.

Acknowledgements

Completing this PhD thesis has been a long journey, and I am deeply grateful to those who have supported, guided, and inspired me along the way.

First and foremost, I thank my advisor, Dr. Phys **Vjaceslavs Gerbreders**, for his exceptional mentorship and unwavering belief in this research. His expertise, guidance, and critical feedback were indispensable in shaping this work. Under his supervision, I developed essential skills in experimental design, data analysis, and scientific reasoning—lessons that have shaped my academic growth.

I am also deeply thankful to my colleagues and co-authors—Marina Krasovska, Irena Mihailova, Eriks Sledevskis, Edmunds Tamanis, Andrejs Ogurcovs, Janis Snikeris and Jans Keviss—for their invaluable collaboration. Their contributions ranged from refining experimental techniques to providing critical insights during manuscript preparation. Their technical support, scientific discussions, and joint efforts in publishing our findings were essential in advancing this research.

To my friends and family, I owe immense gratitude for their patience, encouragement, and unwavering support. Their belief in me kept me motivated through the most challenging moments.

Finally, I acknowledge the **Daugavpils University** and **G.Liberts' Innovative Microscopy Centre** for providing the scientific equipment and laboratories that made this research possible.

This thesis has been funded by **European Social Fund (ESF)** under project nr. 8.2.2.0/20/I/003 *Daugavpils University strategic specialization and academic personnel professional competence strengthening*.

References

- [1] V. Gerbreders, M. Krasovska, I. Mihailova, V. Mizers, E. Sledevskis and A. Bulanovs, «Selective laser-assisted patterning of ZnO: effects of synthesis parameters on nanostructure morphology,» *Latvian Journal Of Physics And Technical Sciences*, 2024.
- [2] I. Mihailova, M. Krasovska, E. Sledevskis, V. Gerbreders, V. Mizers, A. Bulanovs and A. Ogurcovs, «Selective patterned growth of ZnO nanoneedle arrays,» *Latvian Journal Of Physics And Technical Sciences*, 2023.
- [3] I. Mihailova, V. Gerbreders, M. Krasovska, E. Sledevskis, V. Mizers, A. Bulanovs and A. Ogurcovs, «A non-enzymatic electrochemical hydrogen peroxide sensor based on copper oxide nanostructures,» *Bailstein Journal of Nanotechnology*, 2022.
- [4] V. Mizers, V. Gerbreders, M. Krasovska, E. Sledevskis, I. Mihailova, A. Ogurcovs, A. Bulanovs and A. Gerbreders, «Non-Enzymatic Co3O4 Nanostructure-Based Electrochemical Sensor for H2O2 Detection,» *Latvian Journal of Physics and Technical Sciences*, 2023.
- [5] V. Gerbreders, M. Krasovska, E. Sledevskis, I. Mihailova, V. Mizers, J. Keviss and A. Bulanovs, «Enhancing Salt Stress Tolerance in Rye with ZnO Nanoparticles: Detecting H2O2 as a Stress Biomarker by Nanostructured NiO Electrochemical Sensor,» *Crystals*, 2024.
- [6] V. Gerbreders, M. Krasovska, E. Sledevskis, I. Mihailova and V. Mizers, «Co3O4 Nanostructured Sensor for Electrochemical Detection of H2O2 as a Stress Biomarker in Barley: Fe3O4 Nanoparticles-Mediated Enhancement of Salt Stress Tolerance,» *Micromachines*, 2024.
- [7] I. Mihailova, M. Krasovska, E. Sledevskis, V. Gerbreders, V. Mizers and A. Ogurcovs, «Assessment of Oxidative Stress by Detection of H2O2 in Rye Samples Using a CuO- and Co3O4-Nanostructure-Based Electrochemical Sensor,» *Chemosensors*.
- [8] V. Mizers, V. Gerbreders, E. Sledevskis, I. Kokina, E. Tamanis, M. Krasovska, I. Mihailova, A. Orugcovs and A. Bulanovs, «Electrochemical detection of small volumes of glyphosate with mass-produced non-modified gold chips,» *Latvian Journal Of Physics And Technical Sciences*, 2020.

- [9] V. Gerbreders, M. Krasovska, I. Mihailova, E. Sledevskis, A. Ogurcovs, E. Tamanis, V. Auksmuksts, A. Bulanovs and V. Mizers, «Morphology influence on wettability and wetting dynamics of ZnO nanostructure arrays,» *Latvian Journal of Physics And Technical Sciences*, 2022.
- [10] M. Zhao, Y. Zeng, X. Zhang and H. Liang, «Recent Advances in Electrochemical Cell Design for Concurrent Chemical Production and Electricity Generation,» *ChemElectroChem*, 2024.
- [11] C. Shen, P. Zhou and D. Guo, «Potential profile of electrolytic cell and influence of electrolyte resistance in three-electrode electrochemical testing,» *Electrochimica Acta*.
- [12] X. Guo, L. Ma, Z. Fu, J. Wang, Z. Li, B. Shi, Y. Li, G. Yang, L. Lu and D. Zhang, «Molecular understanding of the effects of electrode potential and electric double layer on the adsorption process of two azole-based corrosion inhibitors,» *Corrosion Science*, 2025.
- [13] C. Qiao, Q. Wu, L. Hao, X. Zhang, T. Chowwanonthaypunya, M. Sun, X. An and W. Ke, «Material selection in making electrochemical impedance spectroscopy sensor for electrolyte thickness measurement in marine atmosphere,» *Corrosion Science*, 2023.
- [14] G. Keles, E. S. Ataman, S. B. Taskin, I. Polatoglu and S. Kurbanoglu, «Nanostructured Metal Oxide-Based Electrochemical Biosensors in Medical Diagnosis,» *Biosensors*, 2024.
- [15] Z. Zhao, W. Lei, X. Zhang, B. Wang and H. Jiang, «ZnO-Based Amperometric Enzyme Biosensors,» *Sensors*, 2010.
- [16] I. M. Maafa, «Potential of Zinc Oxide Nanostructures in Biosensor Application,» *Biosensors*, 2025.
- [17] F. J. Holler and S. R. Crouch, Fundamentals of Analytical Chemistry, 9, Ред., Cengage Learning, 2013.
- [18] A. J. Bard and L. R. Faulkner, Electrochemical methods: Fundamentals and Applications, 2001.
- [19] P. Atkins, J. d. Paula and J. Keeler, Physical Chemistry, 11, Ред., Oxford University Press, 2018.
- [20] C. G. Zoski, Handbook of Electrochemistry, Elsevier Science, 2007.
- [21] A. P. F. Turner, «Biosensors: sense and sensibility,» Chemical Society Reviews, 2013.
- [22] A. Qurashi, J. H. Kim and Y.-B. Hahn, «Direct fabrication of ZnO nanorods array on-chip system in solution and their electrical properties,» *Electrochemistry Communications*, 2012.

- [23] M. Kawakami, A. B. Hartanto, Y. Nakata and T. Okada, «Synthesis of ZnO Nanorods by Nanoparticle Assisted Pulsed-Laser Deposition,» *Japanese Journal of Applied Physics*, 2003.
- [24] J. Bae, J.-I. Hong, W. H. Han, Y. J. Choi and R. L. Snyder, «Superior field emission properties of ZnO nanocones synthesized by pulsed laser deposition,» *Chemical Physics Letters*, 2009.
- [25] Y. Liu, C. Gao, X. Pan, X. An, Y. Xie, M. Zhou, J. Song, H. Zhang, Z. Liu, Q. Zhao, Y. Zhang and E. Xie, «Synthesis and H2 sensing properties of aligned ZnO nanotubes,» *Applied Surface Science*, 2011.
- [26] W.-T. Chiou, W.-Y. Wu and J.-M. Ting, «Growth of single crystal ZnO nanowires using sputter deposition,» *Diamond and Related Materials*, 2003.
- [27] P. S. Venkatesh, S. Balakumar and K. Jeganathan, «Post-annealing effects on the structural and optical properties of vertically aligned undoped ZnO nanorods grown by radio frequency magnetron sputtering,» *RCS Advances*, 2014.
- [28] S. E. Ahn, J. S. Lee, H. Kim, S. Kim, B. H. Kang, K. H. Kim and G. T. Kim, «Photoresponse of solgel-synthesized ZnO nanorods,» *Applied Physics Letters*, 2004.
- [29] R. Chai, R. Yuan, Y. Chai, C. Ou, S. Cao and X. Li, «Amperometric immunosensors based on layer-by-layer assembly of gold nanoparticles and methylene blue on thiourea modified glassy carbon electrode for determination of human chorionic gonadotrophin,» *Talanta*, 2008.
- [30] L. Chen, B. Gu, G. Zhu, Y. Wu, S. Liu and C. Xu, «Electron transfer properties and electrocatalytic behavior of tyrosinase on ZnO nanorod,» *Journal of Electroanalytical Chemistry*, 2008.
- [31] A. Wei, X. W. Sun, J. X. Wang, Y. Lei, X. P. Cai, C. M. Li, Z. L. Dong and W. Huang, «Enzymatic glucose biosensor based on ZnO nanorod array grown by hydrothermal decomposition,» *Applied Physics Letter*, 2006.
- [32] C. Xia, N. Wang, L. Lidong and G. Lin, «Synthesis and characterization of waxberry-like microstructures ZnO for biosensors,» *Sensors and Actuators B: Chemical*, 2008.
- [33] J. Anusha, H.-J. Kim, A. T. Fleming, S. J. Das, K.-H. Yu, B. C. Kim and C. J. Raj, «Simple fabrication of ZnO/Pt/chitosan electrode for enzymatic glucose biosensor,» *Sensors and Actuators B: Chemical*, 2014.

- [34] M. B. Wayu, R. T. Spidle, T. Devkota, A. K. Deb, R. K. Delong, K. C. Ghosh, A. K. Wanekaya and C. C. Chusuei, «Morphology of hydrothermally synthesized ZnO nanoparticles tethered to carbon nanotubes affects electrocatalytic activity for H2O2 detection,» *Electrochimica Acta*, 2013.
- [35] V. Liustrovaite, D. Karoblis, B. Brasiunas, A. Popov, A. Katelnikovas, A. Kareiva, A. Ramanavicius, R. Viter, M. T. Giardi, D. Erts and A. Ramanaviciene, «Electrochemical Immunosensor for the Determination of Antibodies against Prostate-Specific Antigen Based on ZnO Nanostructures,» *International Journal of Molecular Sciences*, 2023.
- [36] M. B. Wayu, R. T. Spidle, T. Devkota, A. K. Deb, R. K. Delong, K. C. Ghosh, A. K. Wanekaya and C. C. Chusuei, «Morphology of hydrothermally synthesized ZnO nanoparticles tethered to carbon nanotubes affects electrocatalytic activity for H2O2 detection,» *Electrochimica Acta*, 2013.
- [37] R. Singh and J. Singh, «Recent advances in nanostructured cobalt oxide (Co3O4): Addressing methods and design strategies, challenges, and future directions for non-enzymatic sensor applications,» Sensors and Actuators: A. Physical, 2025.
- [38] M. Wang, X. Jiang, J. Liu, H. Guo and C. Liu, «Highly sensitive H2O2 sensor based on Co3O4 hollow sphere prepared via a template-free method,» *Electrochimica Acta*, 2015.
- [39] H. Dai, Y. Chen, X. Niu, C. Pan, H. Chen and X. Chen, «High-performance electrochemical biosensor for nonenzymatic H2O2 sensing based on Au@C-Co3O4 heterostructures,» *Biosensors and Bioelectronics*, 2018.
- [40] N. H. Khand, I. M. Palabiyik, J. A. Buledi, S. Ameen, A. F. Memon, T. Ghumro and A. R. Solangi, «Functional Co3O4 nanostructure-based electrochemical sensor for direct determination of ascorbic acid in pharmaceutical samples,» *Journal of Nanostructure in Chemistry*, 2021.
- [41] A. S. Chang, A. Tahira, F. Chang, N. N. Memon, A. Nafady, A. Kasry and Z. H. Ibupoto, «Silky Co3O4 nanostructures for the selective and sensitive enzyme free sensing of uric acid,» *RCS Advances*, 2021.
- [42] T. Zhe, M. Li, F. Li, R. Li, F. Bai, T. Bu, P. Jia and L. Wang, «Integrating electrochemical sensor based on MoO3/Co3O4 heterostructure for highly sensitive sensing of nitrite in sausages and water,» *Food Chemistry*, 2022.
- [43] M. Wu, Y. Hong, X. Zang and X. Dong, «ZIF-67 Derived Co3O4/rGO Electrodes for Electrochemical Detection of H2O2 with High Sensitivity and Selectivity,» *ChemistrySelect*, 2016.

- [44] S. Barkaoui, M. Haddaoui, H. Dhaouadi, N. Raouafi and F. Touati, «Hydrothermal synthesis of urchin-like Co3O4 nanostructures and their electrochemical sensing performance of H2O2,» *Journal of Solid State Chemistry*, 2015.
- [45] M. M. Shahid, P. Rameshkumar, W. J. Basirunc, U. Wijayantha, W. S. Chiu, P. S. Khiew and N. M. Huang, «An electrochemical sensing platform of cobalt oxide@gold nanocubes interleaved reduced graphene oxide for the selective determination of hydrazine,» *Electrochimica Acta*, 2018.
- [46] A. S. Chang, A. Tahira, F. Chang, A. G. Solangi, M. A. Bhatti, B. Vigolo, A. Nafady and Z. H. Ibupoto, «Highly Heterogeneous Morphology of Cobalt Oxide Nanostructures for the Development of Sensitive and Selective Ascorbic Acid Non-Enzymatic Sensor,» *Biosensors*, 2023.
- [47] Z. Liu, X. Xia, H.-K. Guan, Q. Liu, S.-S. Zhao, X.-L. Cheng, Q.-Q. Xu and S.-S. Li, «Hypersensitized electrochemical detection of Hg(II) based on tunable sulfur-doped porous Co3O4 nanosheets: Promotion Co2+/Co3+ valence change cycle and adsorption via introducing S,» *Chemical Engineering Journal*, 2022.
- [48] G. E. Uwaya, P. K. Sappidi and K. Bisetty, «Development of a Co3O4/rGO Modified Electrochemical Sensor for Highly Sensitive Riboflavin Detection,» *ChemElectroChem*, 2024.
- [49] L. Xiong, Y. Zhang, S. Wu, F. Chen, L. Lei, L. Yu and C. Li, «Co3O4 Nanoparticles Uniformly Dispersed in Rational Porous Carbon Nano-Boxes for Significantly Enhanced Electrocatalytic Detection of H2O2 Released from Living Cells,» *International Journal of Molecular Sciences*, 2022.
- [50] M. Alsaiari, A. R. Younus, A. Rahim, R. Alsaiari and N. Muhammad, «An electrochemical sensing platform of cobalt oxide@SiO2/C mesoporous composite for the selective determination of hydrazine in environmental samples,» *Microchemical Journal*, 2021.
- [51] R. K. Devi, G. Muthusankar, S.-M. Chen and G. Gopalakrishnan, «In situ formation of Co3O4 nanoparticles embedded N-doped porous carbon nanocomposite: a robust material for electrocatalytic detection of anticancer drug flutamide and supercapacitor application,» *Microchimica Acta*, 2021.
- [52] H. S. Magar, R. Y. A. Hassan and M. N. Abbas, «Non-enzymatic disposable electrochemical sensors based on CuO/Co3O4@MWCNTs nanocomposite modified screen-printed electrode for the direct determination of urea,» *Scientific Reports*, 2023.

- [53] S. Bilge, L. Karadurmus, E. B. Atici, A. Sınağ and S. A. Ozkan, «A novel electrochemical sensor based on magnetic Co3O4 nanoparticles/carbon recycled from waste sponges for sensitive determination of anticancer drug ruxolitinib,» *Sensors and Actuators B: Chemical*, 2022.
- [54] J. C. Dutta and P. K. Sharma, «Fabrication, Characterization and Electrochemical Modeling of CNT Based Enzyme Field Effect Acetylcholine Biosensor,» *IEEE Xplore*, 2018.
- [55] M. Arivazhagan and G. Maduraiveeran, «Hierarchical gold dispersed nickel oxide nanodendrites microarrays as a potential platform for the sensitive electrochemical detection of glucose and lactate in human serum and urine,» *Materials Chemistry and Physics*, 2022.
- [56] T. A. Saleh and G. Fadillah, «Recent trends in the design of chemical sensors based on graphene—metal oxide nanocomposites for the analysis of toxic species and biomolecules,» *TrAC Trends in Analytical Chemistry*, 2019.
- [57] Z. Khorablou, F. Shahdost-Fard and H. Razmi, «High sensitive detection of methamphetamine by high-performance aptasensing platform based on nickel oxide nanoparticles anchored on mxene,» *Microchemical Journal*, 2023.
- [58] K. Z. Mousaabadi, A. A. Ensafi and B. Rezaei, «Electrochemical Sensor for the Determination of Methotrexate Based on MOF-Derived NiO/Ni@C-Poly(isonicotinic acid),» *Industrial & Engineering Chemistry Research*, 2022.
- [59] R. Ahmad, M. Khan, P. Mishra, N. Jahan, M. A. Ahsan, I. Ahmad, M. R. Khan, Y. Watanabe, M. A. Syed and H. Furukawa, «Engineered Hierarchical CuO Nanoleaves Based Electrochemical Nonenzymatic Biosensor for Glucose Detection,» *Journal of The Electrochemical Society*, 2021.
- [60] S. Khan, Akrema, S. Qazi, R. Ahmad, K. Raza and Rahisuddin, «In Silico and Electrochemical Studies for a ZnO–CuO-Based Immunosensor for Sensitive and Selective Detection of E. coli,» ACS Omega, 2021.
- [61] B. Feyzi-barnaji, B. Darbasizadeh, E. Arkan, H. Salehzadeh, A. Salimi, F. Nili, R. Dinarvand and A. Mohammadi, «Immunoreaction-triggered diagnostic device using reduced graphene oxide/CuO NPs/chitosan ternary nanocomposite, toward enhanced electrochemical detection of albumin,» Journal of Electroanalytical Chemistry, 2020.
- [62] P. Narasimhappa and P. C. Ramamurthy, «Bio-mimicking the melanogenesis pathway using tyrosinase for dopamine sensing,» *Electrochimica Acta*, 2023.

- [63] J. S. Olarve, G. N. Santos and S. S. Kim, «Electrochemical detection of aflatoxins using a ZnO nanowire-modified biosensor with a droplet-based approach,» *Talanta Open*, 205.
- [64] Y. Sun, S. Li, Y. Yang, X. Feng, W. Wang, Y. Liu, M. Zhao and Z. Zhang, «Fabrication of a thermal responsive hemoglobin (Hb) biosensor via Hb-catalyzed eATRP on the surface of ZnO nanoflowers,» *Journal of Electroanalytical Chemistry*, 2019.
- [65] N. K. Yetim, «Hydrothermal synthesis of Co3O4 with different morphology: Investigation of magnetic and electrochemical properties,» *Journal of Molecular Structure*, 2021.
- [66] G. N. Narayanan and A. Karthigeyan, «Influence of different concentrations of Cetyltrimethylammonium bromide on morphological, structural and optical properties of Zinc Oxide nanorods,» *Materials Today: Proceedings*, 2016.
- [67] S. Abdolalian and M. Taghavijeloudar, «Performance evaluation and optimization of ZnO-PVP nanoparticles for photocatalytic wastewater treatment: Interactions between UV light intensity and nanoparticles dosage,» *Journal of Cleaner Production*, 2022.
- [68] R.-T. Wang, L.-B. Kong, J.-W. Lang, X.-W. Wang, S.-Q. Fan, Y.-C. Luo and L. Kang, «Mesoporous Co3O4 materials obtained from cobalt–citrate complex and their high capacitance behavior,» *Journal of Power Sources*, 2012.
- [69] T. G. Beatto, W. E. Gomes, A. Etchegaray, R. Gupta and R. K. Mendes, «Dopamine levels determined in synthetic urine using an electrochemical tyrosinase biosensor based on ZnO@Au core—shell,» *RCS Advances*, 2023.
- [70] J. Zhang, W. Gao, M. Dou, F. Wang, J. Liu, Z. Lia and J. Ji, «Nanorod-constructed porous Co3O4 nanowires: highly sensitive sensors for the detection of hydrazine,» *Analyst*, 2015.
- [71] A. Toldrà, A. Ainla, S. Khaliliazar, R. Landin, G. Chondrogiannis, M. Hanze, P. Réu and M. M. Hamedi, «Portable electroanalytical nucleic acid amplification tests using printed circuit boards and open-source electronics,» *Analyst*, 2022.
- [72] H. Shamkhalichenar, C. J. Bueche and J.-W. Choi, «Printed Circuit Board (PCB) Technology for Electrochemical Sensors and Sensing Platforms,» *Biosensors*, 2020.
- [73] J. Rainbow, E. Sedlackova, S. Jiang, G. Maxted, D. Moschou, L. Richtera and P. Estrela, «Integrated Electrochemical Biosensors for Detection of Waterborne Pathogens in Low-Resource Settings,» biosensors, 2020.

- [74] A. Ainla, M. P. S. Mousavi, M.-N. Tsaloglou, J. Redston, J. G. Bell, M. T. Fernández-Abedul and G. M. Whitesides, «Open-Source Potentiostat for Wireless Electrochemical Detection with Smartphones,» Analytical Chemistry.
- [75] G. Paimard, E. Ghasali and M. Baeza, «Screen-Printed Electrodes: Fabrication, Modification, and Biosensing Applications,» *Chemosensors*, 2023.
- [76] N.-B. Mincu, V. Lazar, D. Stan, C. Mihailescu, R. Iosub and A. Mateescu, «Screen-Printed Electrodes (SPE) for in vitro diagnostic purpose,» *Diagnostics*, 2020.
- [77] R. Couto, J. Lima and M. Quinaz, «Recent developments, characteristics and potential applications of screen-printed electrodes in pharmaceutical and biological analysis,» *Talanta*, 2016.
- [78] M. Li, Y.-T. Li, D.-W. Li and Y.-T. Long, «Recent developments and applications of screen-printed electrodes in environmental assays—A review,» *Analytica Chimica Acta*, 2012.
- [79] D. Antuña-Jiménez, M. González-García, D. Hernández-Santos and P. Fanjul-Bolado, «Screen-printed electrodes modified with metal nanoparticles for small molecule sensing,» *Biosensors*, 2020.
- [80] R. Torre, E. Costa-Rama, H. Nouws and C. Delerue-Matos, «Screen-printed electrode-based sensors for food spoilage control: Bacteria and biogenic amines detection,» *Biosensors*, 2020.
- [81] C. Foster, R. Kadara and C. Banks, Fundamentals of screen-printing electrochemical architectures, Springer Nature, 2015.
- [82] M. Khairy, R. Kadara and C. Banks, «Electroanalytical sensing of nitrite at shallow recessed screen printed microelectrode arrays,» *Analytical methods*, 2010.
- [83] L. Cao, C. Fang, R. Zeng, X. Zhao, F. Zhao, Y. Jiang and Z. Chen, «A disposable paper-based microfluidic immunosensor based on reduced graphene oxide-tetraethylene pentamine/Au nanocomposite decorated carbon screen-printed electrodes.,» *Sensors and Actuators B: Chemical*, 2017.
- [84] P. Sundaresan, T.-W. Chen, S.-M. Chen, T.-W. Tseng and X. Liu, «Electrochemical activation of screen printed carbon electrode for the determination of antibiotic drug metronidazole.,» *International Journal of Electrochemical Science*, 2018.
- [85] D. Pan, S. Rong, G. Zhang, Y. Zhang, Q. Zhou, F. Liu, M. Li, D. Chang and H. Pan, «Amperometric Determination of Dopamine Using Activated Screen-Printed Carbon Electrodes,» *Electrochemistry*, 2015.

- [86] A. Sanati, M. Jalali, K. Raeissi, F. Karimzadeh, M. Kharaziha, S. Mahshid and S. Mahshid, «A review on recent advancements in electrochemical biosensing using carbonaceous nanomaterials.,» *Microchimica Acta*, 2019.
- [87] G. Paimard, M. Shamsipur and M. Gholivand, «A three-dimensional hybrid of CdS quantum dots/chitosan/reduced graphene oxide-based sensor for the amperometric detection of ceftazidime.,» *Chemical Papers*, 2022.
- [88] Z. Fan, J. Ho, T. Takahashi, R. Yerushalmi, K. Takei, A. Ford, Y. Chueh and A. Javey, «Toward the development of printable nanowire electronics and sensors.,» *Advanced materials*, 2009.
- [89] W. Liu, Z. Zhang, X. Geng, R. Tan, S. Xu and L. Sun, «Electrochemical sensors for plant signaling molecules,» *Biosensors and Bioelectronics*, 2024.
- [90] A. S. Lima, K. R. Prieto, C. S. Santos, H. P. Valerio, E. Y. Garcia-Ochoa, A. Huerta-Robles, M. J. Beltran-Garcia, P. D. Mascio and M. Bertotti, «In-vivo electrochemical monitoring of H2O2 production induced by root-inoculated endophytic bacteria in Agave tequilana leaves,» *Biosensors and Bioelectronics*, 2018.
- [91] L. Sun, Y. Pan, J. Wu, D. Zhao, M. Hui, S. Zhu, X. Zhu, D. Li, F. Song and C. Zhang, «Paper-Based Analytical Devices for the Rapid and Direct Electrochemical Detection of Hydrogen Peroxide in Tomato Leaves Inoculated with Botrytis cinerea,» *Sensors*, 2020.
- [92] J. Zhang, M. Lu, H. Zhou, X. Du and D. Du, «Assessment of Salt Stress to Arabidopsis Based on the Detection of Hydrogen Peroxide Released by Leaves Using an Electrochemical Sensor,» *Internation Journal of molecular Sciences*, 2022.
- [93] H.-T. Zhu, Y.-Y. Ma, J. Du, H.-Q. Tan, Y.-H. Wang and Y.-G. Li, «Efficient Electrochemical Detection of Hydrogen Peroxide Based on Silver-Centered Preyssler-Type Polyoxometalate Hybrids,» *Inorganic Chemistry*.
- [94] D. Huo, D. Li, S. Xu, Y. Tang, X. Xie, D. Li, F. Song, Y. Zhang, A. Li and L. S. 1, «Disposable Stainless-Steel Wire-Based Electrochemical Microsensor for In Vivo Continuous Monitoring of Hydrogen Peroxide in Vein of Tomato Leaf,» *Biosensors*.
- [95] M. Parrilla, A. Sena-Torralba, A. Steijlen, S. Morais, Á. Maquieira and K. D. Wael, «A 3D-printed hollow microneedle-based electrochemical sensing device for in situ plant health monitoring,» *Biosensors and Bioelectronics*, 2024.

- [96] S. Cao, R. Yuan, Y. Chai, L. Zhang, X. Li and F. Gao, «A mediator-free amperometric hydrogen peroxide biosensor based on HRP immobilized on a nano-Au/poly 2,6-pyridinediamine-coated electrode,» *Bioprocess and Biosystems Engineering*, 2007.
- [97] X. Wang, F. Sun, Y. Huang, Y. Duana and Z. Yin, «A patterned ZnO nanorod array/gas sensor fabricated by mechanoelectrospinning-assisted selective growth,» *Chemical Communications*, 2015.
- [98] M. T. Z. Myint, N. S. Kumar, G. L. Hornyak and J. Dutta, «Hydrophobic/hydrophilic switching on zinc oxide micro-textured surface,» *Applied Surface Science*, 2013.
- [99] E. Sledevskis, M. Krasovska, V. Gerbreders, I. Mihailova, J. Keviss, V. Mizers and A. Bulanovs, «Impact of ZnO Nanostructure Morphology on Electrochemical Sensing Performance for Lead Ion Detection in Real Water Samples,» *Chemosensors*, 2025.
- [100] V. Mizers, V. Gerbreders, M. Krasovska, I. Mihailova, A. Bulanovs and E. Sledevskis, «Cheap and mass-producible electrochemical sensor of hydrogen peroxide,» *Latvian Journal Of Physics And Technical Sciences*, 2023.
- [101] J. Sheals, P. Persson and B. Hedman, «IR and EXAFS Spectroscopic Studies of Glyphosate Protonation and Copper(II) Complexes of Glyphosate in Aqueous Solution,» *Inorganic Chemistry*, 2001.

Appendix 1. Python program for electrochemical cell simulations

This appendix outlines the computational model used to simulate electrochemical reactions at a single electrode, generating the data for the plots in Chapters 2.1 and 2.2. The simulation employs a finite-difference approach to resolve transient mass transport and electrochemical kinetics within the diffusion layer adjacent to the electrode.

1. Model Assumptions and Discretization

- The diffusion layer is divided into discrete spatial grid points, and the simulation proceeds in discrete time steps. Key assumptions include:
- The far boundary of the diffusion layer is held at a constant reagent concentration, Cbulk, representing the bulk solution.
- The near boundary represents the electrode surface, where electrochemical reactions occur.

2. Electrochemical Kinetics at the Electrode Surface

At each time step, the following sequence of calculations is performed in accordance of mathematical model described in chapter 2.1:

- Potential Calculation: The electrode potential E is determined using the Nernst.
- Current Density Calculation: The Butler-Volmer equation is applied to compute the current density j.
- Faradaic Conversion Rate: The rate of ion conversion between oxidized and reduced forms is computed using Faraday's law of electrolysis.

3. Mass Transport via Diffusion

The updated concentrations at the electrode surface are propagated through the diffusion layer using Fick's second law. A finite-difference scheme ensures numerical stability.

4. Iterative Simulation and Data Collection

The above steps are repeated over multiple time steps. At each step, the following quantities are recorded for subsequent analysis:

- Instantaneous current density (j)
- Applied potential (E)
- Concentrations of oxidized (Cox) and reduced (Cred) species

The collected data is subsequently processed to generate the figures in the thesis.

The simulation code is implemented in two Python files:

CellSimulator.py Contains the core computational logic, including:

- Discretization of the diffusion layer
- Electrochemical kinetics calculations
- Mass transport simulation
- Data collection and storage

main.py Sets up the reaction conditions, including:

- Standard reaction potential
- Equilibrium current density
- Diffusion coefficient
- Bulk concentrations of reduced and oxidized species
- Time step and total simulation duration
- Applied electrode potential as a function of time

This file then initiates the simulation and plots the results.

Software Requirements:

- Python 3.10 or later
- NumPy (for numerical operations)
- SciPy (for scientific computing utilities)
- Pandas (for data handling and analysis)

File CellSimulator.py

```
import math
import numpy as np
from scipy.integrate import solve ivp
import pandas as pd
#This class calculates the diffusion of a single reactant over a diffusion layer
class DiffusionCalculator:
   def __init__(self, N_Points):
       #Setup default coefficients
       self.R = 8.31 # Universal gas constant
        self.F = 96485 # Faradays constant
       # number of points in diffusion layer space
       self.N Points = N Points
       #Concentrations of bulk solution
       self.Bulk = 1.0
       #Diffusion coefficients of reactant
       self.Coef = .5
       #Depth of diffusion layer
       self.Diff_layer = 0
       self.dx = 0
       self.CaclDiffLayerDepth(0.1)
   #This function calculates the depth of diffusion layer for given conditions
   def CaclDiffLayerDepth(self, dV_dt):
        #self.Diff_layer = math.sqrt( 2 * self.Coef / dV_dt ) / 100
        self.Diff layer = math.sqrt( 2 * self.Coef / dV dt )
        self.dx = self.Diff_layer / self.N_Points
   #This function takes the array of concentration data over space and calculates the
   #derivative of the concentration over time using Ficks second law
   #Conc should be np.array with lenght N_Points
   def CalcFickDiffusion(self, Conc, Approximate = False):
        Conc[-1] = self.Bulk # Bulk boundary condition
       dConc dt = np.zeros_like(Conc)
       for i in range(1, self.N_Points-1):
            dConc_dt[i] = self.Coef * ( (Conc[i+1] - 2 * Conc[i] + Conc[i-1] ) / self.dx**2 )
       #Approximate the temporal derivative at electrode surface based on Neumann condition
       if Approximate:
           dConc_dt[0] = self.Coef * ( Conc[1] - Conc[0] ) / self.dx
       return dConc_dt
   #This function generates an array of X values for calculated points
   def GetXValues(self):
       return np.linspace(0, self.Diff_layer, self.N_Points)
   #Generate an array of initial values
   def GetInitial(self):
        return np.full(self.N_Points, self.Bulk)
def map_value(x, a, b, c, d):
   # Linear transformation
   y = c + (x - a) * (d - c) / (b - a)
   # Clamping y to the target range
   return max(min(y, max(c, d)), min(c, d))
class ElectricSolver:
   def __init__(self):
       self.R = 8.31 # Universal gas constant
```

```
self.F = 96485 # Faradays constant
       self.T = 273+25 # System temperature
       self.n = 1 # Number of electrons participiating in reaction
       self.E0 = 0 # Standart potential of reaction
       self.j0 = 10000 # Current density at equilibrium
       #the rate of reaction for anodic and cathodic conversions
       self.alpha a = 0.5
       self.min conc = 1e-8
   #This function takes the concentrations of reduced and oxidised form of a rectant and
   #calculates Nernst equilibrium potential
   def Nernst_Potential(self, Red, Ox):
       Red = max (Red, self.min conc)
       Ox = max (Ox, self.min conc)
       return self.E0-self.R*self.T/(self.n*self.F)*math.log(Ox/Red)
   #This function takes the overpotential ni, concentrations of reduced and oxidised form and
   #calculates conversion current according to Butler-Volmer
   def ButlerVolmer_Current(self, E, Red, Ox):
       ni = E - self.Nernst Potential(Red, Ox)
       k = ni*self.n*self.F/(self.R*self.T)
       alpha_a = self.alpha_a
       alpha_c = 1 - self.alpha_a
       #return self.j0 * (math.exp(alpha_a*k) - math.exp(-alpha_c*k))
       return self.j0 * (Ox * math.exp(alpha a*k) - Red * math.exp(-alpha c*k))
   #This function accounts for numeric errors and discrepancies during calculations
   def Current(self, E, Red, Ox):
       j = self.ButlerVolmer Current(E, Red, Ox)
       return j
#This class performs simulation for a simple cell with 1 reaction happening inside
class CellSimulator:
   def __init__(self, Diff_N_Points):
       self.RedDiff = DiffusionCalculator(Diff_N_Points)
       self.OxDiff = DiffusionCalculator(Diff_N_Points)
       self.Reaction = ElectricSolver()
       self.dV_dt = 0.1
       self.SetExpectedSlope(0.1)
       self.time = np.zeros(1)
       self.RedConc = np.zeros((1, Diff_N_Points))
       self.0xConc = np.zeros((1, Diff_N_Points))
       self.voltage = np.zeros(1)
       self.current = np.zeros(1)
   def SetDiffCoefficients(self, RedDiff, OxDiff):
       self.RedDiff.Coef = RedDiff
       self.OxDiff.Coef = OxDiff
        self.RedDiff.CaclDiffLayerDepth(self.dV dt)
       self.OxDiff.CaclDiffLayerDepth(self.dV dt)
   def SetBulkConcentrations(self, RedBulk, OxBulk):
       self.RedDiff.Bulk = RedBulk
       self.OxDiff.Bulk = OxBulk
   def SetExpectedSlope(self, dV dt):
       self.dV dt = dV dt
       self.RedDiff.CaclDiffLayerDepth(self.dV dt)
       self.OxDiff.CaclDiffLayerDepth(self.dV_dt)
   #This function takes initial concentration distribution for a given cell and calculates
   #the cell dynamics
   def Solve(self, time_span, time_points, max_dt, Potential, Method="LSODA"):
```

```
t eval = np.linspace(0, time span, time points) # Points at which to store the
solution
        y0 = np.concatenate((self.RedDiff.GetInitial(), self.OxDiff.GetInitial()))
        #self.log = open("log.csv", 'w')
        #self.log.write("Time, Voltage, Current, Red, Ox, deltaRed, deltaOx, \n")
        #sol = solve_ivp(self.SolveStep, (0, time_span), y0, args=(Potential,), t_eval=t_eval,
max_step=max_dt, method="BDF")
        sol = solve_ivp(self.SolveStep, (0, time_span), y0, args=(Potential,), t_eval=t_eval,
max_step=max_dt, method=Method)
       #self.log.close()
        self.time = sol.t
        self.RedConc = sol.y[:self.RedDiff.N Points, :]
        self.OxConc = sol.y[self.RedDiff.N_Points:, :]
        self.voltage = np.zeros_like(self.time)
        self.current = np.zeros like(self.time)
        for t in range(np.size(self.time)):
            self.voltage[t] = Potential(self.time[t])
            self.current[t] = self.Reaction.Current(self.voltage[t], self.RedConc[0, t],
self.0xConc[0, t])
    def SolveStep(self, t, y, Potential):
        E = Potential(t)
        # unwrap variables
        Red = y[:self.RedDiff.N Points]
        Ox = y[self.RedDiff.N_Points:]
        dRed dt = np.zeros like(Red)
        d0x dt = np.zeros like(0x)
        #calculate diffusion, apply Neumann condition to electrode surface
        dRed_dt = self.RedDiff.CalcFickDiffusion(Red, True)
        d0x_dt = self.0xDiff.CalcFickDiffusion(0x, True)
        #calculate current density
        j = self.Reaction.Current(E, Red[0], Ox[0])
        #calculate Faradaic conversion rate
        dRed_dt[0] += j/(self.Reaction.n*self.Reaction.F)
        d0x_dt[0] -= j/(self.Reaction.n*self.Reaction.F)
        \#data = ",".join(str(x) for x in (t, E, j, Red[0], 0x[0], dRed_dt[0], d0x_dt[0],"\n"))
        #self.log.write(data)
        #print(t)
        dy dt = np.concatenate((dRed dt, dOx dt))
        return dy_dt
    def Save(self, file):
        combined array = np.column stack((self.time, self.voltage, self.current,
self.RedConc[0], self.OxConc[0]))
        df = pd.DataFrame(combined array, columns=['Time', 'Voltage', "Current", "Reduced",
"Oxidised"1)
        df.to csv(file, index=False)
```

File main.py

```
import numpy as np
from scipy.integrate import solve ivp
import matplotlib.pyplot as plt
import math
from CellSimulator import CellSimulator
#The set of functions that defines applied potentials over time for various analysis methods
def StepPotential(t):
    return np.where(t <= 0.1,
                    0.0,
                    1.0)
def CyclicVoltammetry(t):
    Vmax = 1
    Vmin = -1
    dVdt = 0.1
    Vstart = Vmin
    if t < 10:
        return Vstart
    else:
        t -= 10
    # Calculate the total potential change and the time to reach vertex potential
    Delta E = abs(Vmax - Vmin)
    T vertex = Delta E / dVdt
    T_total = 2 * T_vertex # Time for a complete forward and reverse sweep
    #calulate offset to account for starting voltage
    t offset = (Vstart - Vmin) / dVdt
    # Use modulo operation to determine the effective time within a single sweep cycle
    t_mod = np.mod(t + t_offset, T_total)
    # Determine the potential at each time point
    E t = np.where(t mod <= T vertex,</pre>
                   Vmin + dVdt * t_mod,
                   Vmax - dVdt * (t_mod - T_vertex))
    return E t
Vstart = -1
pulse_amp = 0.05 # Volts
pulse_period = 0.1 # seconds
step = 0.005 # Volts
def DifferentialPulseVoltammetry(t):
    if t < pulse_period:</pre>
        return Vstart # insert a blank periot at the start
    pulse_count = t // pulse_period
    t_cycle = t % pulse_period
    E_t = Vstart + step * pulse_count
    if t_cycle < pulse_period / 2:</pre>
        E_t += pulse_amp
    return E_t
#Define the simulation parameters
Simulator = CellSimulator(40)
Simulator.SetBulkConcentrations(0.0, 1.0)
Simulator.Reaction.E0 = 0.0
Simulator.Reaction.j0 = 1e3
Simulator.SetDiffCoefficients(0.5, 0.5)
#Run the simulation. The program can process only one simulation at a time; This file will
simulate DPV
#Simulation commands for other types of reactions are analysis out
#Simulator.Solve(50, 1000, 0.1, CyclicVoltammetry)
#Simulator.Solve(0.5, 1000, 0.1, StepPotential)
Simulator.Solve(40, 4000, 0.001, DifferentialPulseVoltammetry)
```

```
# Extract DPV curves
simulation dt = 40.0 / 4000.0
simulation_pulse_points = int(pulse_period / simulation_dt)
base_current = Simulator.current[int(simulation_pulse_points - 1)::simulation_pulse_points]
peak_current = Simulator.current[int(simulation_pulse_points / 2 -
1)::simulation_pulse_points]
peak_voltage = Simulator.voltage[int(simulation_pulse_points / 2 -
1)::simulation_pulse_points]
#Construct the plots
fig, (ax1, ax3) = plt.subplots(1, 2) # 1 rows, 2 column
ax2 = ax1.twinx()
ax1.plot (Simulator.time, Simulator.RedConc[0], label="Red(t)")
ax1.plot (Simulator.time, Simulator.OxConc[0], label="Ox(t)")
ax1.set_ylabel('Concentration')
ax2.plot(Simulator.time[1:], Simulator.current[1:], label='Current(t)', color="green")
ax2.set_ylabel("Current")
#"""
ax3.plot(peak_voltage, peak_current)
ax3.plot(peak_voltage, base_current)
ax3.plot(peak_voltage, peak_current - base_current)
ax3.set_xlabel("Voltage")
ax3.set_ylabel("Current")
plt.show()
# Save the data from ax3 to a CSV file
voltage_data = Simulator.voltage
current_data = Simulator.current
# Stack the two arrays together and save as a CSV
np.savetxt('DifferentialPulseVoltammetry_data.csv', np.column_stack((peak_voltage,
peak_current, base_current, peak_current - base_current)),
           delimiter=',',
           header='Voltage, Peak, Base, DPV',
           comments='')
```